

INFLUENCE OF BURIED PIPES ON DEFORMATIONS NEAR SHALLOW  
FOUNDATIONS

by

Candaş Öner

B.S., Civil Engineering, Boğaziçi University, 2018

Submitted to the Institute for Graduate Studies in  
Science and Engineering in partial fulfillment of  
the requirements for the degree of  
Master of Science

Graduate Program in Program Name

Boğaziçi University

2020

## ACKNOWLEDGEMENTS

First of all, I would like to express my sincere gratitude to my thesis supervisor Assoc. Prof. Özer Çiniciođlu. Even from my undergraduate study, he supported me, enhanced my knowledge immensely, and guided me.

I would like to also thank my co-advisor Assist. Prof. Selçuk Bildik for his kind support throughout my study. He has solved many problems that I encountered with.

I place on record, my sincere gratitude to member of thesis committee, Prof. İlknur Bozbey and Assist. Prof. İrem Zeynep Yıldırım, for their valuable contributions.

I would like to thank Prof. Dr. A. Burhan Ferhanođlu, Prof. Dr. Erdal Kurtođlu, Dr. Burak Deveci, Dr. Muharrem Ünlü, and many other doctors and nurses for sharing their knowledge and support during my treatment process.

I am also thankful to my friends Doruk Demirci, Kadir Eryılmaz, H. Güvenç Sunkar, and Karim Faridaliniya for their support during my study.

Everything aside, I want to thank my family for their endless support and care not only during this study but my entire life. Their support, ideas, and love have been enlightening my path. I also want to thank my beloved girlfriend for her eternal support. Even we were apart for a long time, she found a way to cheer me up. I would not be able to overcome hard times without them.

I would like to express my appreciation to Turkish Scientific and Technical Researchers Institute(TUBITAK) for supporting me financially. This project was supported by TUBITAK, Project Number: 116R020.

I also would like to express my appreciation to TUBITAK for supporting me

individually with 2210-A scholarship program.

## ABSTRACT

### INFLUENCE OF BURIED PIPES ON DEFORMATIONS NEAR SHALLOW FOUNDATIONS

In the design of the buried-pipe systems, precise calculation of the pressures that will act on the pipe is crucial as the most essential needs of humankind are conveyed or provided by buried-pipe systems. Also, recognition of the damage or problem is hard in the buried-pipe systems; therefore, it may take considerable amount of time to repair the system. Besides, when the pipes are placed under a foundation, classical soil response is affected by the foundation-pipe interaction as the pipe-system creates a discontinuity in the soil. There are many parameters that affect the pressures acting on the pipe, such as location of the pipe, relative density of the backfill, and pipe rigidity. In this work, small-scale physical model tests were conducted to examine the effect of pipe location on the pressures acting on the pipe and failure surface. A sand backfill was used in the experiments. To find the pipe pressures, strain gages were used, while to evaluate the changes in the extent of the affected regions, photographs of the tests were analyzed using particle image velocimetry(PIV) method. A total of 10 tests were done with a systematic change in the burial depth and horizontal distance from the foundation. Acquired data from strain gages and from PIV analysis were analyzed and examined, and the results were discussed.

## ÖZET

### GÖMÜLÜ BORULARIN SIĞ TEMELLERİN YAKININDA OLUŞAN DEFORMASYONLAR ÜZERİNDEKİ ETKİSİ

Gömülü boru sistemlerinin tasarımında boru üzerine etki eden basınçların dikkatli bir şekilde hesaplanması önemlidir, çünkü günümüzde insanlığın ihtiyaç duyduğu en temel gereksinimler bu sistemler sayesinde taşınmakta veya sağlanmaktadır. Ayrıca, gömülü boru sistemlerindeki problemlerin fark edilmesi zordur, bu yüzden söz konusu problemlerin düzeltilmesi için uzun bir zaman dilimi gerekebilir. Bunun yanında, temel altına yerleştirilen gömülü boru sistemlerinde, zeminin davranışı temel-boru etkileşiminden dolayı etkilenmektedir. Bunun sebebi, gömülü boruların zeminde bir süreksizlik yaratmasından kaynaklanmaktadır. Gömülü borulara etki eden basınçlar, birçok parametre ile değişmekte olup, bunlardan başlıcaları; borunun konumu, zemin sıklığı ve borunun rijitliğidir. Bu çalışmada, boru konumunun borunun üzerine etki eden basınçlarla ve temel deplasmanının etki alanıyla ilişkisini araştırmak için küçük ölçekli 1g fiziksel model deneyleri yapılmış olup, deneylerde kum zemin kullanılmıştır. Boru üzerindeki basıncı hesaplamak için gerilme ölçerler kullanılmış olup, sistemdeki deplasmanları görüntülemek için deney sırasında çekilen fotoğraflar Parçacık Görüntülü Hız Ölçüm (PGHÖ) tekniği ile analiz edilmiştir. Boru gömülme derinliği ve temelden yatay uzaklık değiştirilerek, toplamda 10 deney yapılmıştır. Gerilme ölçerler ve PGHÖ analizinden gelen veriler analiz edilerek incelenmiş ve elde edilen sonuçlar açıklanmıştır.

## TABLE OF CONTENTS

ACKNOWLEDGEMENTS . . . . .	iii
ABSTRACT . . . . .	v
ÖZET . . . . .	vi
LIST OF FIGURES . . . . .	ix
LIST OF TABLES . . . . .	xvi
LIST OF SYMBOLS . . . . .	xix
LIST OF ACRONYMS/ABBREVIATIONS . . . . .	xxii
1. INTRODUCTION . . . . .	1
2. LITERATURE REVIEW . . . . .	2
2.1. Introduction . . . . .	2
2.2. Physical Model Tests . . . . .	4
2.2.1. Physical Model Tests Under Static Load . . . . .	5
2.2.1.1. Physical Model Tests Under Static Load with Rein- forcement . . . . .	5
2.2.1.2. Physical Model Tests Under Static Load Without Re- inforcement . . . . .	12
2.2.2. Physical Model Tests Under Dynamic Load . . . . .	14
2.3. Usage of PIV Method in Geotechnical Engineering . . . . .	19
2.4. Types of Failure Under Shallow Foundations and Failure Surfaces . . . . .	25
2.4.1. General Shear Failure . . . . .	25
2.4.2. Punching Shear Failure . . . . .	25
2.4.3. Local Shear Failure . . . . .	27
2.4.4. Failure Surfaces . . . . .	29
3. METHODOLOGY . . . . .	36
3.1. Experiment Setup . . . . .	36
3.1.1. Test Box . . . . .	36
3.1.2. Model Footing . . . . .	36
3.1.3. Linear Variable Differential Transformers(LVDTs) . . . . .	38

3.1.4.	Load Cell . . . . .	41
3.1.5.	Strain Gages . . . . .	41
3.1.6.	Data Acquisition System . . . . .	45
3.1.7.	LabVIEW Program . . . . .	46
3.2.	Sand Properties . . . . .	47
3.2.1.	Index Properties . . . . .	47
3.2.1.1.	Sieve Analysis . . . . .	47
3.2.1.2.	Specific Gravity Test . . . . .	48
3.2.1.3.	Minimum and Maximum Void Ratio Tests . . . . .	48
3.2.1.4.	Partice Characteristics of the Tested Sands . . . . .	48
3.2.2.	Strength Properties . . . . .	49
3.2.2.1.	Triaxial Tests . . . . .	49
3.3.	PIV Analysis . . . . .	55
3.4.	Pipe Properties . . . . .	58
3.5.	Procedure of the Experiments . . . . .	58
4.	RESULTS . . . . .	61
4.1.	Analyses of the Photos . . . . .	64
4.1.1.	Effect of Pipe Location on the Affected Area . . . . .	64
4.1.2.	Comparison of the Pipe Displacements . . . . .	78
4.2.	Analysis of the Pressure Acting on the Pipe . . . . .	83
4.2.1.	Effect of Burial Depth(H/D) on Pipe Pressure . . . . .	83
4.2.2.	Effect of Horizontal Distance(X/D) on Pipe Pressure . . . . .	88
4.2.3.	Effect of the Amount of the Settlement on Pipe Pressure . . . . .	91
5.	DISCUSSION . . . . .	97
6.	CONCLUSIONS . . . . .	99
	REFERENCES . . . . .	100
	APPENDIX A: PRESSURE VALUES ON THE DIFFERENT STRAIN GAGES IN EACH TEST . . . . .	105

## LIST OF FIGURES

Figure 2.1.	Pipe placement methods, (a) trench method, (b) positive projection method, (c) negative projection method (Saglamer and Balkaya, 2015). . . . .	3
Figure 2.2.	Imperfect trench method (Saglamer and Balkaya, 2015). . . . .	4
Figure 2.3.	Testing system used (Won <i>et al.</i> , 2004). . . . .	5
Figure 2.4.	Plate settlement vs Applied pressure (Corey <i>et al.</i> , 2014). . . . .	6
Figure 2.5.	Vertical deflection vs Applied pressure (Corey <i>et al.</i> , 2014). . . . .	7
Figure 2.6.	Effect of reinforcement on the pressure acting on the crown of the pipe (Hegde and Sitharam, 2015). . . . .	8
Figure 2.7.	Effect of burial depth on the pressure acting on the crown of the pipe (Hegde and Sitharam, 2015). . . . .	8
Figure 2.8.	Horizontal(left), inverted U(middle), and enveloped(right) orientation (Pires and Palmeria, 2017). . . . .	9
Figure 2.9.	Vertical stress vs Surcharge pressure on different orientation and geogrid types (Pires and Palmeria, 2017). . . . .	9
Figure 2.10.	Test box and geotextiles used in the experiments (Kou <i>et al.</i> , 2018). . . . .	10
Figure 2.11.	Pressure acting on the crown of the pipe vs Backfill height (Ma <i>et al.</i> , 2019). . . . .	11

Figure 2.12. Compatibleness of the methods for different relative density ranges (Terzi <i>et al.</i> , 2012). . . . .	12
Figure 2.13. Vertical and horizontal deflection of the pipe, and their ratio for different relative density ranges (Terzi <i>et al.</i> , 2012). . . . .	12
Figure 2.14. Illustration of the parameters (Bildik and Laman, 2015). . . . .	13
Figure 2.15. Results of the tests for different x and H values (Bildik and Laman, 2015). . . . .	14
Figure 2.16. Change in hoop stress with embedment ratio (Bildik and Laman, 2019). . . . .	15
Figure 2.17. Change in hoop stress with horizontal distance (Bildik and Laman, 2019). . . . .	15
Figure 2.18. Layout of the reinforcements and buried pipe (Moghaddas Tafreshi and Khalaj, 2008). . . . .	16
Figure 2.19. Testing system used in the experiments (Khalaj <i>et al.</i> , 2017). . . . .	17
Figure 2.20. Layout plan of the geocell reinforcement and buried pipe (Fattah <i>et al.</i> , 2018). . . . .	18
Figure 2.21. Changes in the analysis results with the patch sizes (Altunbas, 2015). . . . .	20
Figure 2.22. PIV analysis results (Mirzababaei <i>et al.</i> , 2017). . . . .	21
Figure 2.23. PIV analysis results for different relative density and particle size values (Ghalehjough <i>et al.</i> , 2018). . . . .	21

Figure 2.24. Test set-up, (1) high-resolution camera, (2) footing and load cell, (3) buried pipe (Zhang and Askarinejad, 2018). . . . .	22
Figure 2.25. PIV Analysis results as displacement vectors (Chen <i>et al.</i> , 2019). . .	23
Figure 2.26. Cranical and caudal directions (Martinez <i>et al.</i> , 2019). . . . .	24
Figure 2.27. PIV Analysis, (a) resultant displacement, (b) shear strains, (c) volumetric strains (Martinez <i>et al.</i> , 2019). . . . .	24
Figure 2.28. Displacement fields found by PIV analysis (Oner <i>et al.</i> , 2019). . .	25
Figure 2.29. General shear failure (Das, 2017). . . . .	26
Figure 2.30. Load-Settlement graph for the general shear failure (Das, 2017). . .	26
Figure 2.31. Punching shear failure (Das, 2017). . . . .	27
Figure 2.32. Load-Settlement graph for the punching shear failure (Das, 2017). . .	27
Figure 2.33. Local shear failure (Das, 2017). . . . .	28
Figure 2.34. Load-Settlement graph for the local shear failure (Das, 2017). . . . .	28
Figure 2.35. Failure Surface (Terzaghi, 1943). . . . .	29
Figure 2.36. Failure Surface (Meyerhof, 1951). . . . .	31
Figure 2.37. Failure Surface (Balla, 1962). . . . .	34
Figure 2.38. Determination of the type of failure (Vesic, 1973). . . . .	35

Figure 3.1.	Test box used in the experiments. . . . .	37
Figure 3.2.	Model footing used in the experiments. . . . .	38
Figure 3.3.	Spring system used in the experiments. . . . .	39
Figure 3.4.	Location of the spring-system in model footing. . . . .	39
Figure 3.5.	Hexagonal steel plate used in the experiments. . . . .	40
Figure 3.6.	LVDTs used in the experiments. . . . .	40
Figure 3.7.	Load cell used in the experiments. . . . .	42
Figure 3.8.	Calibration of the load cell. . . . .	42
Figure 3.9.	Strain gages used in the experiments. . . . .	43
Figure 3.10.	Special glue used in the experiments. . . . .	43
Figure 3.11.	Locations of the strain gages. . . . .	45
Figure 3.12.	Load cell cables attached to a NI-9949 module. . . . .	46
Figure 3.13.	NI cDAQ-9179 chassis with a NI-9237 module. . . . .	47
Figure 3.14.	Percent finer vs Sieve opening size. . . . .	48
Figure 3.15.	Peak friction angle vs Peak dilation angle. . . . .	51
Figure 3.16.	Calculated peak dilation angle vs Actual peak dilation angle. . . . .	54

Figure 3.17.	$q_{dev}$ vs $\epsilon_a$ for $I_D=20\%$ $\sigma'_3=50\text{kPa}$ test. . . . .	55
Figure 3.18.	Comparison of the vector fields in UR4 test (pipe area excluded(left), pipe area included(right)). . . . .	57
Figure 3.19.	Comparison of the displacement fields in UR4 test (pipe area excluded(left), pipe area included(right)). . . . .	57
Figure 3.20.	Model pipe used in the experiments. . . . .	58
Figure 3.21.	Test setup prior to the start of the test. . . . .	60
Figure 4.1.	Investigated parameters. . . . .	61
Figure 4.2.	Location of the pipe for each test. . . . .	62
Figure 4.3.	Illustration of the angles between connection lines and the horizontal. . . . .	63
Figure 4.4.	Photograph, displacement field, and vector field of the reference test. . . . .	65
Figure 4.5.	Photograph, displacement field, and vector field of the UR1 test. . . . .	66
Figure 4.6.	Photograph, displacement field, and vector field of the UR2 test. . . . .	67
Figure 4.7.	Photograph, displacement field, and vector field of the UR3 test. . . . .	68
Figure 4.8.	Photograph, displacement field, and vector field of the UR4 test. . . . .	69
Figure 4.9.	Photograph, displacement field, and vector field of the UR5 test. . . . .	70
Figure 4.10.	Photograph, displacement field, and vector field of the UR6 test. . . . .	71

Figure 4.11. Photograph, displacement field, and vector field of the UR7 test. . . . .	72
Figure 4.12. Photograph, displacement field, and vector field of the UR8 test. . . . .	73
Figure 4.13. Photograph, displacement field, and vector field of the UR9 test. . . . .	74
Figure 4.14. Determination of the affected zone. . . . .	75
Figure 4.15. Change in $\zeta$ for different pipe locations. . . . .	76
Figure 4.16. Change in the vertical extent of the affected zone different pipe locations. . . . .	77
Figure 4.17. Determining pipe displacement for UR1 test. . . . .	79
Figure 4.18. Normalized horizontal displacement for the tests. . . . .	80
Figure 4.19. Normalized vertical displacement for the tests. . . . .	81
Figure 4.20. Normalized displacement vectors for the tests. . . . .	82
Figure 4.21. Illustration of the normalized pipe pressures of UR1-UR4-UR7 tests.	84
Figure 4.22. Illustration of the normalized pipe pressures of UR2-UR5-UR8 tests.	86
Figure 4.23. Illustration of the normalized pipe pressures of UR3-UR6-UR9 tests.	87
Figure 4.24. Illustration of the normalized pipe pressures of UR1-UR2-UR3 tests.	89
Figure 4.25. Illustration of the normalized pipe pressures of UR4-UR5-UR6 tests.	89

Figure 4.26.	Illustration of the normalized pipe pressures of UR7-UR8-UR9 tests.	90
Figure 4.27.	Illustration of the effect of the foundation settlement on UR1 test.	92
Figure 4.28.	Illustration of the effect of the foundation settlement on UR4 test.	93
Figure 4.29.	Illustration of the effect of the foundation settlement on UR7 test.	94
Figure 4.30.	Illustration of the effect of the foundation settlement on UR8 test.	94
Figure 4.31.	Illustration of the effect of the foundation settlement on UR9 test.	95

## LIST OF TABLES

Table 2.1.	Comparison of $N_\gamma$ values. . . . .	33
Table 3.1.	Properties of the load cell. . . . .	41
Table 3.2.	Strain gage properties. . . . .	44
Table 3.3.	Index properties. . . . .	49
Table 3.4.	Triaxial test results. . . . .	51
Table 3.5.	Conversion to plain-strain condition. . . . .	53
Table 3.6.	Triaxial tests used to find $E_{50}$ . . . . .	55
Table 3.7.	Strength properties of the sand. . . . .	56
Table 3.8.	Pipe properties. . . . .	58
Table 4.1.	Testing program. . . . .	62
Table 4.2.	The angle of the connection line with the horizontal. . . . .	63
Table 4.3.	Comparison of the areal extent of the affected zones. . . . .	75
Table 4.4.	Comparison of the vertical extent of affected zones. . . . .	76
Table 4.5.	Most affected region of the pipe from displacement. . . . .	78

Table 4.6.	Normalized pipe displacement comparison for $X/D > 0$ . . . . .	79
Table 4.7.	Normalized pipe displacement comparison for $X/D = 0$ . . . . .	80
Table 4.8.	Change in $\lambda$ with the angle of connection line with horizontal. . . .	82
Table 4.9.	Angle between normalized displacement vectors with the horizontal.	83
Table 4.10.	Comparison of the normalized pipe pressures of UR1-UR4-UR7 tests.	84
Table 4.11.	Comparison of the normalized pipe pressures of UR2-UR5-UR8 tests.	85
Table 4.12.	Change in the pressure at the 3 <sup>rd</sup> strain gage with displacement. . .	86
Table 4.13.	Comparison of the normalized pipe pressures of UR3-UR6-UR9 tests.	87
Table 4.14.	Comparison of the normalized pipe pressures of UR1-UR2-UR3 tests.	88
Table 4.15.	Comparison of the normalized pipe pressures of UR4-UR5-UR6 tests.	88
Table 4.16.	Comparison of the normalized pipe pressures of UR7-UR8-UR9 tests.	90
Table 4.17.	$\Gamma_1$ and the angle of the connection line with the horizontal. . . . .	91
Table 4.18.	Effect of the foundation settlement on UR1-UR4 tests. . . . .	92
Table 4.19.	Effect of the foundation settlement on UR7-UR8-UR9 tests. . . . .	93
Table 4.20.	Effect of the foundation settlement on UR3-UR5-UR6 tests. . . . .	96
Table A.1.	Pressures in the UR1 test. . . . .	105

Table A.2.	Pressures in the UR2 test. . . . .	106
Table A.3.	Pressures in the UR3 test. . . . .	107
Table A.4.	Pressures in the UR4 test. . . . .	108
Table A.5.	Pressures in the UR5 test. . . . .	109
Table A.6.	Pressures in the UR6 test. . . . .	110
Table A.7.	Pressures in the UR7 test. . . . .	111
Table A.8.	Pressures in the UR8 test. . . . .	112
Table A.9.	Pressures in the UR9 test. . . . .	113

## LIST OF SYMBOLS

$a_\psi$	A stress-based constant (Cinicioglu and Abadkon, 2015)
$b$	Width of the pile (Chen <i>et al.</i> , 2019)
$B$	Width of the foundation
$B$	Pore pressure parameter
$B_c$	Diameter of the buried pipe (Kou <i>et al.</i> , 2018)
$c$	Cohesion
$C$	Thickness of the EPS Geofoam (Ma <i>et al.</i> , 2019)
$C_c$	Coefficient of curvature
$C_u$	Coefficient of uniformity
$d\epsilon_1$	Change in the major principal strain
$d\epsilon_v$	Change in the volumetric strain
$D$	Diameter of the pipe
$D_f$	Depth of the foundation
$D_{50}$	Median particle Size
$e_{max}$	Maximum void ratio
$e_{min}$	Minimum void ratio
$E$	Modulus of elasticity
$E_{50}$	Secant modulus
$G_s$	Specific gravity
$L$	Initial length
$H$	Burial depth of the pipe
$I_D$	Relative density
$k$	Reduction factor (Vesic, 1973)
$K_{p\gamma}$	Passive earth pressure coefficient
$K_{\Phi P}$	Ratio of the critical state friction angle to peak friction angle for plain-strain conditions (Nanda and Patra, 2015)
$K_{\Phi T}$	Ratio of the critical state friction angle to peak friction angle for axisymmetric conditions (Nanda and Patra, 2015)

$m_\psi$	A density-based constant (Cinicioglu and Abadkon, 2015)
$N_c, N_q, N_\gamma$	Bearing pressure coefficients (Terzaghi, 1943)
$p_a$	Atmospheric pressure
$p'_i$	Initial mean effective stress
$P_u$	Measured Pressure (Hegde and Sitharam, 2015)
q	Surcharge Pressure
$q_{dev}$	Deviatoric stress
$q_u$	Maximum Applied Pressure (Hegde and Sitharam, 2015)
r	Length of any line between the right corner of the elastic zone and radial shear zone
$r_0$	Length of the one edge that is not parallel to the horizontal of the triangular elastic zone (Terzaghi, 1943)
$r_{ps}$	Dilatancy effect parameter on friction for plain-strain conditions
$r_{tx}$	Dilatancy effect parameter on friction for axisymmetric conditions
$R$	Nominal gage resistance
$R_{ave}$	Average roundness
$S_{ave}$	Average sphericity
x	Horizontal distance from the right end of the foundation to the left end of the pipe (Bildik and Laman, 2015)
X	Horizontal distance from center of the footing to the center of the pipe
$\alpha$	Angle between the edge of the triangular zone and the horizontal (Hu, 1964)
$\beta_1$	Pressure acting on the 1 <sup>st</sup> strain gage to the pressure acting on the foundation at the same amount of settlement
$\beta_2$	Pressure acting on the 2 <sup>nd</sup> strain gage to the pressure acting on the foundation at the same amount of settlement
$\beta_3$	Pressure acting on the 3 <sup>rd</sup> strain gage to the pressure acting on the foundation at the same amount of settlement
$\beta_4$	Pressure acting on the 4 <sup>th</sup> strain gage to the pressure acting on the foundation at the same amount of settlement

$\gamma$	Unit weight
$\Gamma_1$	Ratio of the $\beta_1$ of the tests having $X/D > 0$ to $\beta_1$ of the test where $X/D = 0$ at the same burial depth
$\Delta L$	Change in the length
$\Delta R$	Change in the resistance
$\Delta u$	Change in pore water pressure
$\Delta \sigma_3$	Change in the cell pressure
$\epsilon$	Strain
$\epsilon_a$	Axial strain
$\zeta$	Ratio of the area of the affected zone to the total area of interest
$\theta$	Inclination between $r_0$ and $r$ (Terzaghi, 1943)
$\lambda$	Ratio of the normalized horizontal displacement of the pipe to normalized vertical displacement of the pipe
$\sigma$	Stress
$\sigma'_3$	Effective minor principal stress
$\phi$	Friction angle
$\phi'$	Modified friction angle (Vesic, 1973)
$\Phi'_p$	Peak friction angle
$\Phi_c^T$	Critical state friction angle for axisymmetric conditions (Nanda and Patra, 2015)
$\Phi_p^T$	Peak friction angle for plain-strain conditions (Nanda and Patra, 2015)
$\Phi_p^P$	Peak friction angle for axisymmetric conditions (Nanda and Patra, 2015)
$\Psi_p$	Peak dilation angle

## LIST OF ACRONYMS/ABBREVIATIONS

AOI	Area of Interest
ASTM	American Society for Testing and Materials
BCR	Bearing Capacity Ratio (Bildik and Laman, 2015)
EPS	Expanded Polystyrene
GF	Gage Factor
HDPE	High Density Polyethylene
LVDT	Linear Variable Differential Transformer
PGHÖ	Parçacık Görüntülü Hız Ölçüm
PIV	Particle Image Velocimetry
PVC	Polyvinyl Chloride

## 1. INTRODUCTION

The buried pipe systems are extensively used in today's world. Cracking, leaking, or any other potential failure in these systems might lead to disturbances and even to catastrophe; therefore, necessary considerations and calculations to protect the pipes should be precisely done before installment. There have been a lot of research conducted in this area, and main purpose has been focused on the mitigation of the excessive pressure on pipes using geosynthetic materials (Pires and Palmeria, 2017; Kou *et al.*, 2018).

Evaluation of the engineering response of a system can be done by interpreting stresses and strains. In the literature, majority of the research on this topic used stresses acting on the pipe to understand behavior, while less work has been done using visualization.

In the scope of this thesis, a joint approach was followed. Within the scope of TUBITAK Project No:116R020A, a series of physical model tests were done in a model rigid box, in which pipes were placed in the pre-determined locations. Loading was done by a model footing, and as a backfill material, sand was used. Effect of the location of the pipe on pipe pressure was obtained by data recorders, while its effect on displacements in the system was found by image analysis, using a method called Particle Image Velocimetry(PIV). With the simultaneous assessment of the results found by data recorders and PIV method, a more elaborate insight on the effect of buried pipes location was acquired.

## 2. LITERATURE REVIEW

### 2.1. Introduction

In today's world, the transportation of most essential needs, such as water, petroleum, gas, and communication systems, is accomplished by systems of buried pipes. As the pipes are installed beneath the soil, they are exposed to static loads. Besides, major portion of infrastructure is in cities where, human interactions on buried pipes are inevitable, mostly in terms of traffic loads. Therefore, while installing a buried pipe system, the combinations of load-patterns should be taken into account.

Buried pipes are divided into two categories based on flexibility: rigid pipes and flexible pipes. Pipes are defined as rigid if 0.1% change in their lateral or horizontal dimension leads to hazardous cracks. Rigid pipes are generally made of cement, concrete, or reinforced concrete. In design, rigid pipes are considered to undergo zero deformation; therefore, all the applied load is carried by the rigid pipes, not the soil. Flexible pipes instead are generally made of plastic, PVC, or thin steel. Flexible pipes can undergo deformation and are defined as the pipes that can undergo a change of 2% in their dimensions without structural hazard. Because of this flexibility, load is carried not only by the pipe but also by the surrounding soil.

There are two main methods for the placement of buried pipe systems: trench method and embankment method. In trench method, a narrow and deep trench is dug in soil, and the pipe is placed in this trench. Then, trenches are backfilled with appropriate materials. Sewer, drainage, water, and gas pipes are usually placed with this method. Embankment methods are divided into two groups, as positive projection and negative projection method. In positive projection method, the pipe is placed above the natural soil surface and then backfilled with an appropriate filling material up to a depth, while in negative projection method, the pipe is placed inside a narrow and shallow trench and backfilled up to a pre-considered depth. Both methods are

used in both road and railroad culverts. The illustrations of trench method, positive projection method, and negative projection method can be seen in Figure 2.1.

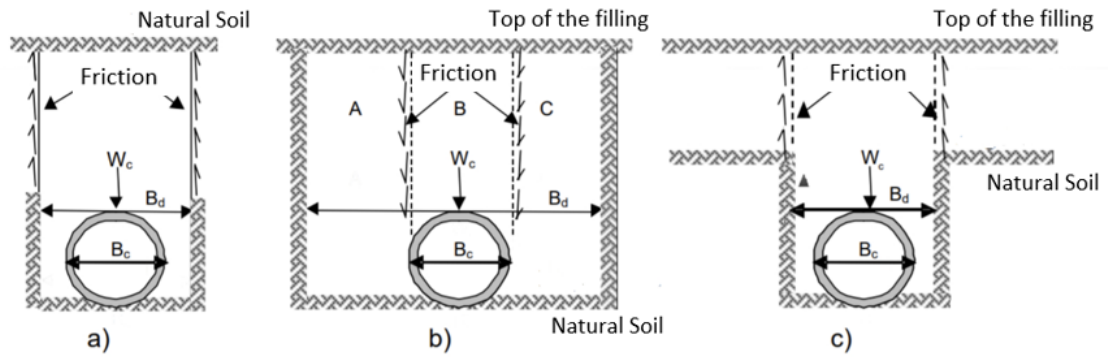


Figure 2.1. Pipe placement methods, (a) trench method, (b) positive projection method, (c) negative projection method (Saglamer and Balkaya, 2015).

There is also a special pipe placement method, called imperfect trench method. As in the negative projection method, the pipe is placed inside a narrow and shallow trench and then backfilled. The distance between the crown of the pipe and the top of the fill should be approximately 1-1.5 times the pipe diameter. In this process, filling should be well-compacted. Then, another trench is dug until reaching the top of the crown and then filled with loose material. Afterwards, the filling is continued to a predetermined depth. While the final filling is getting done, the loose part undergoes more settlement than the compacted zone, creating a positive arching that leads to a decrease in the load acting on the crown of the pipe. In order to make this process effective, the trench width should be equal to the pipe width, and the center of the trench and pipe should be vertically aligned. The illustration of imperfect trench method is in Figure 2.2.

Nowadays, with the improvement in the pipe technology, trenchless methods are being used in pipe placement. Some deformations may be observed in the application of deep trenches, especially during lowering ground water table, backfilling, supporting the trench, and removing the support. Trenchless methods are more advantageous when surface deformation is not desired. Some of the most popular trenchless methods

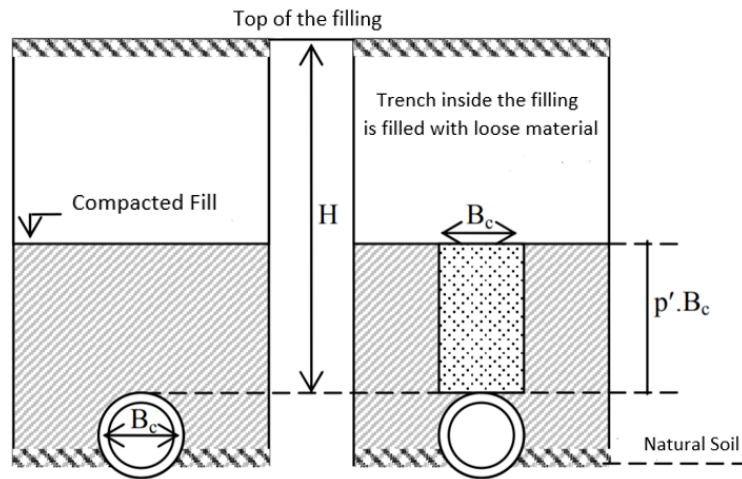


Figure 2.2. Imperfect trench method (Saglamer and Balkaya, 2015).

are pipe ramming, pipe jacking, horizontal directional drilling, and microtunneling (Saglamer and Balkaya, 2015).

## 2.2. Physical Model Tests

The behavior of buried pipe systems has been investigated extensively with analytical investigations (Masada, 2000), numerical investigations (Witthoeft and Kim, 2016; Meguid and Hussein, 2017), full-scale tests (Sargand *et al.*, 2005; Wang *et al.*, 2020), and also experimental investigations in laboratory. In experimental works, the research has been focused more on the primary factors that affect the pressure on the pipe and the bearing capacity of the system. These factors are the location of the pipe, relative density of the backfill, base course, loading conditions, and reinforcements. Geosynthetics have been primarily used as reinforcements, and the effects of geosynthetic type and their properties on the system performance have been studied. Some of the similar experimental work will be briefly explained in this section.

### 2.2.1. Physical Model Tests Under Static Load

2.2.1.1. Physical Model Tests Under Static Load with Reinforcement. In 2004, Won *et al.* performed several laboratory experiments to figure out the effects of reinforcement layer characteristics above a buried pipe on the deformations of the buried pipe. This was done by altering the number of reinforcement layers, reinforcement type, and burial depth of the pipe. In Figure 2.3, the test box used in the experiments is sketched. In total, three different reinforcement types, three different burial depths, and four different layers of reinforcement were tested. In the analysis of the reinforcement type, it was concluded that the shape of the reinforcement and mesh spacing were more important factors than the maximum tensile strength of the reinforcement. Also, it was seen that the bearing capacity of the system tended to increase proportionally with the number of reinforcement layers up to two layers. Afterwards, no such increase was observed. Besides, the effect of pipe burial depths was investigated, and it was stated that the bearing capacity decreased with a decrease in the burial depth.

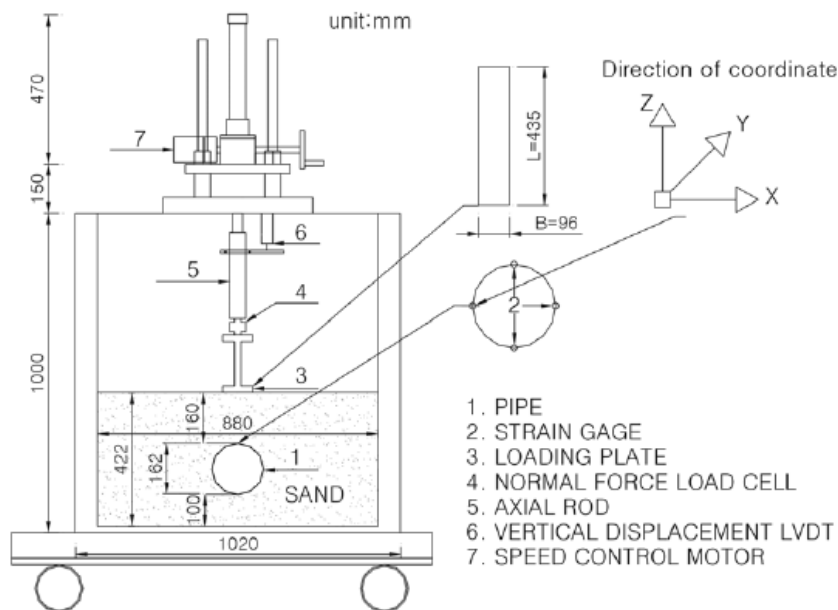


Figure 2.3. Testing system used (Won *et al.*, 2004).

Corey *et al.* (2014) discussed the physical model test results conducted on the shallow-buried steel-reinforced high-density polyethylene (HDPE) pipes exposed to

static loads transferred from a steel plate. In the tests, a three-meter wide box frame with a fat clay backfill was used. While placing the steel-reinforced HDPE pipes, a trench was created inside the fat clay layer and then filled with sand. In total, four tests were performed, where the tested parameters were the presence of reinforcement (geogrids) and the type of base course (aggregates and sand). The deflection of the pipe and the loading plate, earth pressures, geogrid strain, and pipe strain were recorded during the tests. As seen in Figure 2.4, when the base course was sand, the use of geogrids led to a decrease in the loading plate settlement from 4.5mm to approximately 3.5mm at the maximum pressure of 345kPa. However, this difference was not very significant when aggregates were used as base materials because, the loading plate settlement decreased from approximately 3.5mm to 3mm at the maximum pressure of 552kPa. Also, when the base course was selected as aggregates, the vertical settlement of pipe cross-section under the loading plate was decreased approximately by 0.35mm with the implementation of geogrids, while no significant difference was observed when the base course was selected as sand as seen in Figure 2.5.

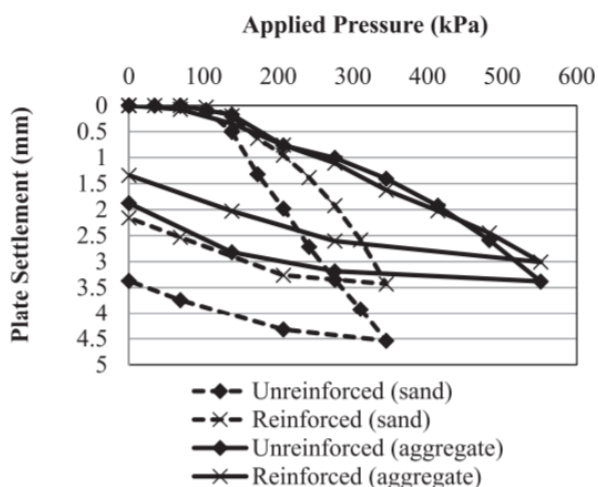


Figure 2.4. Plate settlement vs Applied pressure (Corey *et al.*, 2014).

Hegde and Sitharam (2015) presented their findings from physical model tests that were done to understand the effects of geocell reinforcement on buried pipe systems. In the tests, not only the sole effects of geocell were investigated, but also the

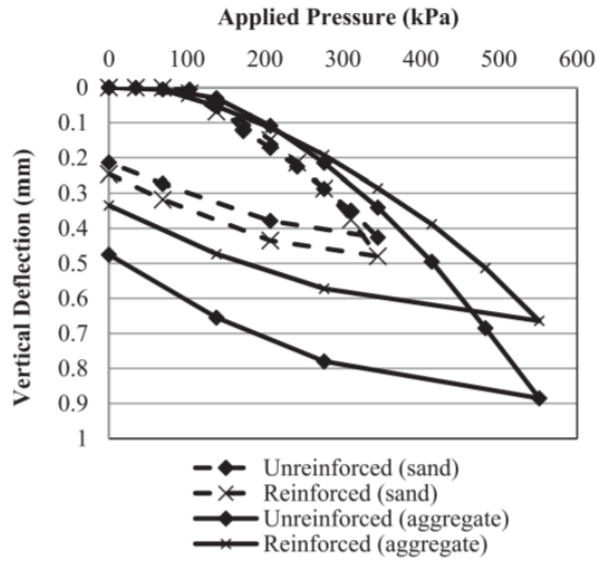


Figure 2.5. Vertical deflection vs Applied pressure (Corey *et al.*, 2014).

effects of geogrids and the combination of geocells with geogrids were investigated, and the tests were repeated for various burial depth conditions. The pressure and the strain on the crown of the pipe were measured using strain gages. It was stated that the best performance was reached when the combination of reinforcements was used, resulting in an approximately 50% decrease in the vertical pressure and the strain on the crown of the pipe. This is illustrated in Figure 2.6, where  $P_u$  is the measured pressure value, and  $q_u$  is the maximum applied pressure. The results also showed that the sole application of geocell yielded a higher decrease compared to the sole geogrid application. Besides, as seen in Figure 2.7, with an increase in the burial depth, the vertical pressure and the strain at the crown of the pipe decreased significantly.

Pires and Palmeria (2017) conducted laboratory experiments in a rigid metal tank filled with geogrid-reinforced sand to determine the effects of type and orientation of geosynthetics on the settlement-pressure mechanism of the loading plate and stress distribution along the pipe. To accomplish this, 10 tests were performed in total with three different orientation types, three different geosynthetic types, and a reference experiment with no reinforcement. The three orientation types were horizontal, inverted

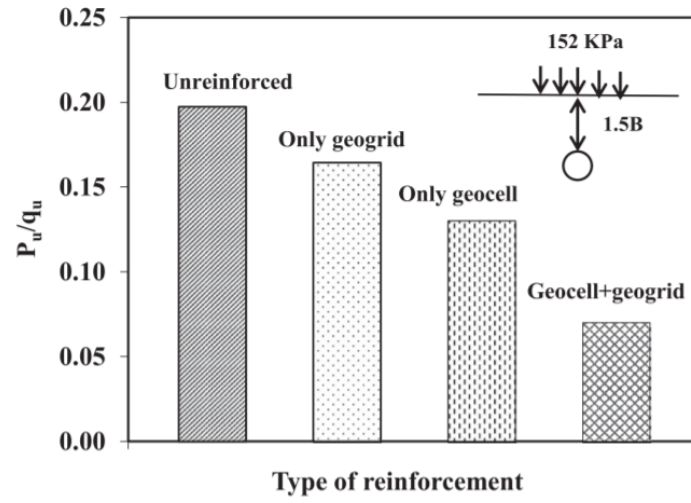


Figure 2.6. Effect of reinforcement on the pressure acting on the crown of the pipe (Hegde and Sitharam, 2015).

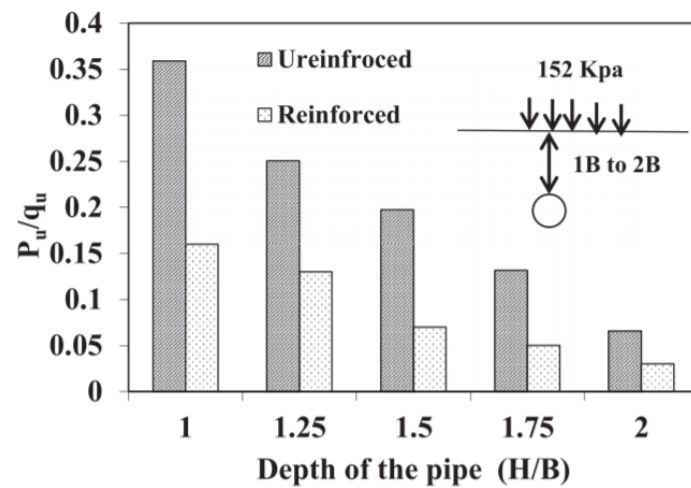


Figure 2.7. Effect of burial depth on the pressure acting on the crown of the pipe (Hegde and Sitharam, 2015).

U, and enveloped as seen in Figure 2.8, respectively. The three geogrid-reinforcements were named as R1, R2, and R3 with tensile strengths of 1.45kN/m, 12.0kN/m, and 20.3kN/m, respectively. In the results, it was observed that the load-settlement of the footing flattened with an increase in the stiffness of the geogrid. In other words, under the application of the same surcharge pressure, the footing system reinforced with a stiffer geogrid underwent a smaller settlement. The minimum settlement of the footing was observed when the orientation was enveloped. Similar observations were recorded for the vertical stress acting on the crown of the pipe, shown in Figure 2.9. With an increase in the stiffness of the geogrid and enveloped orientation, the maximum vertical stress at the crown of the buried pipe tended to decrease.

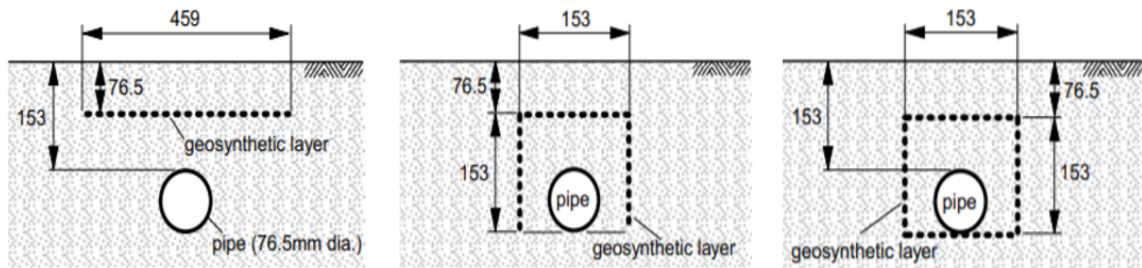


Figure 2.8. Horizontal(left), inverted U(middle), and enveloped(right) orientation (Pires and Palmeria, 2017).

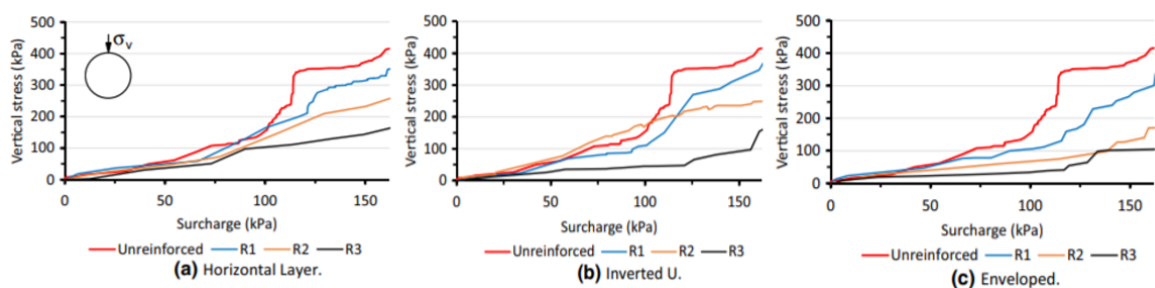


Figure 2.9. Vertical stress vs Surcharge pressure on different orientation and geogrid types (Pires and Palmeria, 2017).

Kou *et al.* (2018) conducted a series of modal load tests on a buried pipe system in a rigid tank filled with geotextile-reinforced sand. In their work, the goal was to determine whether the width of geotextiles affects the footing settlement, the pressure

distribution and the deflection along the buried pipe. In Figure 2.10, the test box with geotextile of different widths is illustrated. In the results, it was stated that there was a positive correlation between the load-bearing capacity of the foundation overlaid on geotextile-reinforced sandy soil cover over the buried pipe and the thickness of the geotextile up to  $4B_c$ , where  $B_c$  was the diameter of the buried pipe. Also, it was observed that the vertical and the horizontal deformations of the buried pipe tended to decrease with the implementation of geotextile reinforcement above the buried pipe. Those deformations were observed to decrease with an increase in the width of the geotextile reinforcement.

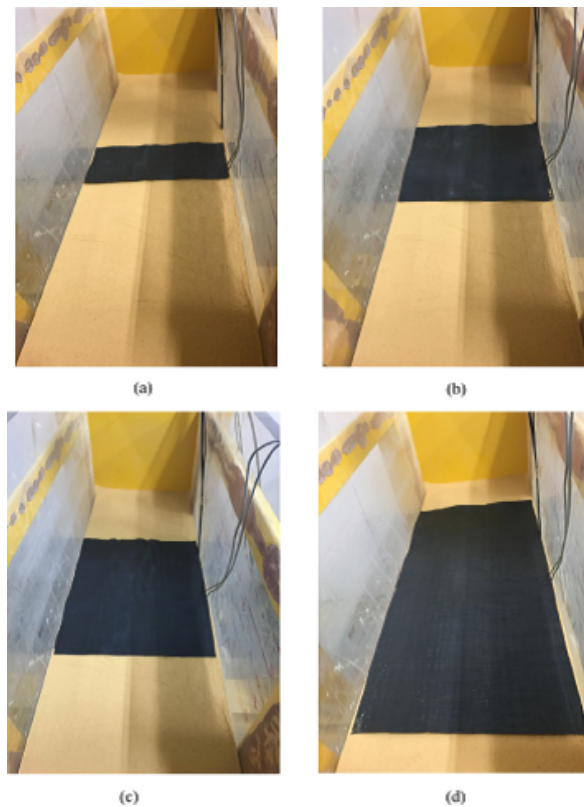


Figure 2.10. Test box and geotextiles used in the experiments (Kou *et al.*, 2018).

Ma *et al.* (2019) investigated the effects of the thickness and number of layers of EPS Geofoam on the pressure on the crown of the buried pipes and the load-reduction efficiencies of those pipes. The pipes were grouped as flexible pipes and rigid pipes. The influence of the thickness of EPS Geofoam was observed for different filling heights. In Figure 2.11, Scheme 1 is the test in which steel pipe was used with no reinforcement,

Scheme 7 is the test in which PVC pipe was tested without reinforcement. Scheme 8-11 are the results of the tests where PVC pipe was used with EPS Geofoams of different thicknesses, where thickness is represented by  $C$ . Also,  $\gamma H$  is the pressure that should be acting on the pipe according to the linear theory. The results in Figure 2.11 showed that using a flexible pipe instead of a rigid pipe decreased the pressure acting on the pipe by 26.15%. In general, the earth pressure on the crown of the pipe tended to decrease with an increase in the thickness of EPS Geofoam. The influence of EPS Geofoam thickness on load-reduction differed based on the pipe type, causing a smaller impact on rigid pipes than flexible pipes. When the EPS Geofoam thickness reached 4cm, the load reduction rate was 26.95% for rigid pipes while this value was 66.34% for flexible pipes.

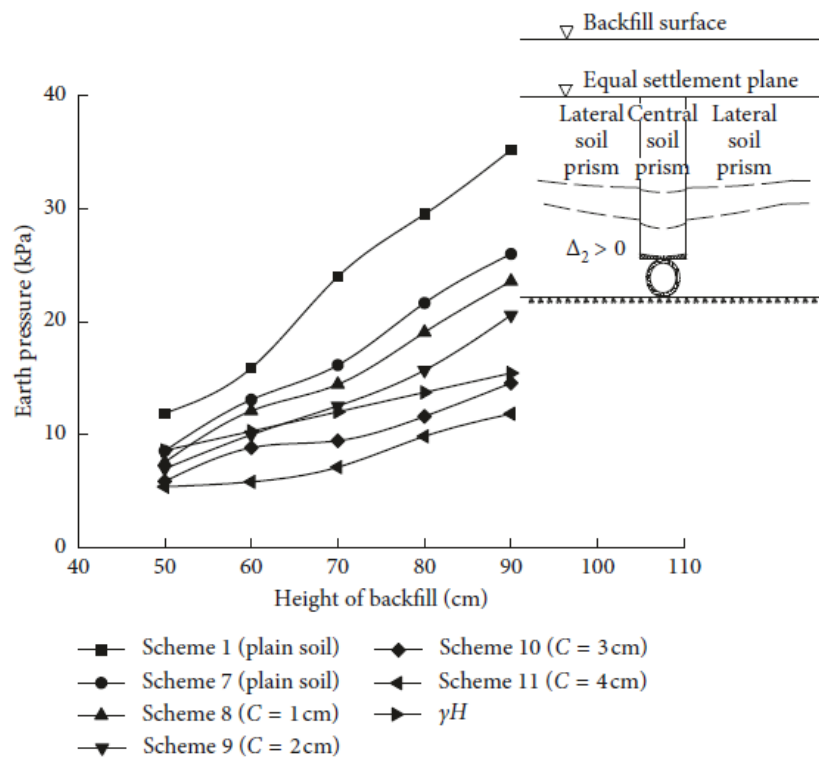


Figure 2.11. Pressure acting on the crown of the pipe vs Backfill height (Ma *et al.*, 2019).

2.2.1.2. Physical Model Tests Under Static Load Without Reinforcement. Terzi *et al.* (2012) conducted laboratory experiments to investigate the effects of relative density on the deformation behavior of buried HDPE pipes. The tests were done with three different relative density ranges. The deformation behavior of the HDPE pipes was found by two methods: electric-resistant strain gages with linear position transducers and close-range image processing by photogrammetric cameras. The results were then compared, and it was stated that they were in good correlation for all relative density ranges, as seen in Figure 2.12. In the experiments, it was observed that both the vertical deflection of the pipe crown and the lateral deflection of the springline tended to increase with the decrease in relative density. However, the ratio of vertical deflection to horizontal deflection tended to decrease with the decrease in relative density as shown in Figure 2.13.

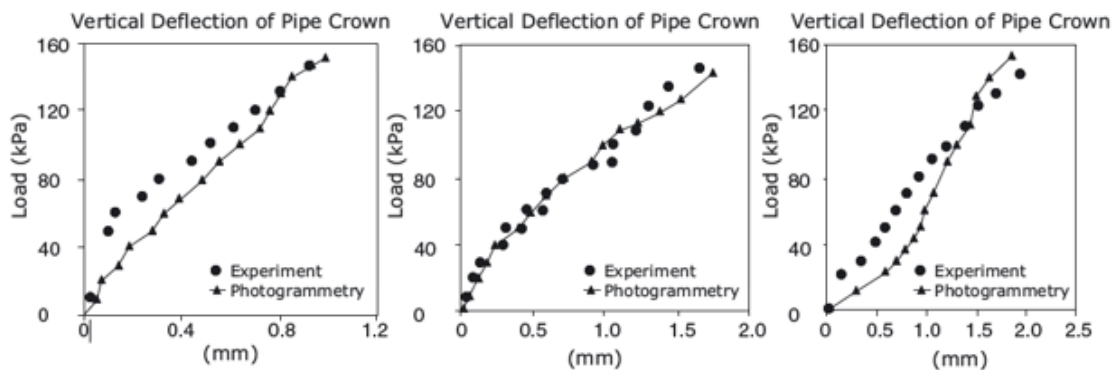


Figure 2.12. Compatibleness of the methods for different relative density ranges (Terzi *et al.*, 2012).

Condition	Vertical deflection (mm)	Lateral deflection (mm)	Ratio
Dense	0.98	0.62	1.58
Medium	1.65	1.33	1.24
Loose	1.97	1.90	1.03

Figure 2.13. Vertical and horizontal deflection of the pipe, and their ratio for different relative density ranges (Terzi *et al.*, 2012).

Bildik and Laman (2015) carried out physical model tests to find out the effects of relative density, load rate, burial depth, and horizontal distance of the pipe to the center of the foundation on the bearing capacity of the foundations laid on the soil-buried pipe systems. In Figure 2.14, the investigated parameters are illustrated, where  $H$  is burial depth,  $D$  is the diameter of the pipe,  $B$  is the foundation width, and  $x$  is the horizontal distance from the right end of the foundation to the left end of the pipe. The results in Figure 2.15 showed that BCR (bearing capacity ratio of the tested situation to the bearing capacity of the system without any pipe installation) increased almost linearly with the burial depth until  $H/D=4$ , and when burial depth reached  $H/D=5$ , the bearing capacity was almost equal to the case with no pipe installed. Another result was that with the increase in the horizontal distance from the foundation, the bearing capacity of the system increased. However, the loading rate did not have any considerable effects on the bearing capacity. Also, it was stated that the relative density increased the ultimate bearing capacity of the soil-buried pipe system. This increment was 70% for  $H/D=1$  and 85% for  $H/D=5$ .

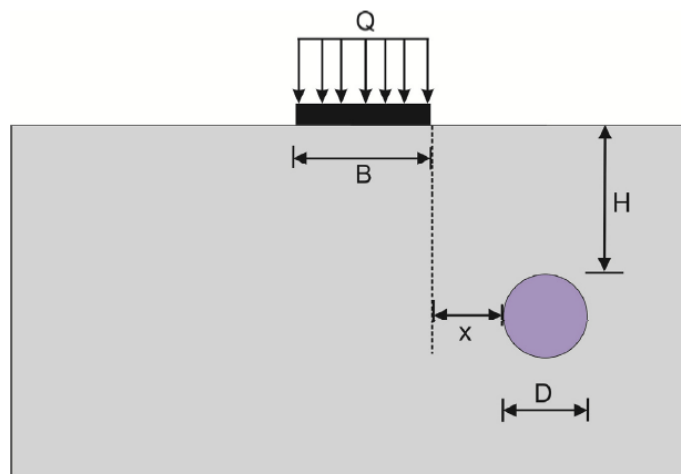


Figure 2.14. Illustration of the parameters (Bildik and Laman, 2015).

Bildik and Laman (2019) investigated the effects of the burial depth and the horizontal distance from the footing on the stresses acting on the pipe and the load-settlement behavior of the soil-pipe system by conducting physical model tests. The

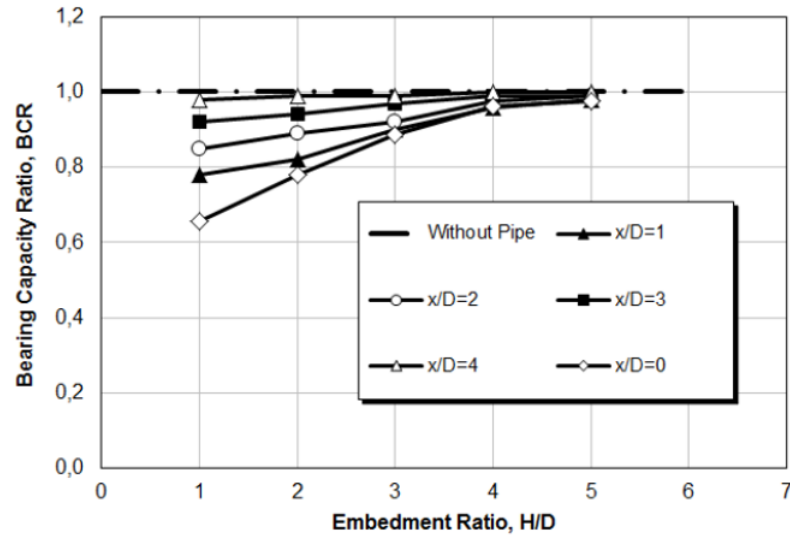


Figure 2.15. Results of the tests for different  $x$  and  $H$  values (Bildik and Laman, 2015).

stresses acting on the pipe were found by using four strain gages attached to the sides of the pipe. In general, the results showed that with an increase in the burial depth, the hoop stresses acting on the pipe decreased as shown in Figure 2.16. For the experiments in which the horizontal distance was changing while the burial depth was kept constant, different results in terms of sign of the pressure were obtained as seen in Figure 2.17. For the strain gages placed on the bottom and top parts of the pipe to record the vertical stresses, the pressure values were negative when there was no horizontal distance from the center of the pipe, meaning that there was compression. This value tended to increase and reach positive values when  $x/D=2$ , meaning that they were recording tensile pressures. The pressure acting on the pipe tended to go to zero when  $x/D=4$  condition was reached.

### 2.2.2. Physical Model Tests Under Dynamic Load

Moghaddas Tafreshi and Khalaj (2008) conducted physical model tests to demonstrate the effects of vehicle loading on buried pipes. The test box in Figure 2.18 was backfilled with sand with three different relative density values and a different num-

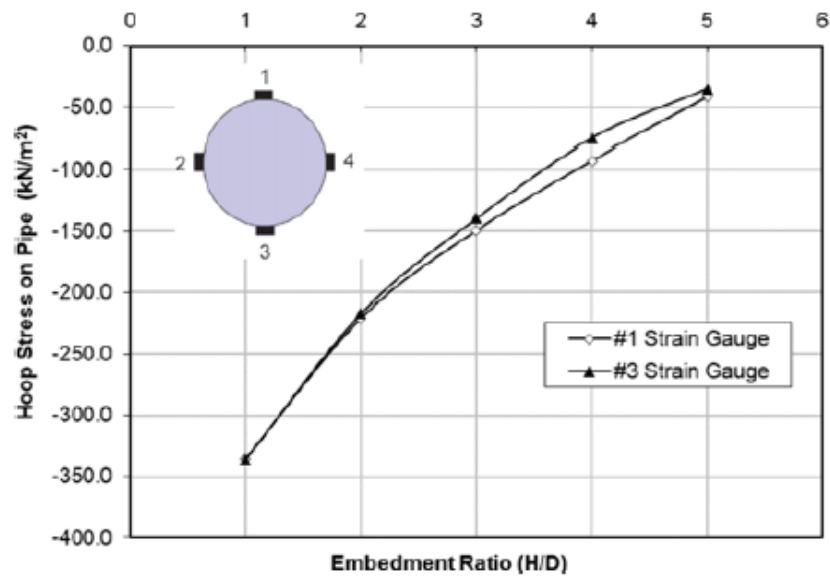


Figure 2.16. Change in hoop stress with embedment ratio (Bildik and Laman, 2019).

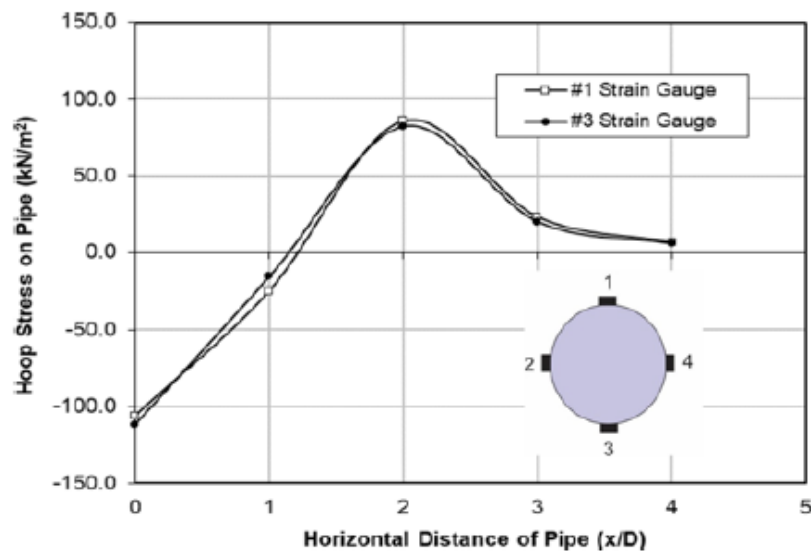


Figure 2.17. Change in hoop stress with horizontal distance (Bildik and Laman, 2019).

ber of geogrid-reinforcement. These variables were also tested for four different burial depths. According to the results;

- With the implementation of geogrid reinforcement, both the pipe and the soil deformations decreased.
- The optimum conditions were reached when the first reinforcement having a width five times the pipe width was buried to  $0.35B$ , where  $B$  is the foundation width.
- With the increase in the relative density of the soil backfill, the deformations in both the pipe and the foundation decreased.

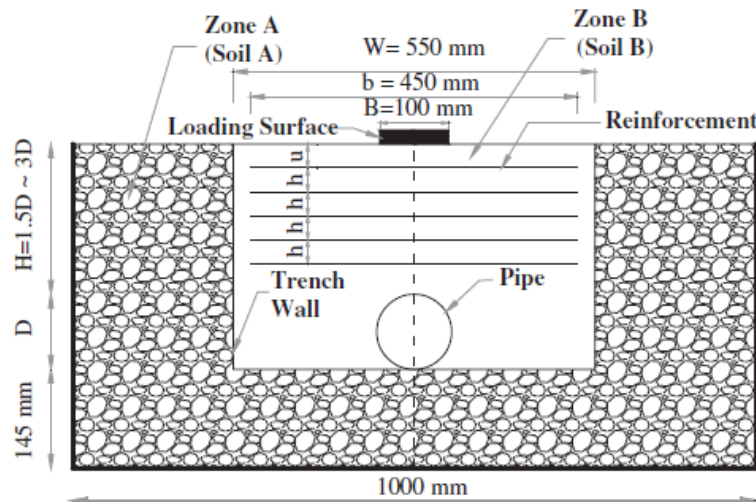


Figure 2.18. Layout of the reinforcements and buried pipe (Moghaddas Tafreshi and Khalaj, 2008).

Khalaj *et al.* (2017) conducted physical model experiments to investigate the effects of the thickness and density of EPS Geofom on the behavior of flexible PVC pipes. A pressure of 450kPa with a frequency of 0.33Hz was applied using a plate. Sketch of the testing system is illustrated in Figure 2.19. Data was collected from the test system to record the vertical diameter strain and the pressure acting on the crown of the pipe. An increase in EPS block thickness and density led to a decrease in both the vertical diameter strain and the circumferential crown strain.

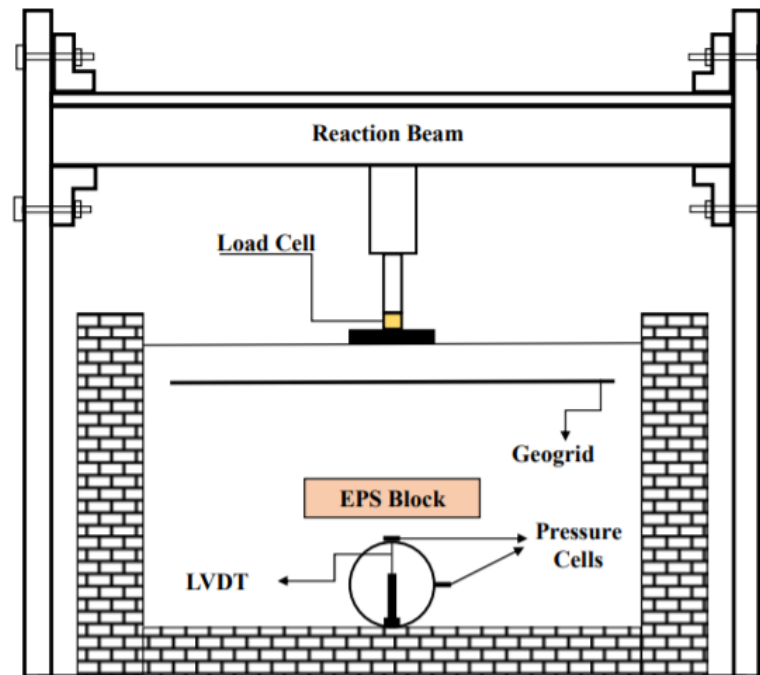


Figure 2.19. Testing system used in the experiments (Khalaj *et al.*, 2017).

Fattah *et al.* (2018) performed laboratory experiments to observe the behavior of buried PVC pipes under dynamic loading. The dynamic loading was applied with amplitudes of 0.5 and 1 ton and frequencies of 0.5, 1, and 2Hz. The pipes were buried in a box backfilled with two layers(subbase and base), consisting of sand with different relative densities. Sketch of the testing system can be seen in Figure 2.20. The geocell reinforcement was installed between the subbase and the base layers. The effects of reinforcement were investigated by comparing the reinforced case with the unreinforced case. In conclusion, it was stated that the geocell reinforcement significantly enhanced the performance of the system by reducing the vertical stress acting on the pipe by 41%, the vibration of the pipe by 35%, and the settlement in the crown of the pipe decreased by 25-35%. The crown displacement and the vertical stress acting on the pipe increased with a higher load frequency. The authors also validated their results by creating a numerical model and comparing the experimental results with the numerical model, which proved a good correlation.

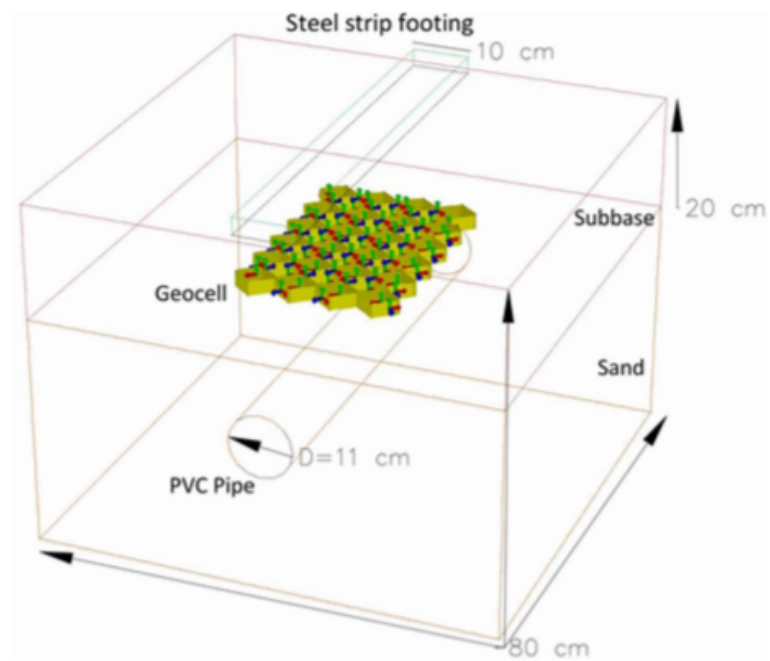


Figure 2.20. Layout plan of the geocell reinforcement and buried pipe (Fattah *et al.*, 2018).

### 2.3. Usage of PIV Method in Geotechnical Engineering

Particle image velocimetry (PIV) method is used to investigate the differentiations between an image and the sequence of the other images. Originally, PIV technique was used to track deformations in fluid mechanics, then it was adopted for geotechnical engineering applications. In fact, as the soil grains have textures, identification of the displacements in soil backfills is easier than fluid mechanics applications. PIV analysis is done by the geoPIV(White *et al.*, 2003) and geoPIV\_RG(Stanier *et al.*, 2016) programs, which are image analysis modules for MATLAB. The analysis starts with determination of an area of interest(AOI) that should encompass the area of deformations. This AOI is then divided into a grid of square patches. The area of those square patches is dependent on the user's choice. There is a dilemma in the choice of the square patch area. If the patch area is chosen too small, the computation time increases. Also, although the decrease in the patch area enables the user to see more details, a very small patch size may impede the recognition of the differences. On the other hand, increasing the patch size leads to a decrease in the computation time. Nonetheless, if the patch size is too large, the crudeness of the analysis increases, meaning that the details may be missed. To investigate this dilemma, Altunbas (2015) analyzed six different patch sizes for the same analysis, as seen in Figure 2.21.

After creating a mesh from the reference image and creating sub-meshes called patches, the program starts to evaluate the differences in each patch with the adjacent picture and creates a displacement vector. Fast Fourier Transform (FFT) method is used in the correlation operations for the evaluation of the differences. This assessment continues for each patch defined in the AOI. Afterwards, this procedure is repeated for the subsequent images in series. After the analysis come to an end, it is possible to see the differences between each picture as a vector field or as a map that consists of different colors that indicate the amount of displacement, volumetric strain, or shear strain. Unit in the analysis is defined as pixels, as default. To convert pixels to centimeters or any other parameters, control markers can be added to the system. Control markers are points which have pre-determined distances and are stable points

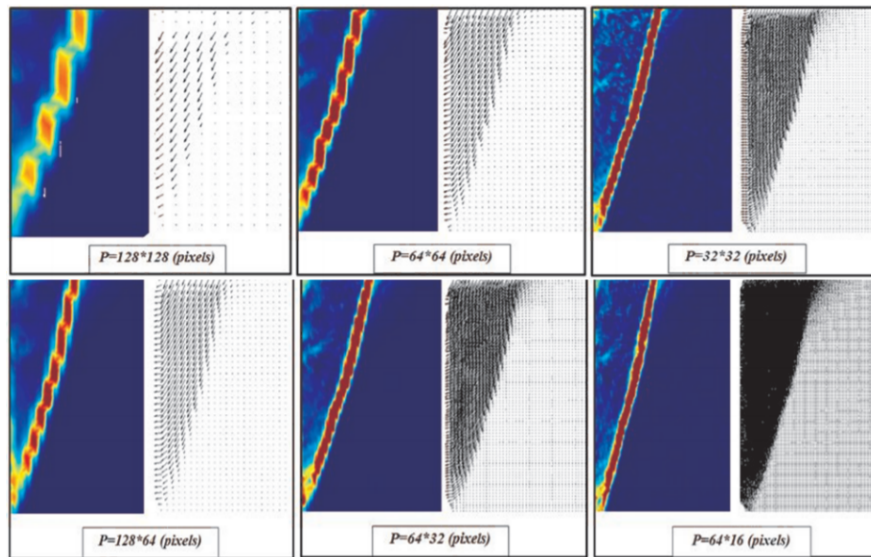


Figure 2.21. Changes in the analysis results with the patch sizes (Altunbas, 2015).

meaning that they are not affected from the deformations in the system. In the analysis, differences in the distance of these control points can be obtained in terms of pixels, which enables the conversion of the necessary properties from pixels to the desired units. Some of the contemporary researches in which PIV analysis was used are exemplified below.

Mirzababaei *et al.* (2017) examined the effects of waste carpet fibers as a reinforcement on clay soil slopes. This was done by changing fiber content of the waste carpet and distance between crest of the slope and footing edge. Pictures of the tests were taken and analyzed via PIV method to understand the deformation behavior by illustrations, shown in Figure 2.22. In the results, the authors stated that fiber reinforcement improves the bearing capacity of the slopes considerably. Also, a reduction in the deformation of the slope in both vertical and horizontal directions was observed because of the use of fibers that created interlocking with soil fibers. Besides, it was indicated that using 1% fiber improvement did not result in a considerable change in the bearing capacity of the system.

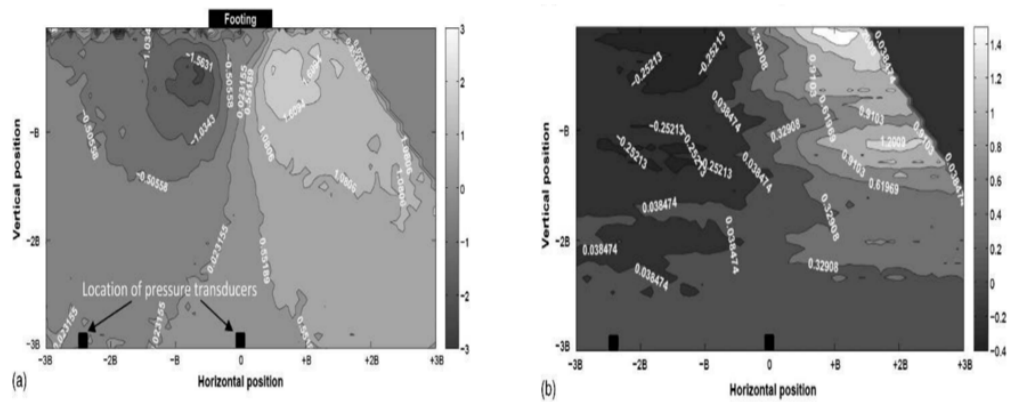


Figure 2.22. PIV analysis results (Mirzababaei *et al.*, 2017).

Ghalehjough *et al.* (2018) tested three different sand types and three different relative density values to investigate the effects of particle roundness and morphology on the failure surface mechanism under a strip foundation. Pictures were taken with 30-second intervals while the tests were being conducted. Then, the pictures were analyzed via geoPIV software to find out the soil displacement. In Figure 2.23, it can be seen that with the increase in relative density, a more intensive soil displacement was observed. Also, a change in particle size resulted in a change in the soil displacement field.

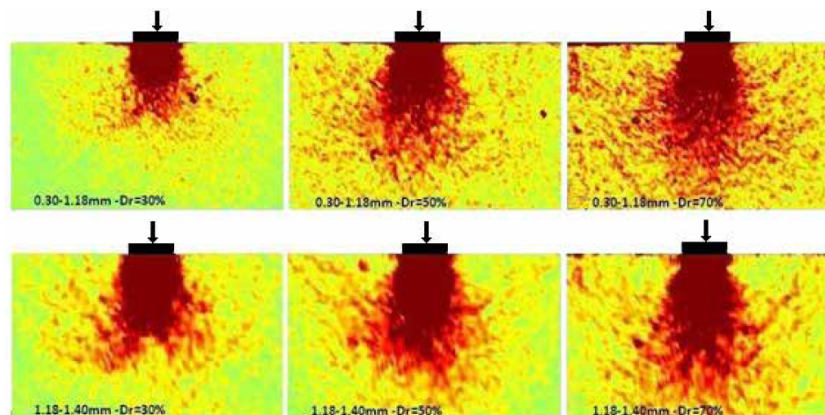


Figure 2.23. PIV analysis results for different relative density and particle size values (Ghalehjough *et al.*, 2018).

Zhang and Askarinejad (2018) conducted physical model tests to examine the effects of the position of the pipe and grain-size distribution on the behavior of pipes in unstable sandy slopes. Tests were done using the centrifugal testing machine that created an acceleration of 300 times the gravitational acceleration. Two types of sand were tested: coarse grained and fine grained. Samples were prepared with the implementation of dry pluvization technique. Test set-up can be seen in Figure 2.24. PIV method was used to illustrate those deformations and failure surfaces of the slopes. In the results, it was proposed that pipes installed near the failure surfaces of the slopes undergo larger displacements. It was also stated that while determining the bearing capacity factors of the buried pipes, slope angle and burial distance to the top of the crest should be taken into consideration.

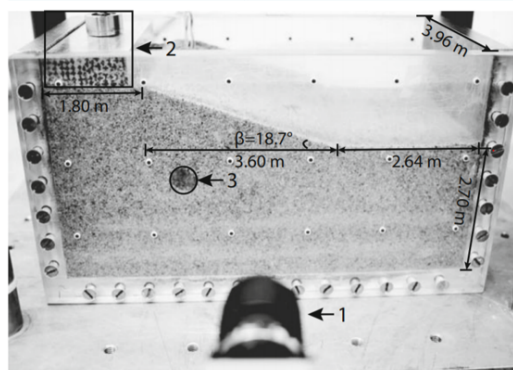


Figure 2.24. Test set-up, (1) high-resolution camera, (2) footing and load cell, (3) buried pipe (Zhang and Askarinejad, 2018).

Chen *et al.* (2019) performed numerical and physical model experiments to find out the effects of pile spacing on the deformation characteristics of pile groups installed in dense sand. While the test was being conducted, photographs were taken in different deformation ratios and analyzed via PIV method in MATLAB. Some PIV analysis outputs are illustrated in Figure 2.25. With this analysis, displacement fields were created for the pile groups having  $3b$  and  $6b$  pile spacing, where  $b$  is the width of the pile. In the results, it was shown that a decrease in pile spacing increases pile tip resistance and bearing capacity of the pile group, while an increase in pile spacing leads

to higher group composite efficiency.

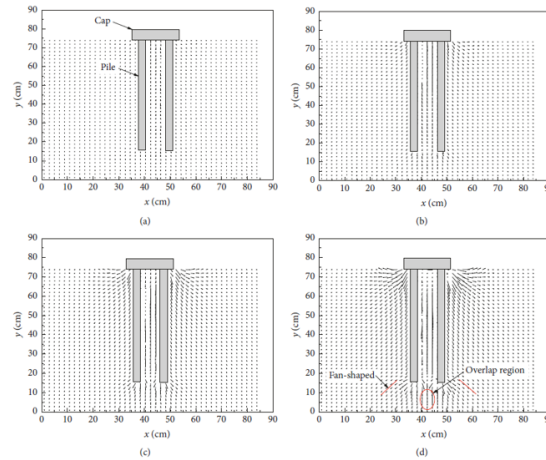


Figure 2.25. PIV Analysis results as displacement vectors (Chen *et al.*, 2019).

Martinez *et al.* (2019) carried out interface shear box tests to find out the effects of behavior of snakeskin-inspired surfaces on the soil strength parameters and deformations. To do that, 19 different bio-inspired surfaces were created by 3-D printing. Tests were done in two different sand groups and two different directions: cranial direction and caudal direction, shown in Figure 2.26. In the results, it was indicated that shearing in the cranial direction leads to a higher peak and residual interface strength and dilation than shearing in the caudal direction. Also, PIV method was used to examine the soil deformations. With PIV analysis, shown in Figure 2.27, larger deformations and dilation were observed in the soil when it was sheared in the cranial direction compared to caudal direction.

Oner *et al.* (2019) conducted physical model tests on a rigid retaining wall to find the effects of particle size and shape on the active failure surface geometry. Tests were done under different relative density and surcharge pressure values to generalize those effects. While tests were being conducted, pictures were taken by a high-resolution camera and analyzed with PIV method via MATLAB. Some of the results are demonstrated in Figure 2.28. The analysis showed that an increase in relative density and a decrease in surcharge pressure lead to a steeper failure surface. Also, an increase

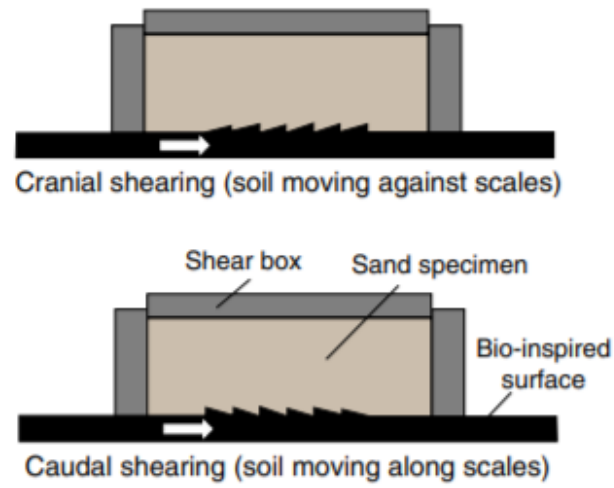


Figure 2.26. Cranial and caudal directions (Martinez *et al.*, 2019).

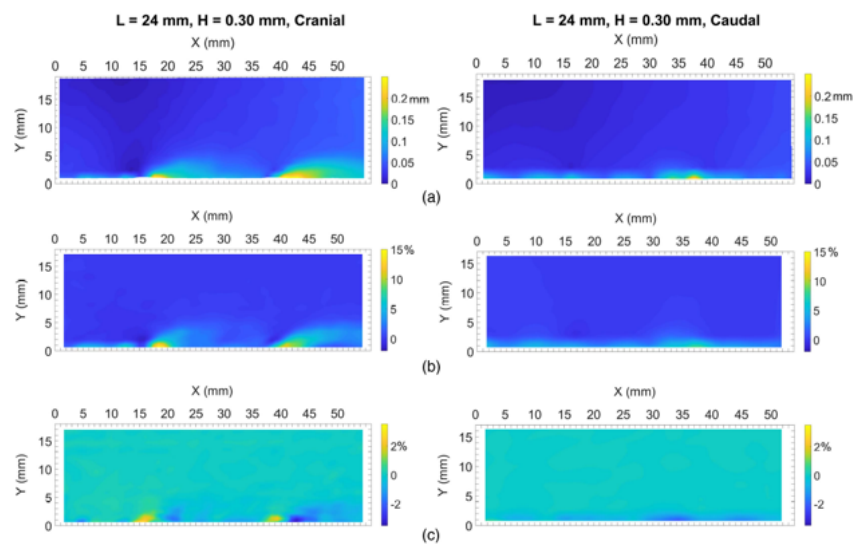


Figure 2.27. PIV Analysis, (a) resultant displacement, (b) shear strains, (c) volumetric strains (Martinez *et al.*, 2019).

in angularity and uniformity coefficient of the tested sands leads to an increase in the failure surface angle.

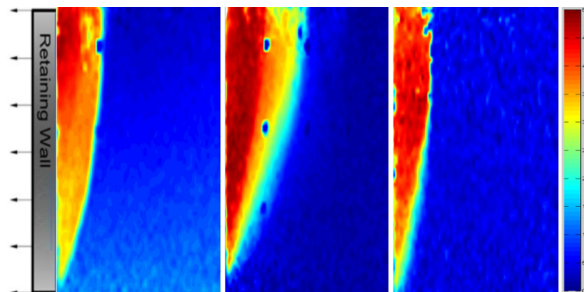


Figure 2.28. Displacement fields found by PIV analysis (Oner *et al.*, 2019).

## 2.4. Types of Failure Under Shallow Foundations and Failure Surfaces

Under the application of load, soil beneath the foundation undergoes deformation. Depending on the properties of this soil, different types of failure and failure surfaces occur. In this section, types of failure are explained briefly.

### 2.4.1. General Shear Failure

- Failure occurs in soils that are strong and have relatively low compressibility such as rocks, dense sand, and saturated and normally consolidated clays that are loaded undrained.
- Failure occurs rapidly.
- A well-defined failure surface can be observed as in Figure 2.29.
- A clear peak load value can be identified in the load-settlement graph, shown in Figure 2.30.

### 2.4.2. Punching Shear Failure

- Failure occurs in very loose sands and weak clays under drained loading conditions.

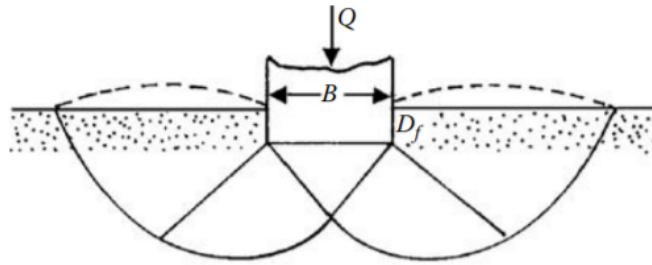


Figure 2.29. General shear failure (Das, 2017).

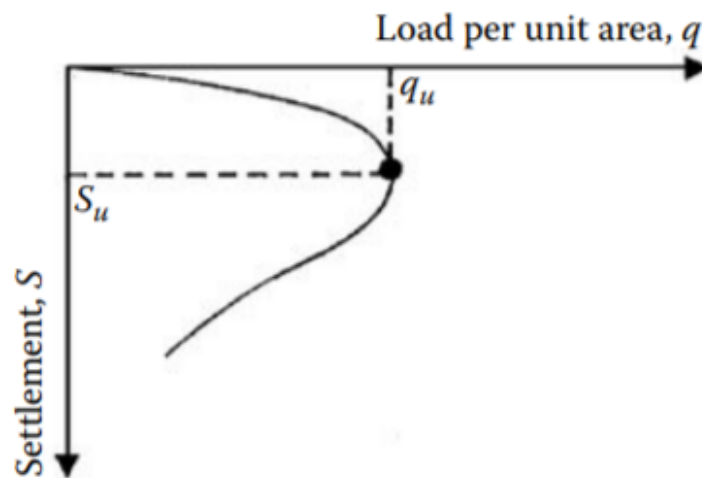


Figure 2.30. Load-Settlement graph for the general shear failure (Das, 2017).

- Failure occurs gradually.
- No bulging occurs at the ground surface as illustrated in Figure 2.31.
- In load-settlement graph, a peak load value cannot be observed. The ultimate load is defined as the point where the ratio of the change in settlement to change in load value reaches the largest value and remains constant thereafter. Load-settlement graph is illustrated in Figure 2.32.

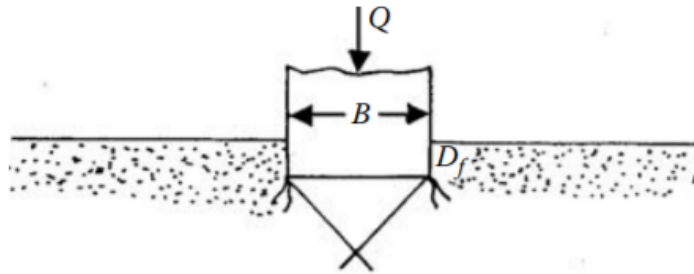


Figure 2.31. Punching shear failure (Das, 2017).

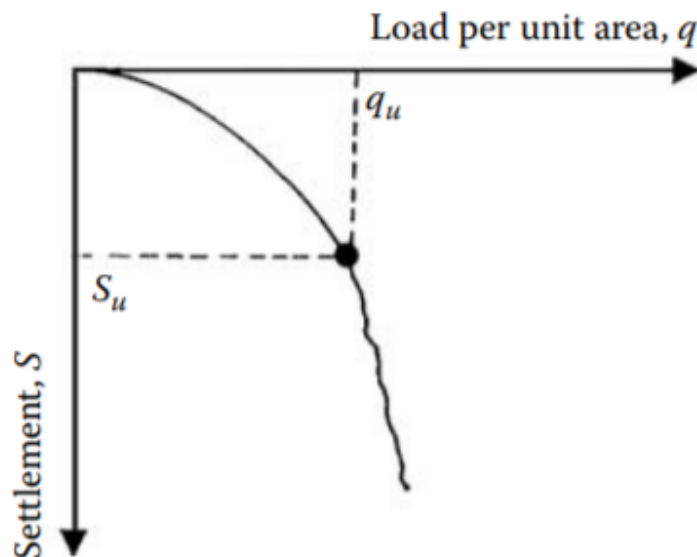


Figure 2.32. Load-Settlement graph for the punching shear failure (Das, 2017).

### 2.4.3. Local Shear Failure

- Failure can be considered as the intermediate case between general and punching shear failure.

- Like the punching shear failure, sudden failure is not observed.
- Although shear surfaces are well defined under the foundation as in the case of general shear failure, it becomes ambiguous near the ground surface. Failure is illustrated in Figure 2.33.
- Peak load interpretation is difficult. Two peak loads are defined in local shear failure. First peak load is defined as the point where an erratic and steeper increase is observed thereafter. Second peak load is defined as the load corresponding to the maximum settlement. This is illustrated in Figure 2.34.

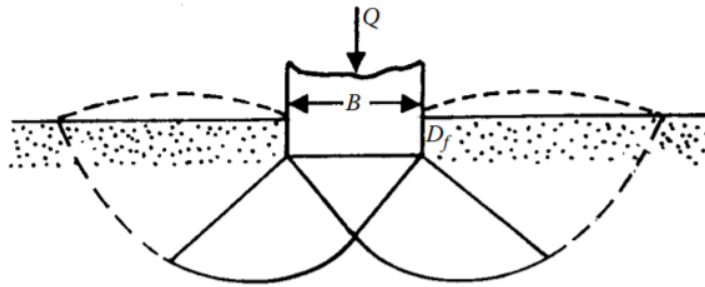


Figure 2.33. Local shear failure (Das, 2017).

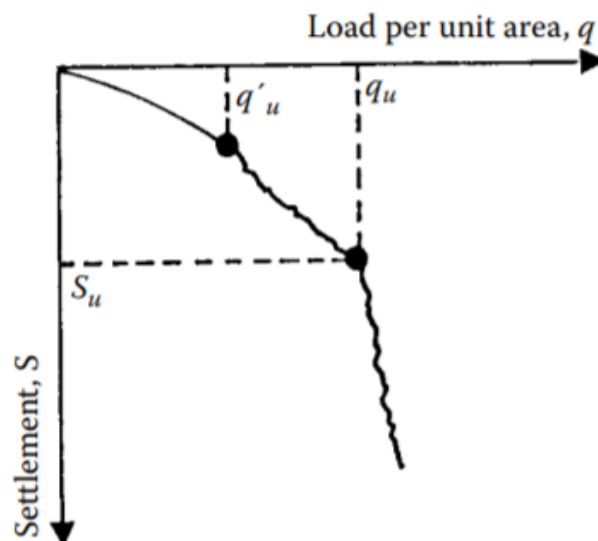


Figure 2.34. Load-Settlement graph for the local shear failure (Das, 2017).



In Figure 2.35,

- B is width of foundation.
- $D_f$  is the depth of foundation.
- $\gamma$  is the unit weight of the backfill.
- $\phi$  is the friction angle of the backfill.
- q is the surcharge pressure.

Failure surface is divided into three regions;

- Region abc: This zone is the triangular elastic zone located below the foundation. Line ac and bc makes an angle of  $\phi$  with the horizontal.
- Region bcf: This zone is called as the Prandtl's radial shear zone. Length of any line starts from the point b to any point in curve cf can be found by using Equation 2.1;

$$r = r_0 e^{\theta \tan \phi} \quad (2.1)$$

where,

- $r_0$  is the length of line ac or bc.
- r is the length of any line between point b and any point in curve cf.
- $\phi$  is the friction angle.
- $\theta$  is the inclination between  $r_0$  and bc.
- Region bfg: This zone is called as the Rankine passive zone. Lines bf and fg make an angle of  $45 - (\phi)/2$  with the horizontal.

It should be noted that Region bcf and bfg are also located to the left of region abc, although not seen in Figure 2.35. Based on this failure surface, Terzaghi (1943) proposed an ultimate bearing capacity equation, shown in Equation 2.2. Bearing capacity coefficients ( $N_q, N_c, N_\gamma$ ) in Equation 2.2 are defined in Equation 2.3, Equation



- Region abc: This zone is the triangular elastic zone located below the foundation.
- Region bcd: This zone is called radial shear zone.
- Region bde: This zone is the mixed shear zone in which shear differs among the limits of radial and plane shears that alters with the depth and roughness of the foundation.

Ultimate bearing capacity equation is the same with the Terzaghi's (1943) equation, the only change being the Terzaghi's coefficients, shown in Equation 2.6 and Equation 2.7:

$$N_q = e^{\pi \tan \phi} \left( \frac{1 + \sin \phi}{1 - \sin \phi} \right) \quad (2.6)$$

$$N_c = (N_q - 1) \cot \phi \quad (2.7)$$

To find  $N_\gamma$ , even though charts can be used, Meyerhof (1963) recommended to use the following approximation formula to determine  $N_\gamma$ , shown in Equation 2.8.

$$N_\gamma = (N_q - 1) \tan (1.4\phi) \quad (2.8)$$

However, there has been an ongoing discussion about the theoretical values of  $N_\gamma$ . In Table 2.1, the proposed  $N_\gamma$  values for different friction angles can be seen;

As seen in the Table 2.1,  $N_\gamma$  values differ significantly with the different analysis methods.

There are also other bearing capacity and failure surface theories. Hu (1964) proposed a theory in which the angle  $\alpha$  in Figure 2.35 is not equal to the friction angle, but it is a function of several parameters including the unit weight of the backfill, friction angle, and surcharge pressure. There are some boundaries in the value of  $\alpha$ ,

Table 2.1. Comparison of  $N_\gamma$  values.

Friction Angle	Terzaghi (1943)	Meyerhof (1951)	Vesic (1973)
0°	0.00	0.00	0.00
5°	0.14	0.07	0.45
10°	0.56	0.37	1.22
15°	1.52	1.13	2.65
20°	3.64	2.87	5.39
25°	8.34	6.77	10.88
30°	19.13	15.67	22.40
35°	45.41	37.15	48.03
40°	115.31	93.69	109.41

shown in Equation 2.9 and Equation 2.10:

$$\phi < \alpha_{min} < 45 + \frac{\phi}{2} \quad (2.9)$$

$$\alpha_{max} < 45 + \frac{\phi}{2} \quad (2.10)$$

Ultimate bearing capacity by this method can be found by using Terzaghi's (1943) bearing capacity equation; however, bearing capacity coefficients should be found from the charts proposed by Hu (1964).

Balla (1962) proposed another bearing capacity theory and failure surface as illustrated in Figure 2.37.

For this failure surface, the curve cd is considered to be an arc of a circle having a radius r, rather than a logarithmic spiral. Again, bearing capacity can be found by using Terzaghi's (1943) bearing capacity formula; however, the appropriate bearing capacity coefficients should be used from the charts proposed by Balla (1962).

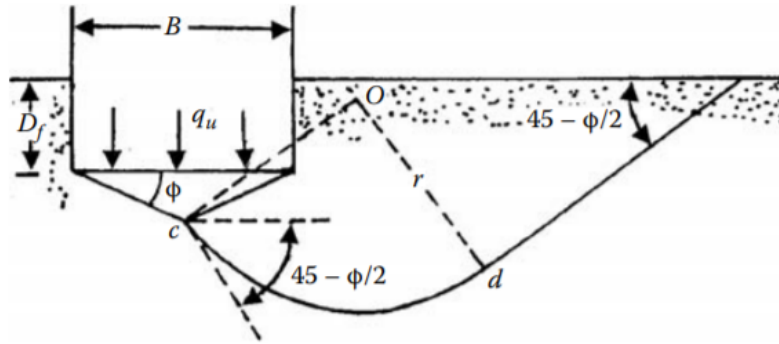


Figure 2.37. Failure Surface (Balla, 1962).

Those failure surface and ultimate bearing capacity estimations were done considering that governing failure type is the general shear failure. Vesic (1973) proposed a graph, shown in Figure 2.38, to determine the type of shear failure based on the relative density of the backfill and ratio of the depth of foundation to the width of foundation.

Although failure surfaces for punching and local shear failures are not clearly identified, ultimate bearing capacity for local shear failure can be found using the Vesic's (1973) method. Vesic (1973) suggested to use a modified friction angle for the estimation of the modified bearing capacity factors. The modified friction angle can be found using the Equation 2.11 and Equation 2.12:

$$\phi' = \tan^{-1}(k \tan \phi) \quad (2.11)$$

$$k = 0.67 + I_D - 0.75 I_D^2 \quad (2.12)$$

In Equation 2.12,  $k$  is the reduction factor which is valid for  $0 \leq I_D \leq 0.67$ . After determining the modified friction angle ( $\phi'$ ), the charts for bearing capacity coefficients for general shear failure can be used to determine the ultimate bearing capacity for local shear failure.

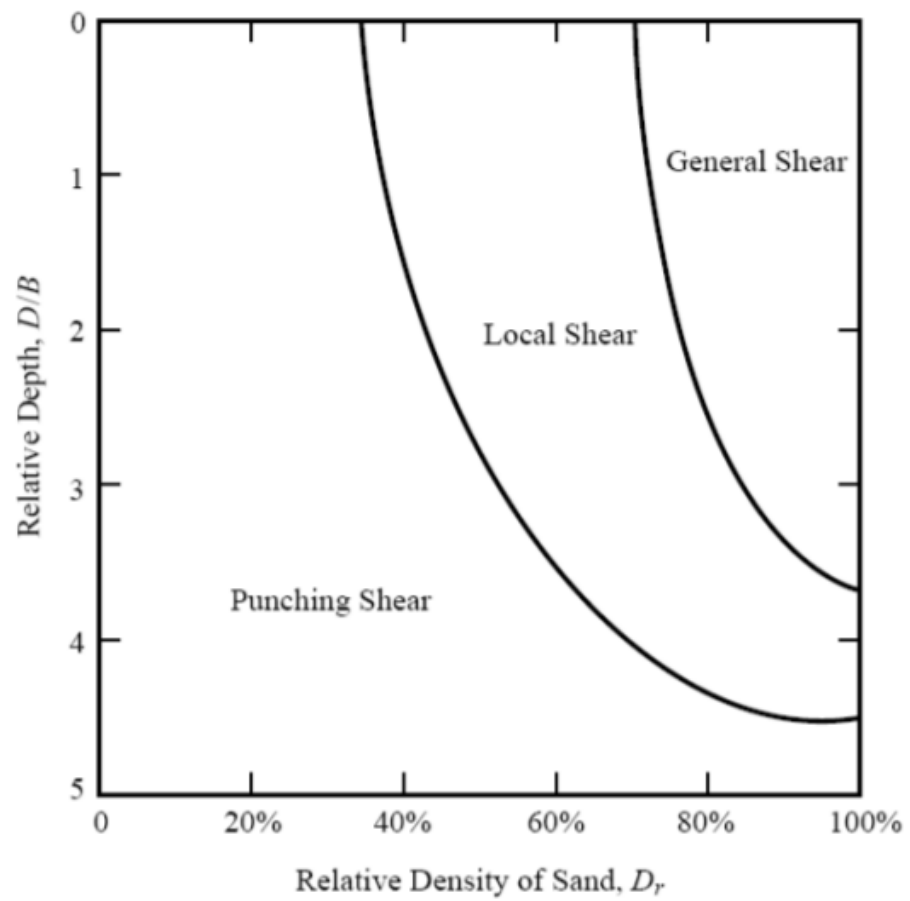


Figure 2.38. Determination of the type of failure (Vesic, 1973).

### 3. METHODOLOGY

#### 3.1. Experiment Setup

##### 3.1.1. Test Box

Experiments were conducted in a rigid box with the dimensions of 100cm x 50cm x 65cm(length x width x depth). Lower surface of the box is completely steel, and there are four steel sections that are attached perpendicular to the lower box. Those are connected at the top of the surface by other four steel sections. The front and rear parts of the box are 10mm glass protected by 3mm plexiglas. This glass surface enabled the author to observe the deformations while the test was being conducted. There are lines with 5cm intervals on the rear glass to check whether the expected relative density was reached or not while the sand was being poured to the box. Test box can be seen in Figure 3.1.

##### 3.1.2. Model Footing

All the experiments were done with the same model footing. A rigid steel plate with the dimensions of 50cm x 10cm x 3cm(length x width x depth) was used as a footing, shown in Figure 3.2. To observe the deformations in the sand, the footing was kept in touch with the front glass by the use of a rubber to sweep off the sand particles during deformation. This was achieved by using, a spring-system consisting of an L-shaped steel plate, a rubber, and springs, as seen in Figure 3.3. One side of the spring system was attached to the footing, and the other side was attached to the L-shaped steel plate. A rubber that fits to the lower part of this L-shaped plate was manufactured to prevent the plexiglas surface from straching. This L-shaped plate and rubber were pushed inside the hollow, and a screw placed on top of the footing was tightened to hold the L-shaped plate and rubber inside the hollow, shown in Figure 3.4. The screws were loosened when the footing was placed inside the test box, which

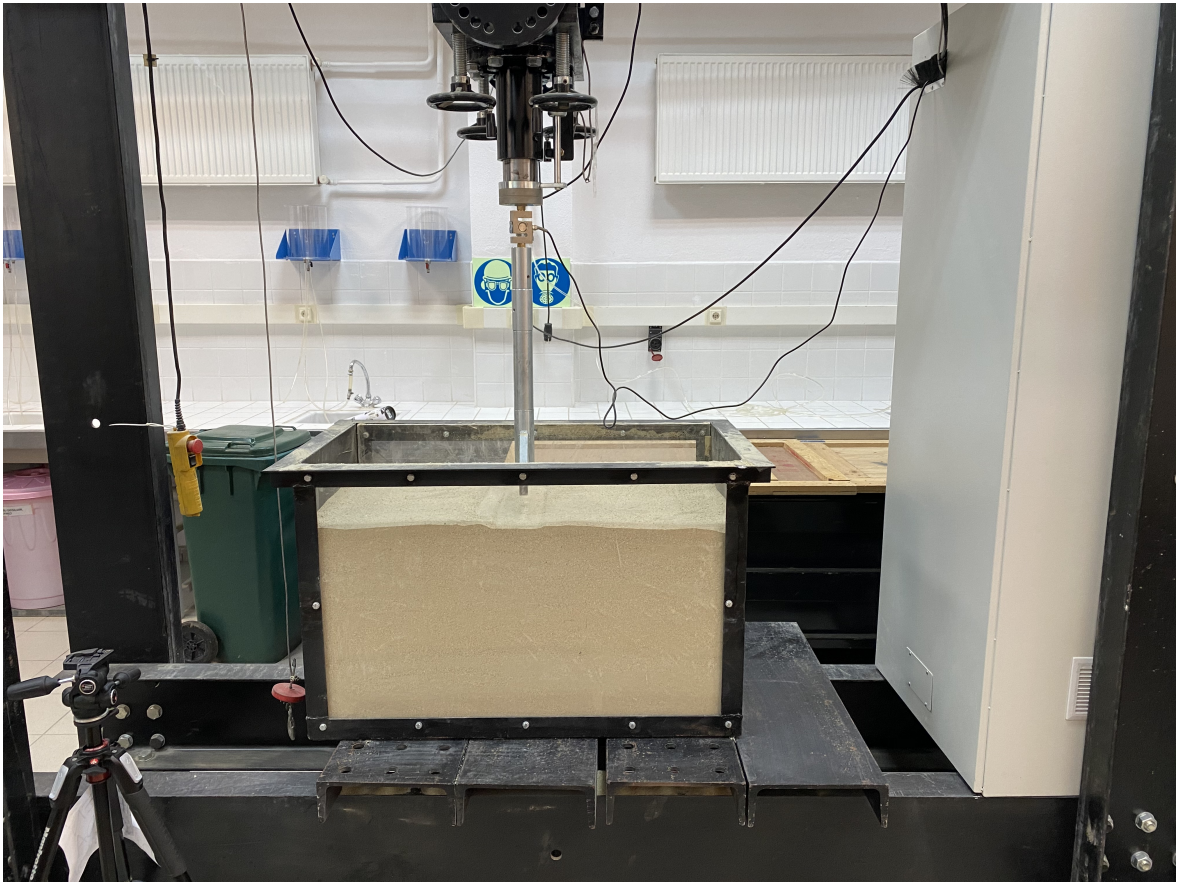


Figure 3.1. Test box used in the experiments.

enabled a contact between footing and plexiglas surface due to the force in the springs.

To make a uniform distribution of load, the three lines of 1.5-cm-diameter grooves were burrowed, and three steel marbles were placed in the middle hollow of each line, as seen in Figure 3.4. One marble was at the center of the footing, and the other two were placed 1.6cm apart from the middle one. The unused grooves were prepared in case test with eccentrically loaded foundations are conducted.

To distribute the applied load evenly to the steel marbles, a hexagonal rigid steel plate shown in Figure 3.5 was manufactured. This plate was attached to a hollow cylindrical steel piston, and this piston was attached to the load cell and the loading frame.

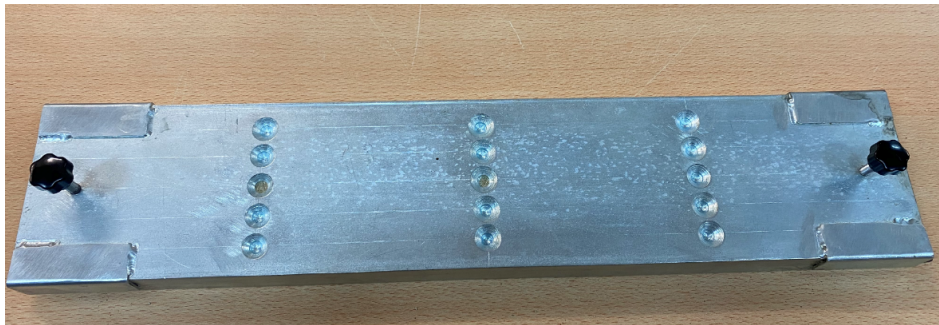


Figure 3.2. Model footing used in the experiments.

### 3.1.3. Linear Variable Differential Transformers(LVDTs)

In the tests, deformations caused by the loading of the model footing were measured by LVDTs manufactured by Yordam Test&Measurement Firm. Two different LVDTs were used in the experiments; one of them was capable of measuring displacements up to 100.00mm and the other was 150.00mm. These LVDTs are shown in Figure 3.6. The two LVDTs were placed on the each end of the long edge of the footing. Average of the readings of the LVDTs were used in the analyses.



Figure 3.3. Spring system used in the experiments.

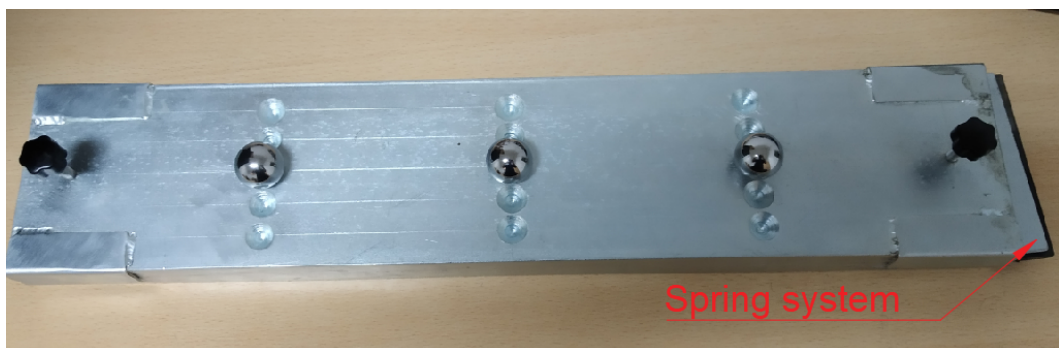


Figure 3.4. Location of the spring-system in model footing.



Figure 3.5. Hexagonal steel plate used in the experiments.

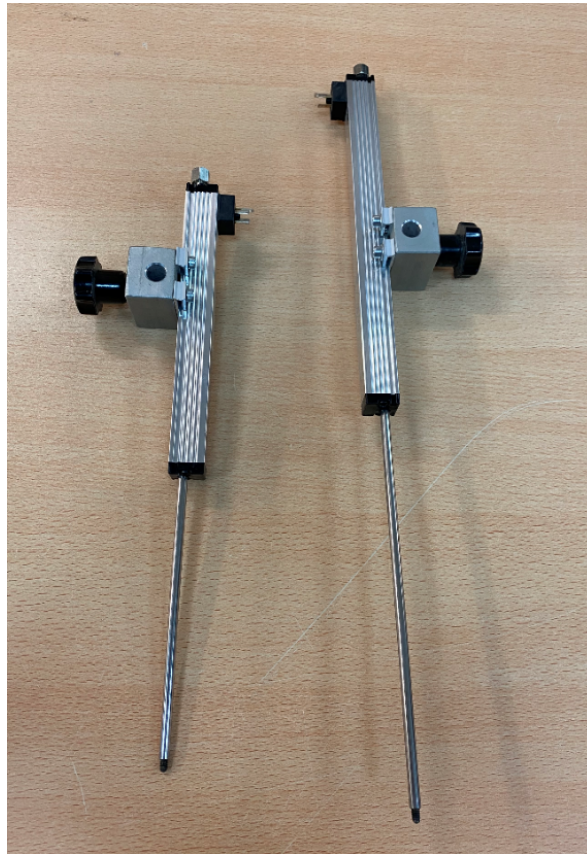


Figure 3.6. LVDTs used in the experiments.

### 3.1.4. Load Cell

In the tests, loads acting on the model footing were measured by a load cell manufactured by Yordam Test&Measurement Firm. The S-type load cell was made from alloy steel and coated with nickel to make it suitable for harsh working conditions. Load cell can be used in both compression and tension tests. Technical properties of the load cell are presented in Table 3.1, and the picture of the load cell is shown in Figure 3.7.

Table 3.1. Properties of the load cell.

Property	Units	Explanation
Precision Class	-	C3
Capacity	kg	500
Input Resistance	$\Omega$	$385\pm 10$
Output Resistance	$\Omega$	$350\pm 3$
Isolation Resistance	$M\Omega$	$^{\circ} \geq 5000$
Compansated Temperature Interval	$^{\circ}$	-10~+40
Working Temperature	$^{\circ}$	-35~+65
Recommended Supply Voltage	V(DC)	5-12
Maximum Supply Voltage	V(DC)	15
Overloading Capacity	%FS	150

Calibration of the load cell was done by another load cell. Load was increased by 10kg intervals up to 100kg, and the resistance value read by load cell was recorded for each increment. By taking the average of the readings from the load cell, the calibration was accomplished. Observed response was linear as shown in Figure 3.8.

### 3.1.5. Strain Gages

To measure the strains in the buried pipes and to calculate resulting stresses, strain gages were used in the experiments. Strain gages were manufactured by Tokyo

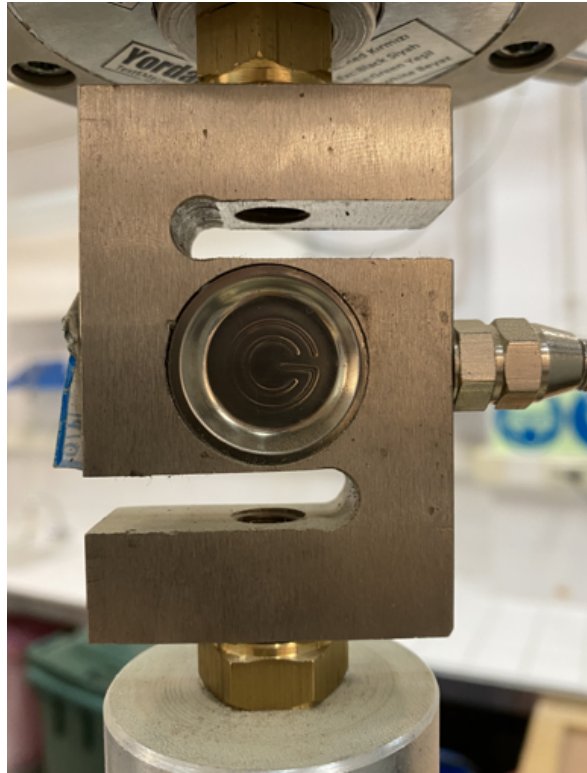


Figure 3.7. Load cell used in the experiments.

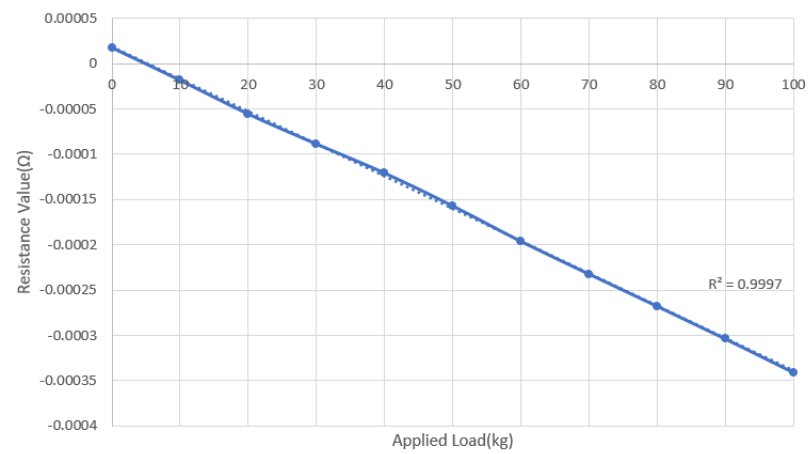


Figure 3.8. Calibration of the load cell.

Sokki Firm, and the GFLA-6-50 model was used as it is the one appropriate for flexible pipes, shown in Figure 3.9. Strain gages were glued to the pipes by a special glue manufactured by Tokyo Sokki Firm with the model number being 4A13A, shown in Figure 3.10. To protect strain gages while loading, a protection band manufactured by Tokyo Sokki Firm was stuck over those strain gages.



Figure 3.9. Strain gages used in the experiments.



Figure 3.10. Special glue used in the experiments.

Working mechanism of the strain gages is based on the change in the electrical resistance due to bending or stretching of the strain gage. This change in the electrical

resistance was then read by data acquisition system, and with the implementation of the conversion formulas, the strain on the strain gage and, therefore, on the pipe was recorded. The conversion formula can be found in Equation 3.1:

$$GF = \frac{\Delta R/R}{\Delta L/L} = \frac{\Delta R/R}{\epsilon} \quad (3.1)$$

where,

- GF is the ratio of the fractional change in electrical resistance to the fractional change in length or, in other words, to strain.
- R is the nominal gage resistance, defined as the resistance of strain gage when no strain is imposed.

Both GF and R values were given as the properties of the strain gages, as shown in Table 3.2. After obtaining strain values, the pressure on the pipe was found with the implementation of the Hooke's Law. Hooke's Law is shown in Equation 3.2:

$$\sigma = E\epsilon \quad (3.2)$$

Table 3.2. Strain gage properties.

Property	Units	Value
<b>Gage Factor</b>	-	2.09±1%
<b>Gage Resistance</b>	Ω	120.8±0.5
<b>Gage Length</b>	m	6
<b>Lead Wire</b>	-	10/0.12 4m
<b>Transverse Sensitivity</b>	-	1.0%
<b>Temperature Correction For</b>	10 <sup>-6</sup> /°C	50

In the tests, strain gages were stuck onto the pre-determined locations of the pipe. As seen in Figure 3.11, the 1<sup>st</sup> strain gage was placed on the top of the pipe, the 2<sup>nd</sup> strain gage was placed on the left edge of the pipe, the 3<sup>rd</sup> strain gage was placed on the bottom of the pipe, and the 4<sup>th</sup> strain gage was placed on the right edge of the pipe.

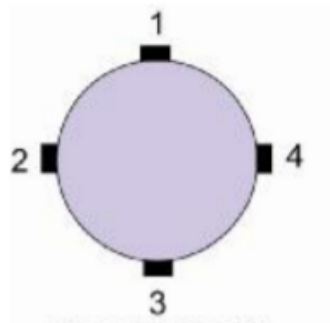


Figure 3.11. Locations of the strain gages.

### 3.1.6. Data Acquisition System

In the experiments, three different recordings were taken; load, displacement, and strain. To measure those variables, load cells, LVDTs, and strain gages were used, respectively. The working principle of all the data recorders depends on the change in the electrical resistance values. Data created from the change in the resistances was stored in a data acquisition system manufactured by National Instruments. The number of channels used was one for load measurement, two for displacement, and four for strain.

For the data acquisition from load cell, full-bridge configuration system was used. Cables from the load cell were linked to the NI-9949 module shown in Figure 3.12, and this module was attached by RJ-50 cable to NI-9237, which is a C-Series strain/bridge input module.

Data acquisition from LVDTs required an external voltage supply. 5V external voltage suppliers were used for each LVDT. Voltage suppliers were connected to LVDTs,

and LVDTs were connected to a NI-9472 module.

Strain gage data was obtained in a different way. There were two cables in a strain gage connected to NI-9944 module, in which a quarter-bridge configuration system was used. Afterwards, this module was again connected to NI-9237.

After the connection of the measuring devices to the NI-9237 and NI-9472 modules was completed, these modules were attached to the NI cDAQ-9179 chassis with a capacity to record data from 14 modules. The chassis was connected to the computer, and the data obtained from this system was analyzed and recorded by LabVIEW software. The NI cDAQ-9179 chassis and a NI-9237 module attached to it can be seen in Figure 3.13.



Figure 3.12. Load cell cables attached to a NI-9949 module.

### 3.1.7. LabVIEW Program

As the data obtained from this acquisition was in terms of resistance values, they were converted to the necessary units by LabVIEW software. To monitor the data obtained from the data acquisition system, a computer code in LabVIEW program was written. The code enabled the author to see all the strain gage, LVDT, and load cell values in the front panel. At the end of the test, the data was exported as an EXCEL file, and assessments were done from this output file.

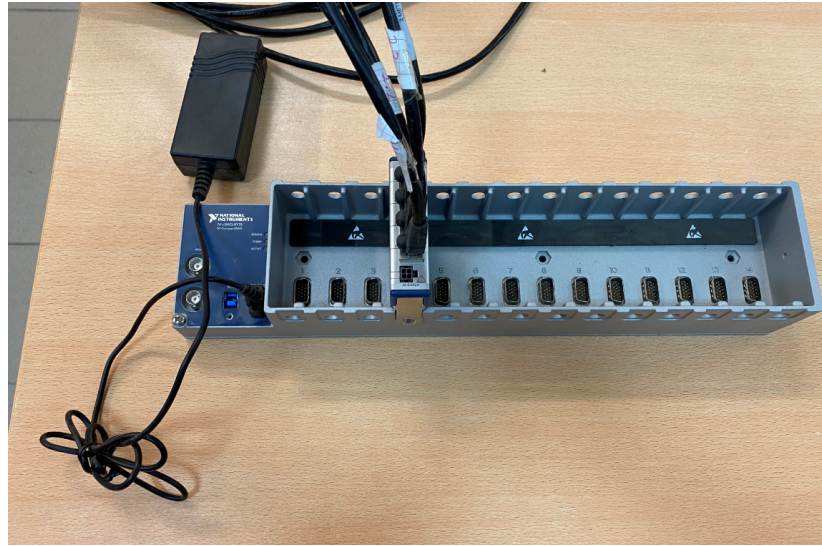


Figure 3.13. NI cDAQ-9179 chassis with a NI-9237 module.

## 3.2. Sand Properties

The sand used in the experiment was gathered from Çerkezköy, Thrace region and called as S1 Sand. Minerology of S1 Sand is a combination of quartz-sandstone and claystone and has a light grey-greenish color. Sand sample was sieved, and the particles retained between No 10 sieve and No 200 sieve was used. Afterwards, to get rid of any dust or organic material, sand sample was washed and dried in ovens in the laboratory. Several tests were done on the sand sample to find its index and strength properties.

### 3.2.1. Index Properties

3.2.1.1. Sieve Analysis. To find the grain size distribution of the sand sample, sieve analysis was done in accordance with the ASTM D422-63(2007)e2. From the data of the test, a percent finer graph was constituted as seen in Figure 3.14. With the use of Figure 3.14,  $D_{50}$ ,  $C_u$ , and  $C_c$  of the sand were determined.

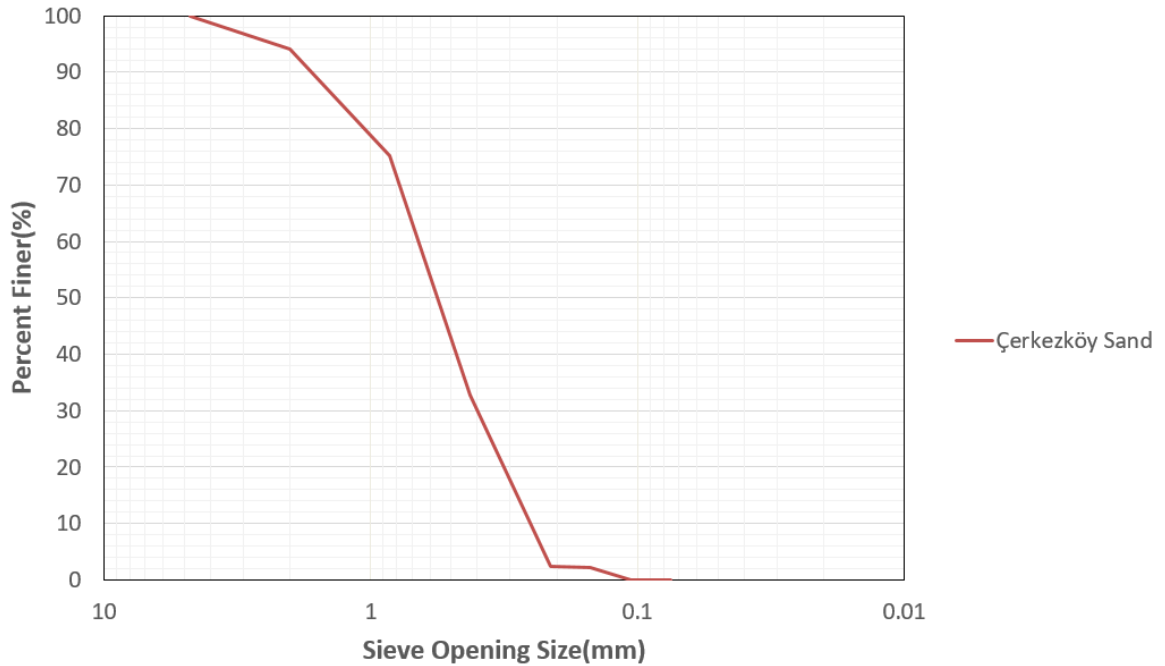


Figure 3.14. Percent finer vs Sieve opening size.

3.2.1.2. Specific Gravity Test. To find the specific gravity of the sand sample, specific gravity test was done in accordance with ASTM D854-14. Tests were repeated twice, and the average of the results was used. Specific gravity of the sand can be found in Table 3.3.

3.2.1.3. Minimum and Maximum Void Ratio Tests. Minimum and maximum void ratio tests were done for the determination of the relative density. Tests were done in accordance with ASTM D4253-16e1 and ASTM D4254-16, respectively. Minimum and maximum void ratio of the sand can be found in Table 3.3.

3.2.1.4. Partice Characteristics of the Tested Sands. Sphericity and roundness values of the tested sand were found by examining the sand particles using a Mshot brand MD50 model digital microscope camera. In total, 50 particles were analyzed. After taking each particle's high-resolution picture, it was analyzed by a Java based image processing program called ImageJ, which is able to assess the particle shape character-

istics of a given particle. From the analyses, average of the sphericity and roundness values were found and assigned as  $S_{ave}$  and  $R_{ave}$  values. Index properties of the tested sand were summarized in Table 3.3.

Table 3.3. Index properties.

Property	Value
Classification	SP
Median Particle Size( $D_{50}$ )	0.64
Coefficient of Uniformity( $C_u$ )	2.37
Coefficient of Curvature( $C_c$ )	0.93
Specific Gravity( $G_s$ )	2.62
Maximum Void Ratio( $e_{max}$ )	0.83
Minimum Void Ratio( $e_{min}$ )	0.50
Average Sphericity( $S_{ave}$ )	0.560
Average Roundness( $R_{ave}$ )	0.749

### 3.2.2. Strength Properties

3.2.2.1. Triaxial Tests. Triaxial testing is one of the most reliable tests in geotechnical engineering to find friction angle, and dilation angle. An automatic triaxial testing system manufactured by Geocomp was used in this study. Tests were conducted in four steps; initialization, saturation, consolidation, and shearing.

In initialization phase, sand specimen was wetted by applying a back pressure of 10kPa. This phase took about 20 minutes, or until whole sample was wetted.

In saturation phase, cell and pore pressures were increased step-by-step until reaching a pore pressure parameter of  $B=0.95$ , which is considered as fully saturated.  $B$  can be found using Equation 3.3:

$$B = \frac{\Delta u}{\Delta \sigma_3} \quad (3.3)$$

where,

- $\Delta u$  is the change in the specimen pore pressure that occurs when cell pressure changes and specimen drainage valves are closed.
- $\Delta\sigma_3$  is the change in cell pressure.

In consolidation phase, the desired mean effective stress was reached by increasing cell and pore pressures simultaneously. At that point, the drainage valve was opened, and soil sample was allowed to be consolidated.

In shearing phase, lateral pressure kept constant, and axial pressure kept increasing until reaching an axial strain value of 20%. In the scope of this thesis, isotropically consolidated drained axial compression tests were performed.

Tests were done in three different relative density ranges (loose( $I_D \approx 20$ ), medium dense( $I_D \approx 50$ ), and dense( $I_D \approx 75$ )) and three different surcharge pressures (50kPa, 200kPa, and 400kPa). In total seven tests were done with the results summarized in Table 3.4. To find the dilation angle, Equation 3.4 (Schanz and Vermeer, 1996) was used:

$$\Psi_p = \sin^{-1} \frac{\left(\frac{d\epsilon_v}{d\epsilon_1}\right)_p}{2 - \left(\frac{d\epsilon_v}{d\epsilon_1}\right)_p} \quad (3.4)$$

where,

- $\left(\frac{d\epsilon_v}{d\epsilon_1}\right)_p$  is the peak dilatancy rate.
- $\Psi_p$  is the peak dilation angle.
- $d\epsilon_v$  is the change in the volumetric strain.
- $d\epsilon_1$  is the change in the major principal strain.

After obtaining these peak friction angle and peak dilation angle values, critical state friction angle value was calculated. By definition, critical state friction angle is

Table 3.4. Triaxial test results.

Test Properties	Peak Friction Angle( $\Phi'_p$ )	Peak Dilation Angle( $\Psi_p$ )
$I_D=20\%$ $\sigma'_3=50\text{kPa}$	35.2°	3.2°
$I_D=54\%$ $\sigma'_3=50\text{kPa}$	37.1°	8.8°
$I_D=54\%$ $\sigma'_3=200\text{kPa}$	36.5°	5.7°
$I_D=54\%$ $\sigma'_3=400\text{kPa}$	34.4°	3.0°
$I_D=79\%$ $\sigma'_3=50\text{kPa}$	40.6°	11.9°
$I_D=74\%$ $\sigma'_3=200\text{kPa}$	39.2°	10.4°
$I_D=71\%$ $\sigma'_3=400\text{kPa}$	36.3°	4.6°

equal to the friction angle where dilation angle is zero. To find critical state friction angle, a scatter graph was drawn, and the best-fit line was plotted with its equation. Using this equation, critical state friction angle was found as shown in Figure 3.15.

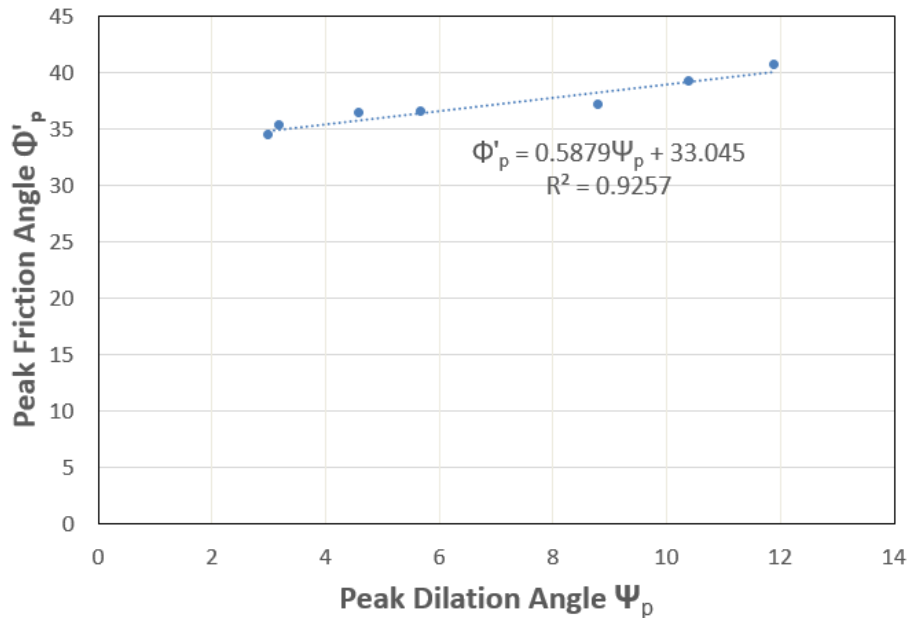


Figure 3.15. Peak friction angle vs Peak dilation angle.

In the physical model experiments, the axisymmetric conditions in the triaxial testing were not valid due to the prevention of the movement in the y-direction. In this case, rather than axisymmetric conditions, plain-strain conditions prevailed. Hence, the

engineering properties of the soil backfill were converted to plain-strain conditions by using the method proposed by Nanda and Patra (2015). There are three equations in this method (Equation 3.5, Equation 3.6, and Equation 3.7), as shown below:

$$K_{\Phi T} = \frac{\Phi_c^T}{\Phi_p^T} \quad (3.5)$$

$$K_{\Phi P} = 0.19e^{\left(\left(\frac{A_P^P}{A_P^T}\right)_B K_{\Phi T}\right)} \quad (3.6)$$

$$\Phi_p^P = \Phi_p^T \left( \frac{\left(\frac{A_P}{A_T}\right) (1 - K_{\Phi T})}{(1 - K_{\Phi P})} \right) \quad (3.7)$$

where,

- $\Phi_c^T$  is the critical state friction angle found by triaxial testing.
- $\Phi_p^T$  is the peak friction angle found by triaxial testing.
- $\Phi_p^P$  is the peak friction angle for plain-strain conditions.

In Equation 3.6, the term  $\left(\frac{A_P^P}{A_P^T}\right)_B$  was considered to be equal to 1.667. Nanda and Patra (2015) stated that the ratio  $\frac{A_P}{A_T}$  alters with the different relative density and confining pressure ranges. In this work, when  $K_{\Phi T}$  was smaller than 0.8,  $\frac{A_P}{A_T}$  was taken as 1.5, while if  $K_{\Phi T}$  was higher than 0.9,  $\frac{A_P}{A_T}$  was taken as 1.6. For the values of  $K_{\Phi T}$  between 0.8 and 0.9,  $\frac{A_P}{A_T}$  was taken as 1.55. An example for this transformation from triaxial conditions to plain-strain condition is shown in Table 3.5.

After creating Table 3.5, the critical state friction angle for plain-strain conditions of the tested sand was found by taking the average. In Table 3.5,  $r_{ps}$  was calculated

Table 3.5. Conversion to plain-strain condition.

$\Phi_p^T$	$\Phi_c^T$	$K_{\Phi T}$	$K_{\Phi P}$	$\frac{A_P}{A_T}$	$\Phi_p^P$	$\Phi_c^P$	$\Psi_p$	$r_{ps}$
34.4°	33.04°	0.96	0.94	1.60	37.6°	35.4°	3.0°	0.72
39.2°	33.04°	0.84	0.77	1.55	42.3°	32.8°	10.4°	0.92
35.2°	33.04°	0.94	0.91	1.60	37.7°	34.3°	3.2°	1.08
36.5°	33.04°	0.91	0.86	1.60	39.3°	33.8°	5.7°	0.97
37.1°	33.04°	0.89	0.84	1.55	39.0°	32.7°	8.8°	0.71
40.6°	33.04°	0.81	0.74	1.55	44.7°	33.0°	11.9°	0.98
36.3°	33.04°	0.91	0.87	1.60	39.0°	33.8°	4.6°	1.13

using the Equation 3.8:

$$r_{ps} = \frac{\Phi_p^P - \Phi_c^P}{\Psi_p'} \quad (3.8)$$

There are again several  $r_{ps}$  values; therefore, the average of them was taken as the desired slope for plain-strain conditions.

Determining the peak dilation angle and, therefore, the peak friction angle for the test conditions is a difficult task in the physical model experiments. First, peak dilation angle for the test conditions should be calculated, and then by multiplying it with  $r_{ps}$  and adding critical state friction angle for plain-strain conditions, peak friction angle can be obtained. To calculate peak dilation angle, the method proposed by Cinicioglu and Abadkon (2015) was applied, as given in Equation 3.9:

$$\tan \Psi_p = \alpha_\psi \left( \frac{p_i'}{p_a} \right) + m_\psi I_D \quad (3.9)$$

where,

- $p_i'$  is the mean effective stress.
- $p_a$  is the atmospheric pressure.

- $I_D$  is the relative density.
- $a_\psi$  and  $m_\psi$  are material constants.

In Equation 3.9, to find  $a_\psi$  and  $m_\psi$ , a nonlinear regression analysis was done in SPSS IBM software. Found values were then used to calculate peak dilation angle, and comparison was done between actual peak dilation angle and calculated peak dilation angle. This comparison is depicted in Figure 3.16 in which it is clear that the proposed method by Cinicioglu and Abadkon (2015) is safe to use to compute peak dilation angle.

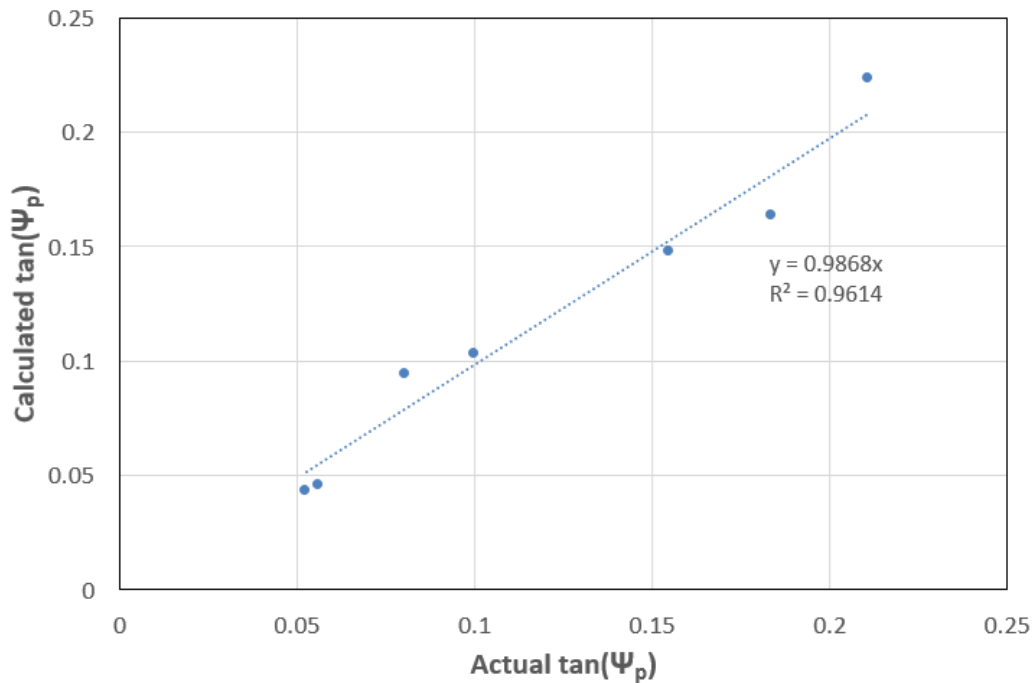


Figure 3.16. Calculated peak dilation angle vs Actual peak dilation angle.

Also, stiffness value for the test condition was determined by using the data of the triaxial test results. By definition,  $E_{50}$  is the secant stiffness for the region between  $q_{dev} = 0$  and  $q_{dev} = (q_{dev,max})/2$ , where  $q_{dev}$  is the difference between effective major principle stress and effective minor principle stress. From the triaxial test data,  $q_{dev}$  vs  $\epsilon_a$  graph was created, where  $\epsilon_a$  is the axial strain. An example of this is illustrated in Figure 3.17. In the physical model experiments, relative density was 35%. Therefore,

triaxial tests that suit most to those conditions were selected. The average of those tests was taken as the  $E_{50}$  value of the model experiments. Stiffness values of the selected triaxial tests can be found in Table 3.6.

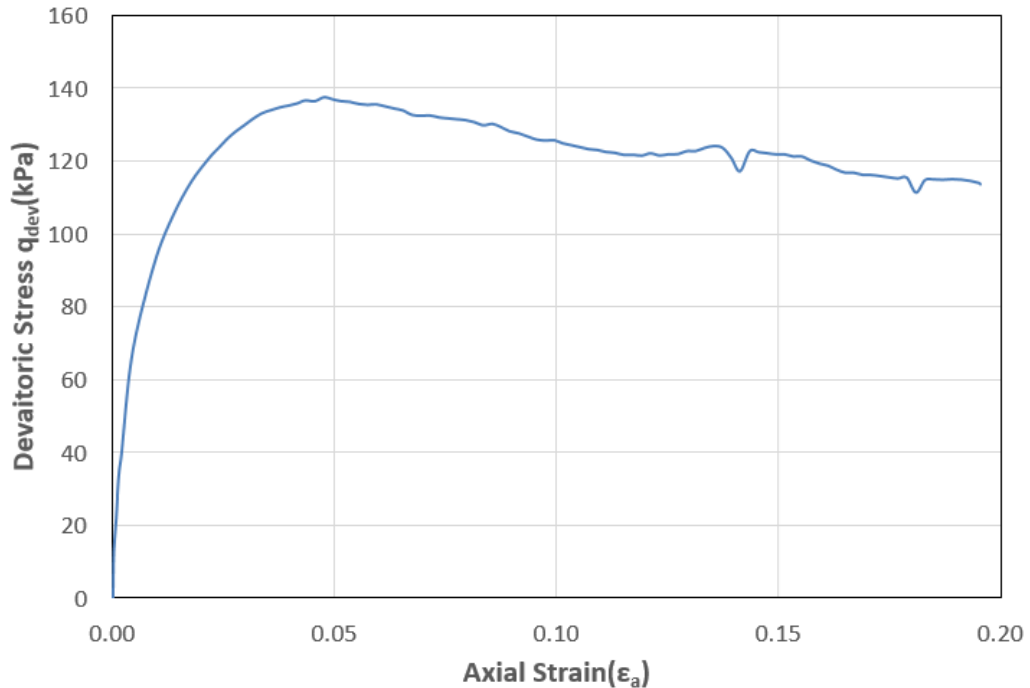


Figure 3.17.  $q_{dev}$  vs  $\epsilon_a$  for  $I_D=20\%$   $\sigma'_3=50\text{kPa}$  test.

Table 3.6. Triaxial tests used to find  $E_{50}$ .

Test Properties	$E_{50}$ (MPa)
$I_D=20\%$ $\sigma'_3=50\text{kPa}$	13.2
$I_D=54\%$ $\sigma'_3=50\text{kPa}$	19.5
<b>Average</b>	16.3

Strength properties of the tested sand are summarized in Table 3.7.

### 3.3. PIV Analysis

Working principle and the procedure of the PIV analysis was given in the Literature Review section. Here, the parameters and some of the investigation methods

Table 3.7. Strength properties of the sand.

	<b>Value</b>
$\Phi_c^T$	33.04
$\Phi_c^P$	33.68
$r_{tx}$	0.59
$r_{ps}$	0.93
$a_\psi$	-0.03
$m_\psi$	0.302

used in this work will be explained.

The patch size used in the PIV analysis was selected as 64x32(pixels). This enabled a clear understanding of the displacement mechanism, while avoiding high computation time.

The main difference in this PIV analysis was the selection of the area of interest(AOI). In the AOI, the area that the pipe was located was excluded. This was done for two reasons; first, in this way the vector fields near the pipe was observed more clearly, and second, the difference in the patches located inside the pipe cannot be recognized by the analysis, as inside of the pipe was dark. Effect of this exclusion on vector and displacement field can be seen in Figure 3.18 and Figure 3.19, respectively. In Results & Discussion section, it will be seen that PIV analyses were interpreted in two ways; by determining the boundaries of the failure zone and the maximum vertical distance between this zone and the foundation. Before conducting a PIV analysis, it was validated that these variables were not affected from the exclusion of the pipe region from the AOI.

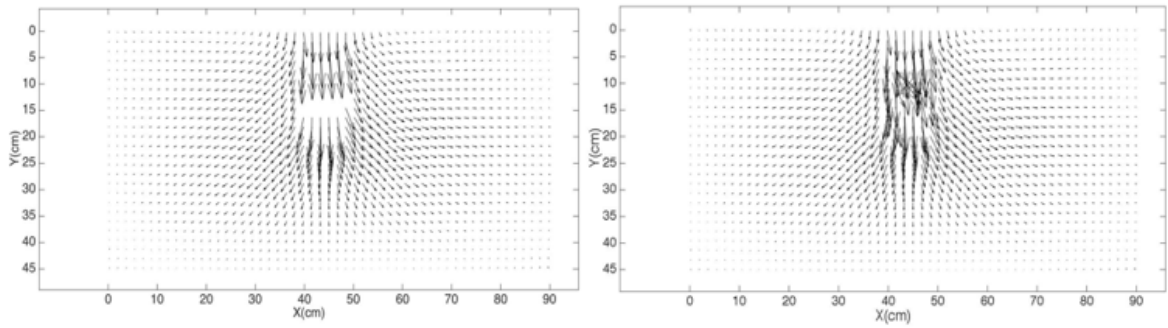


Figure 3.18. Comparison of the vector fields in UR4 test (pipe area excluded(left), pipe area included(right)).

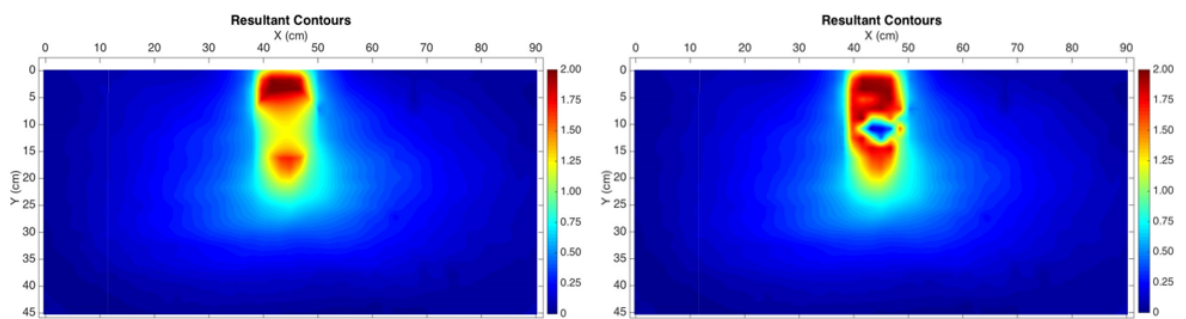


Figure 3.19. Comparison of the displacement fields in UR4 test (pipe area excluded(left), pipe area included(right)).

### 3.4. Pipe Properties

In the scope of this thesis, the influence of a single buried pipe with respect to the foundation on the pressures experienced by was investigated; therefore, the selection of the test pipe is critical. For instance, in order to make strain gages work properly, they should be stuck to a material that obeys the Hooke's Law. Pipes used in the experiments were supplied from a firm called Pilsa, and it was confirmed that the pipes obey Hooke's Law. Properties of the pipe are listed in Table 3.8, and a picture of the pipe is illustrated in Figure 3.20.



Figure 3.20. Model pipe used in the experiments.

Table 3.8. Pipe properties.

Property	Units	Value
Pipe Diameter	cm	7.5
Pipe Wall Thickness	mm	2.2
Modulus of Elasticity	MPa	3000
Thermal Expansion Coefficient	$^{\circ}K^{-1}$	$0.7 \times 10^{-4}$
Specific Heat	J/g $^{\circ}K$	1.0

### 3.5. Procedure of the Experiments

The procedure followed in the experiments is explained step-by-step below.

- Burial depth was determined, and sand was pluviated to that depth while con-

trolling the desired relative density range.

- Surface of the pipe was cleaned.
- The points to stick the strain gages were determined.
- Strain gages were stuck perpendicular to the pipe using the special glue.
- To protect strain gages, they were covered by SB-type band.
- Pipe was placed in the pre-determined location in the test box.
- Water gage was used to make the pipe exactly horizontal, and some changes were done if necessary.
- The rest of the sand was poured until reaching the end point.
- Spring-system was pushed inside the footing and locked using the screws.
- Model footing was placed in the box, and its horizontal position was checked by the water gage.
- Steel marbles were placed in the grooves on the surface of the model footing.
- Screws in the spring-system were unlocked to permit the rubber inside the system to press on the plexiglas surface.
- The other ends of the strain gages were connected to the NI-9944 module.
- Camera was placed on the top of the tripod, and tripod was placed in the pre-determined location to capture the front surface precisely. Test setup prior to the start of the test is shown in Figure 3.21.
- Lights of the laboratory were turned off, and two spotlights, enlightening only the test box, were turned on.
- Hexagonal steel plate that distributed the load was lowered slowly, and at the instance that it touched the marbles, lowering was stopped.
- Test started with the speed of 5mm/min and lasted four minutes when a displacement of 20mm was reached.
- In total, 11 photos were obtained for each test, which were taken with 2mm intervals.
- After the end of the test, the data obtained was saved in an EXCEL file, and the photos were analyzed in geoPIV and geoPIV\_RG modules in MATLAB.

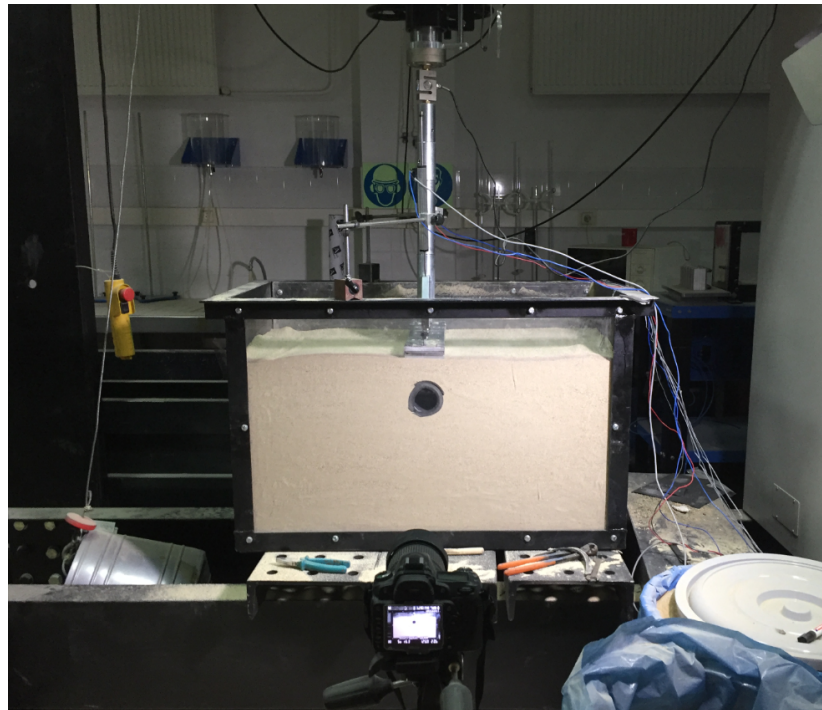


Figure 3.21. Test setup prior to the start of the test.

## 4. RESULTS

In this section, results of the experiments will be explained. In total, 10 tests were conducted with varying pipe positions in terms of horizontal and vertical distances from the model footing. The testing program, the schematic illustration of the investigated parameters, and pipe location in each test can be seen in Table 4.1, Figure 4.1, and Figure 4.2 respectively. Also, a line was drawn to connect the center of the pipe with the center of the foundation, and called as connection line. The angle between this angle and the horizontal was found, shown in Figure 4.3 and Table 4.2, and used in the analyses.

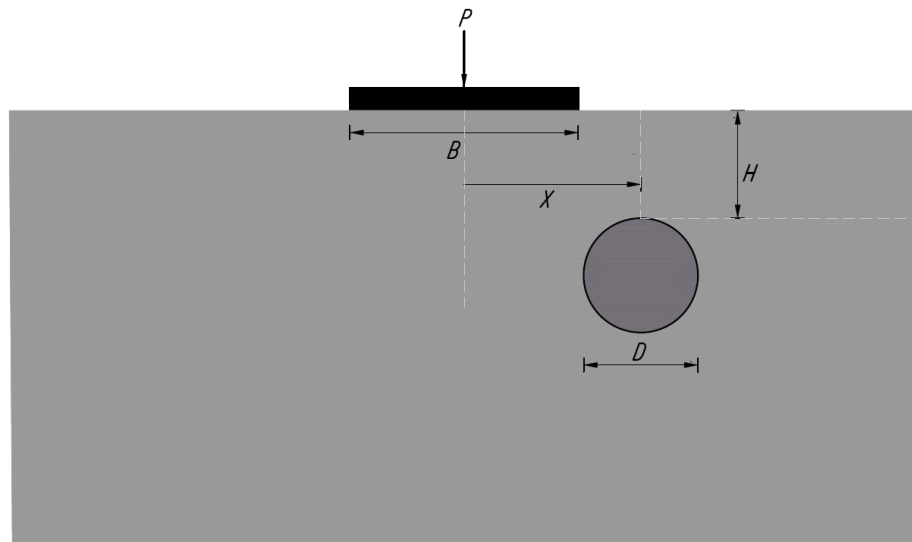


Figure 4.1. Investigated parameters.

Reference experiment in Table 4.1 is the experiment that was conducted without a pipe. Backfill relative density was 35% in all the experiments. Results will be given in two parts; analyses of the photos and analyses of the pressure acting on the pipe.

Table 4.1. Testing program.

Experiment No	Sand Type	H/D	X/D
Reference	Çerkezköy Sand	-	-
UR1	Çerkezköy Sand	0.5	0
UR2	Çerkezköy Sand	0.5	1.17
UR3	Çerkezköy Sand	0.5	1.67
UR4	Çerkezköy Sand	1	0
UR5	Çerkezköy Sand	1	1.17
UR6	Çerkezköy Sand	1	1.67
UR7	Çerkezköy Sand	3	0
UR8	Çerkezköy Sand	3	1.17
UR9	Çerkezköy Sand	3	1.67

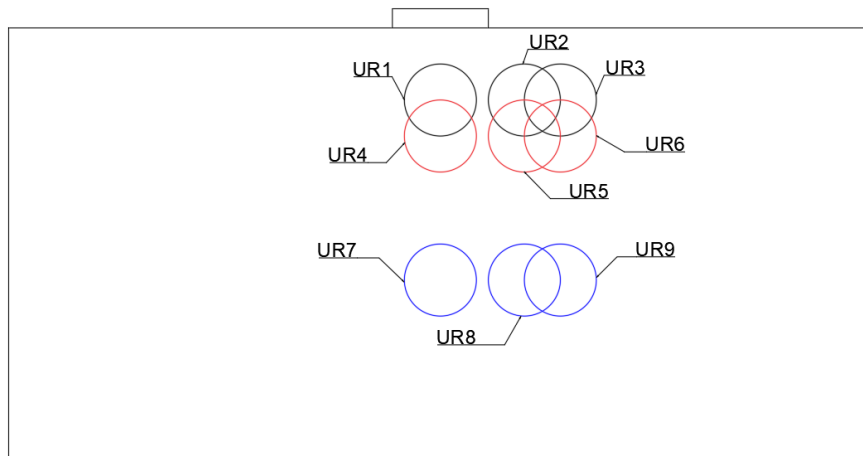


Figure 4.2. Location of the pipe for each test.

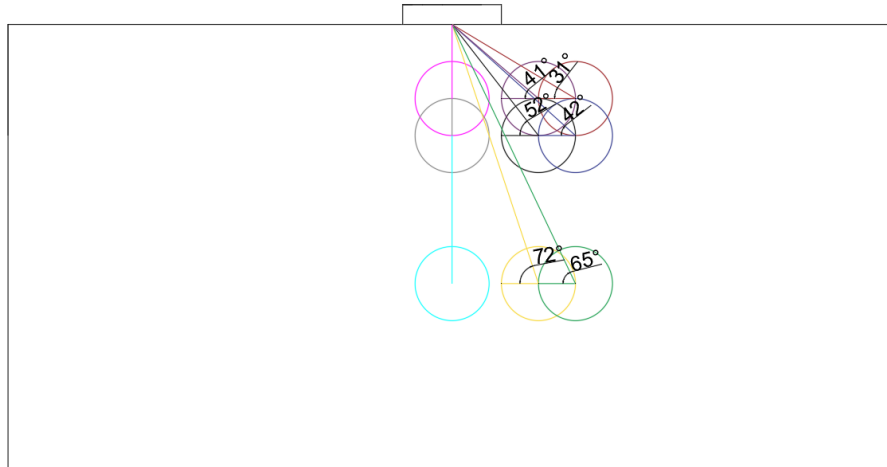


Figure 4.3. Illustration of the angles between connection lines and the horizontal.

Table 4.2. The angle of the connection line with the horizontal.

Experiment No	Angle
<b>UR2</b>	41°
<b>UR3</b>	31°
<b>UR5</b>	52°
<b>UR6</b>	42°
<b>UR8</b>	72°
<b>UR9</b>	65°

## 4.1. Analyses of the Photos

### 4.1.1. Effect of Pipe Location on the Affected Area

In Figures 4.4-4.13, photographs of all experiments, and the corresponding results of the PIV analyses as displacement fields, and as vector fields are illustrated, respectively.

After obtaining PIV results as displacement and vector fields, extent of the affected zone for each experiment was determined. In the displacement fields, regions exposed to the same deformation level were marked with the same color. To determine the differences in these zones, areas having the same deformations were compared. To quantify the areal extent of this affected zone, AutoCAD program was used in which the affected zone was drawn carefully with the black lines (corresponds to a 0.25mm displacement), as seen in Figure 4.14. Besides, the maximum vertical distance between the foundation and the affected zone (i.e, vertical extent) was measured. Afterwards, areal extent of the affected zone was divided to the total area of interest to have normalized values to make the comparisons easier, and this ratio was denoted with  $\zeta$  also shown in Equation 4.1.

$$\zeta = \frac{\text{Areal extent of the affected zone}}{\text{Total area of interest}} \quad (4.1)$$

Obtained results are presented in Table 4.3 and Table 4.4, and illustrated in Figure 4.15 and Figure 4.16.

Based on Table 4.3 and Table 4.4, it can be stated that with the pipe installment, the failure surface widens. In general, both areal and vertical extent of the affected zone tend to decrease when pipe translates horizontally from the vertical centerline of the foundation. Also, both areal and vertical extent of the affected zone when pipe was placed at  $H/D=1$  and  $H/D=3$  were somewhat close, but there was a significant increase when compared to  $H/D=0.5$ . In Figure 4.15, it was observed that for  $H/D=0.5$  and

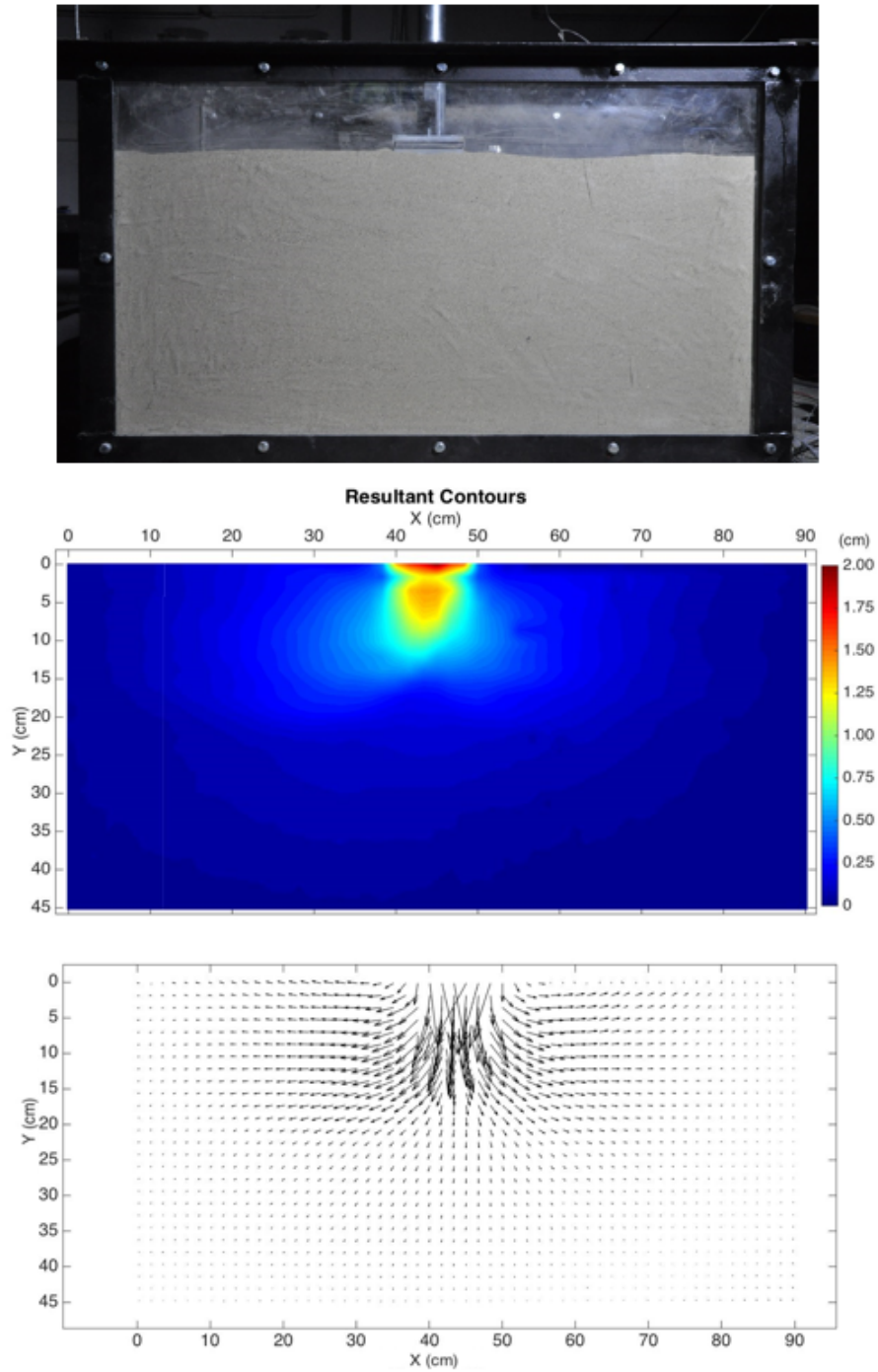


Figure 4.4. Photograph, displacement field, and vector field of the reference test.

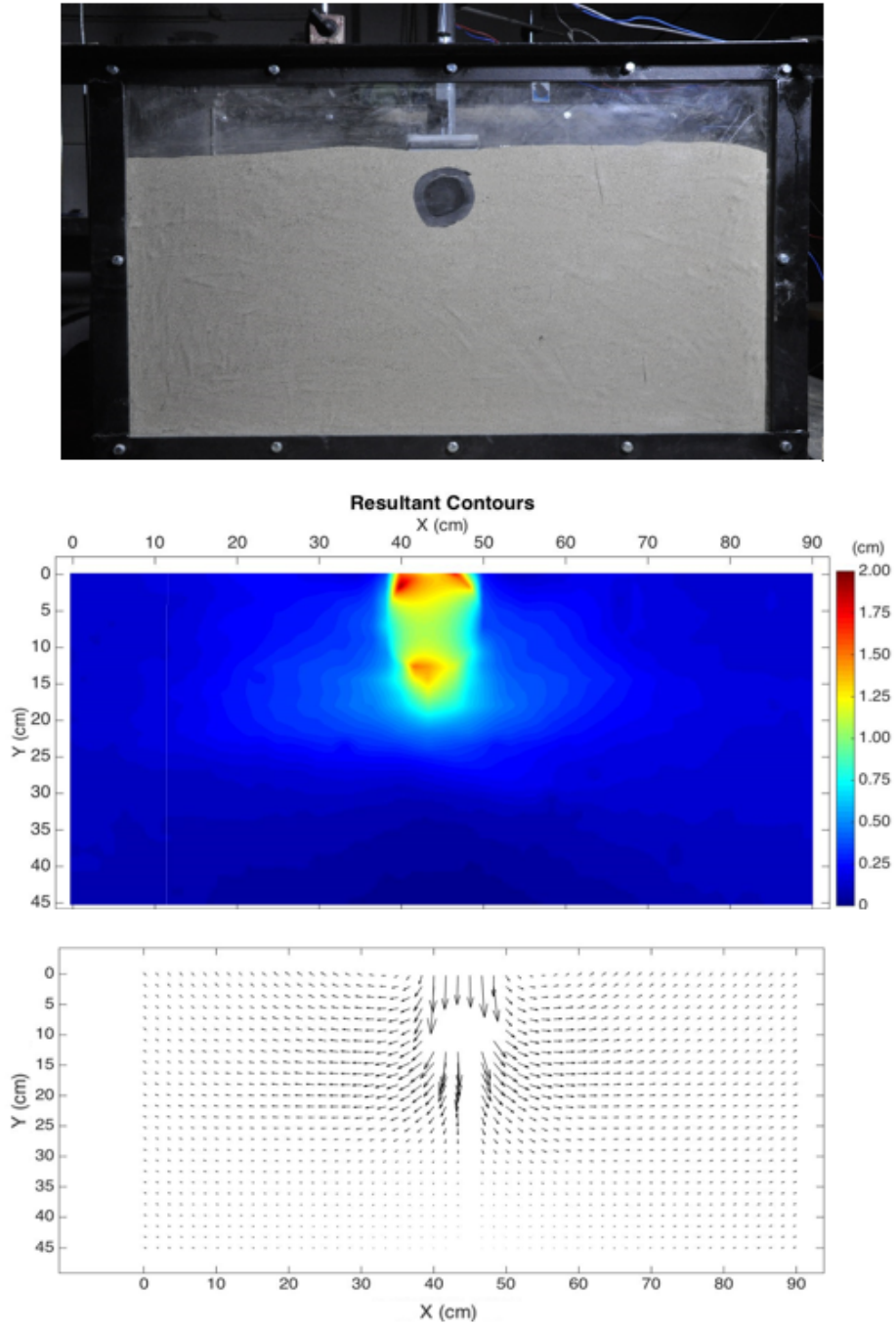


Figure 4.5. Photograph, displacement field, and vector field of the UR1 test.

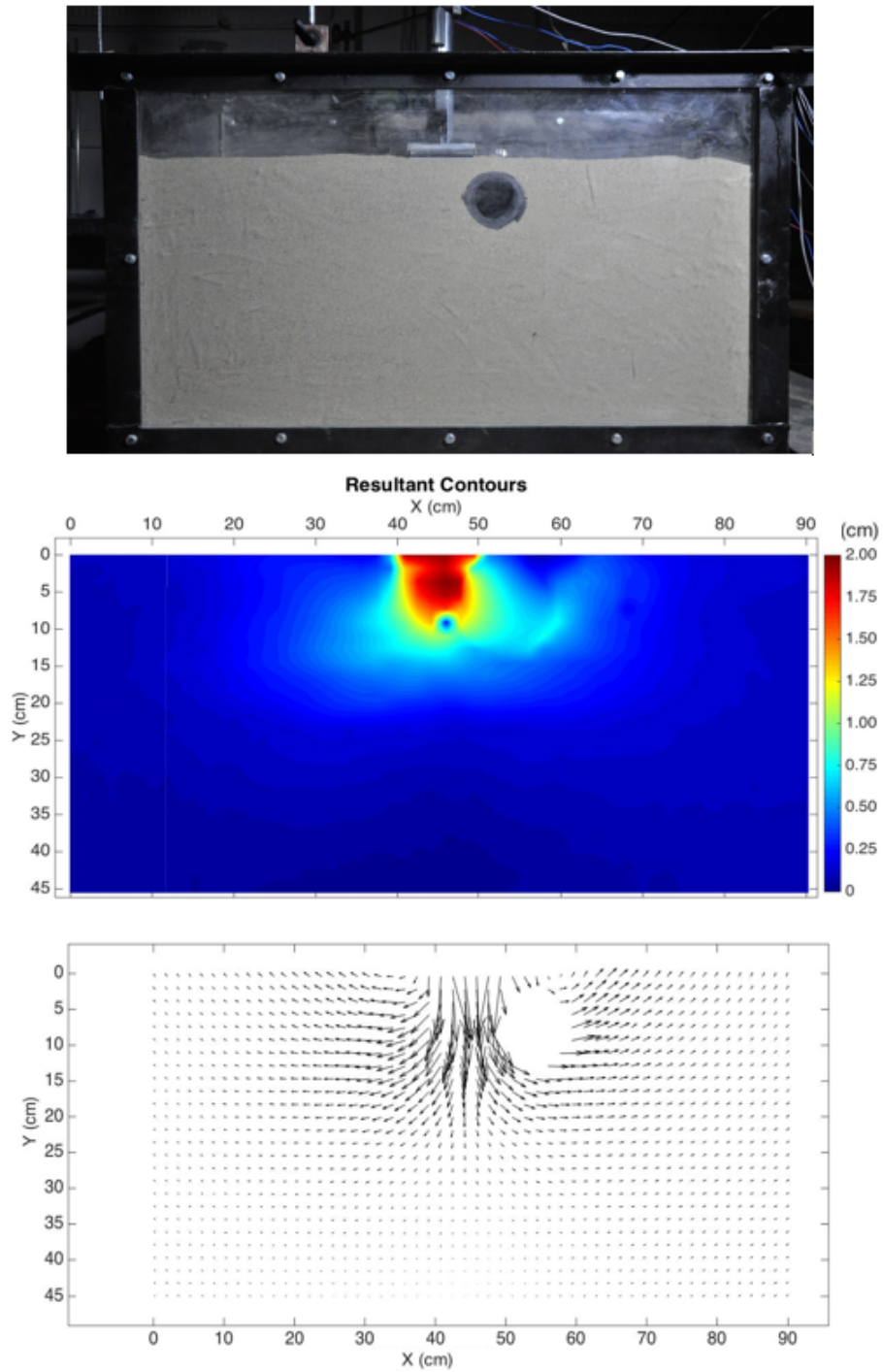


Figure 4.6. Photograph, displacement field, and vector field of the UR2 test.

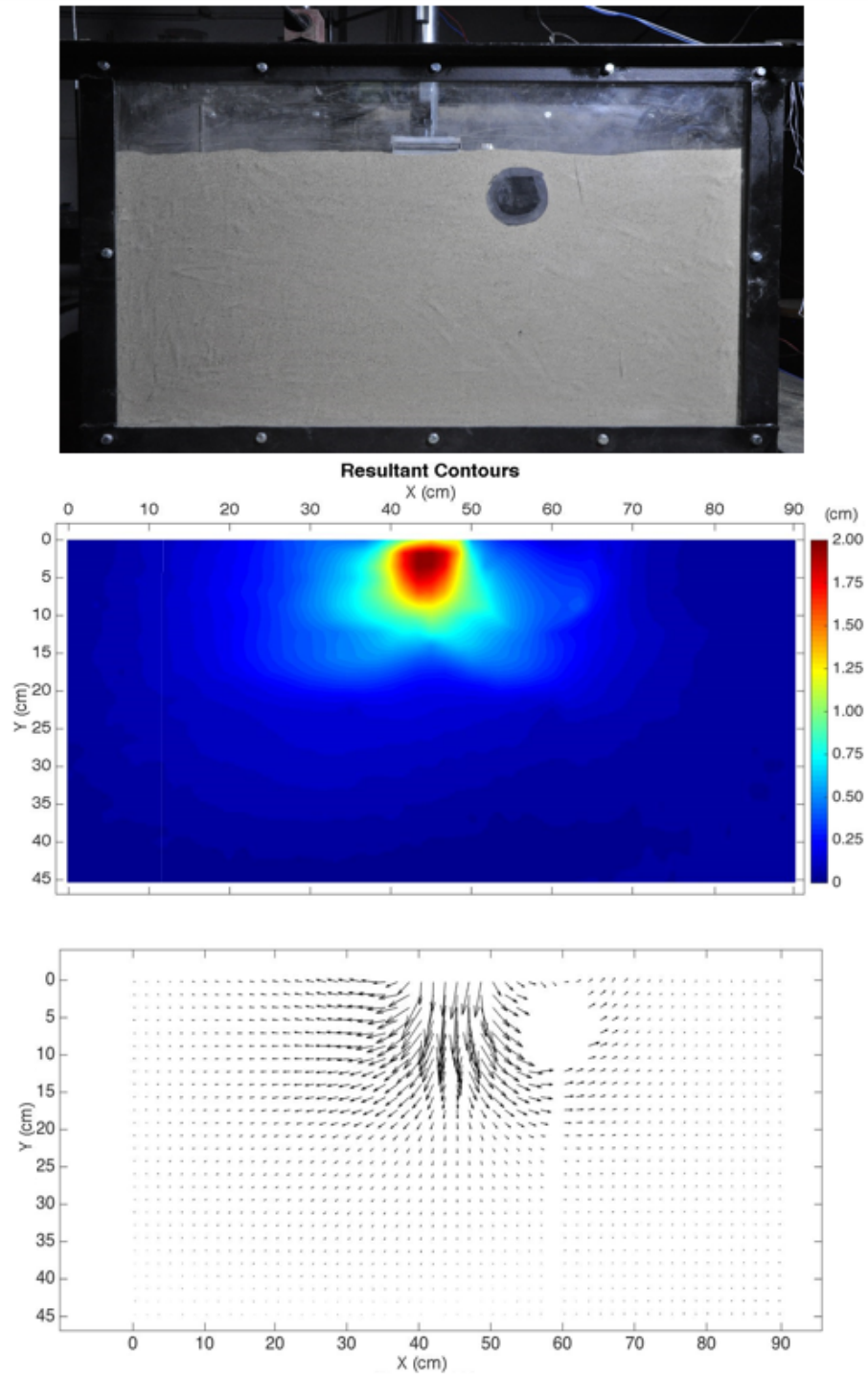


Figure 4.7. Photograph, displacement field, and vector field of the UR3 test.

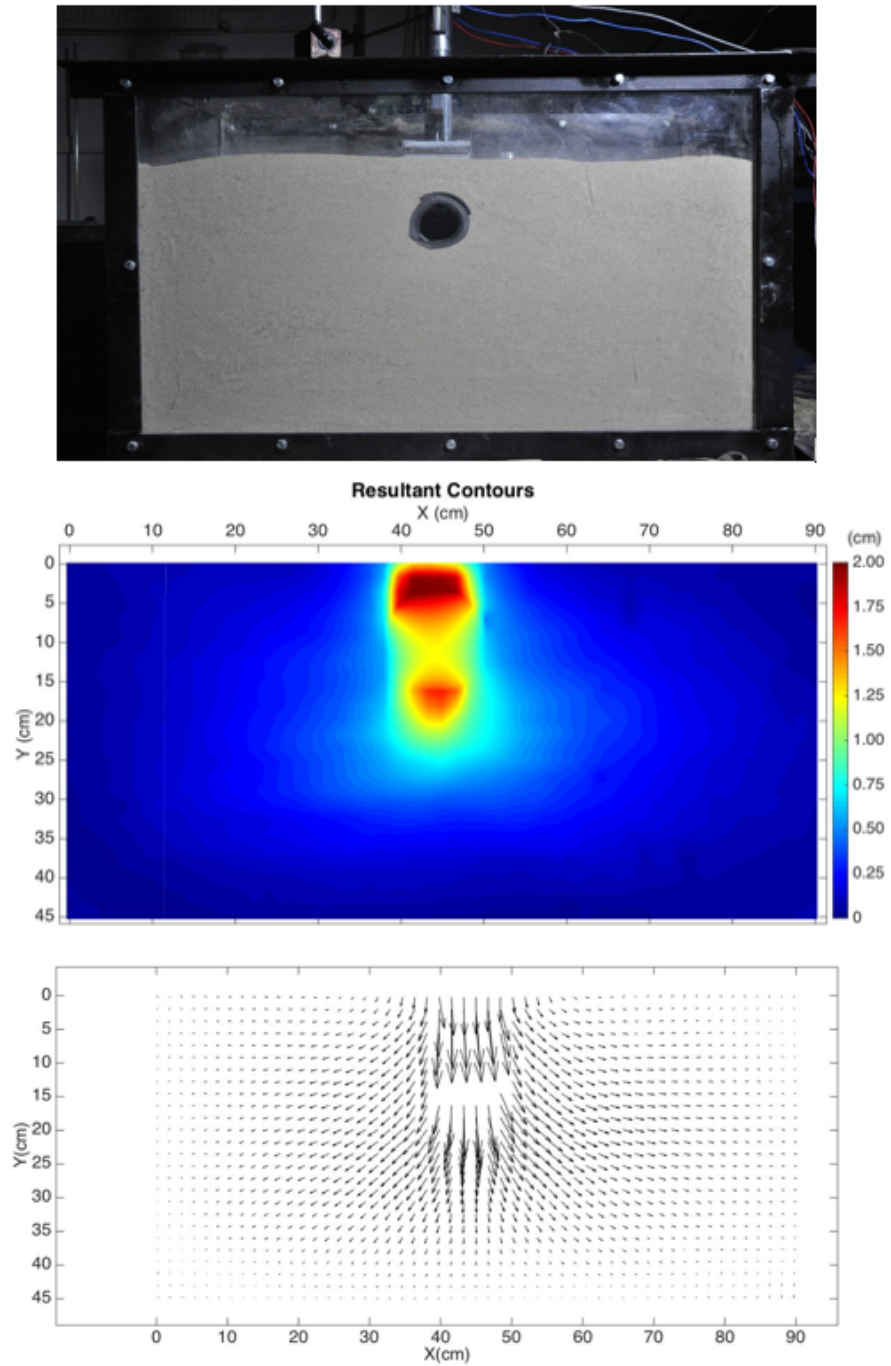


Figure 4.8. Photograph, displacement field, and vector field of the UR4 test.

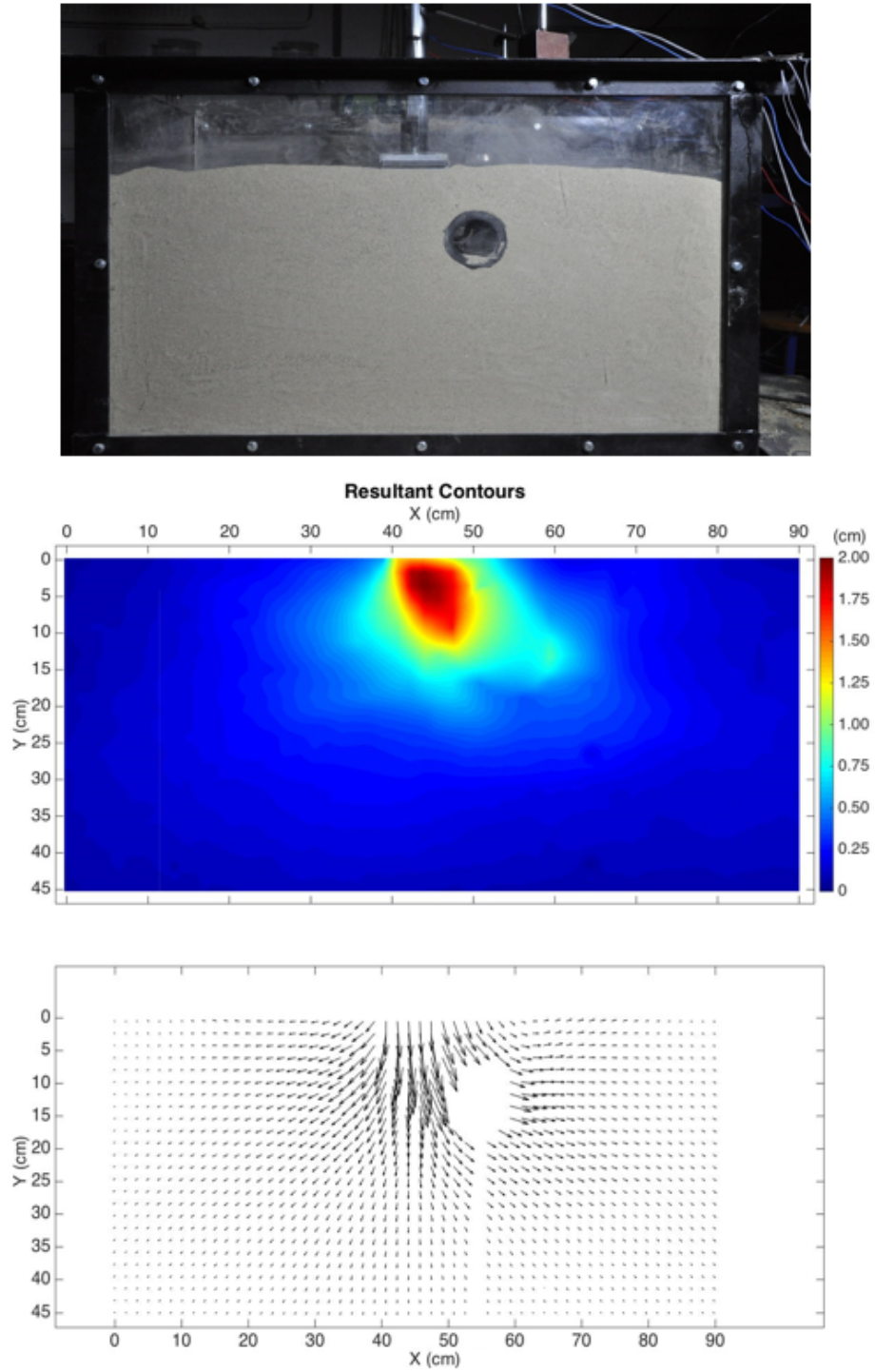


Figure 4.9. Photograph, displacement field, and vector field of the UR5 test.

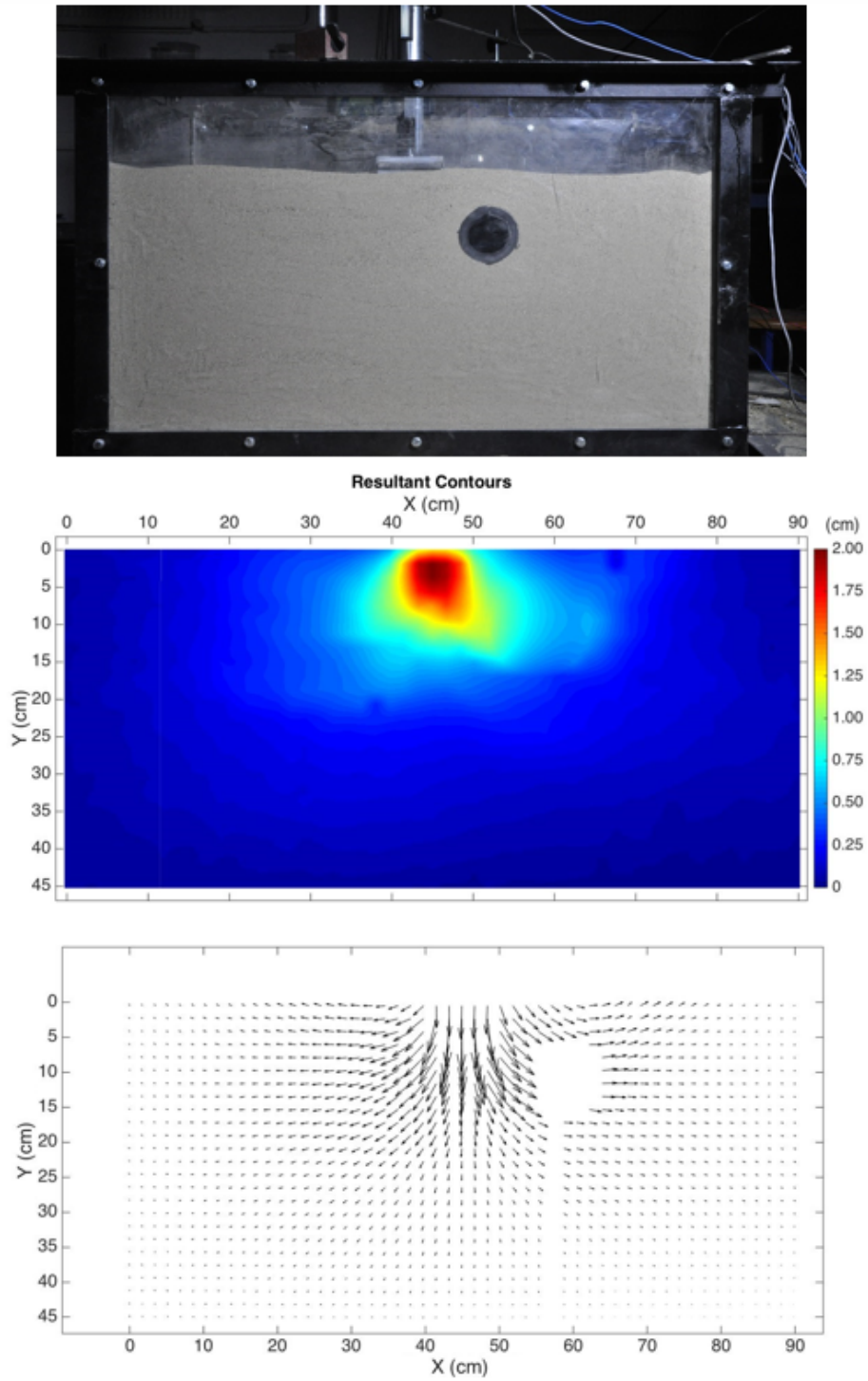


Figure 4.10. Photograph, displacement field, and vector field of the UR6 test.

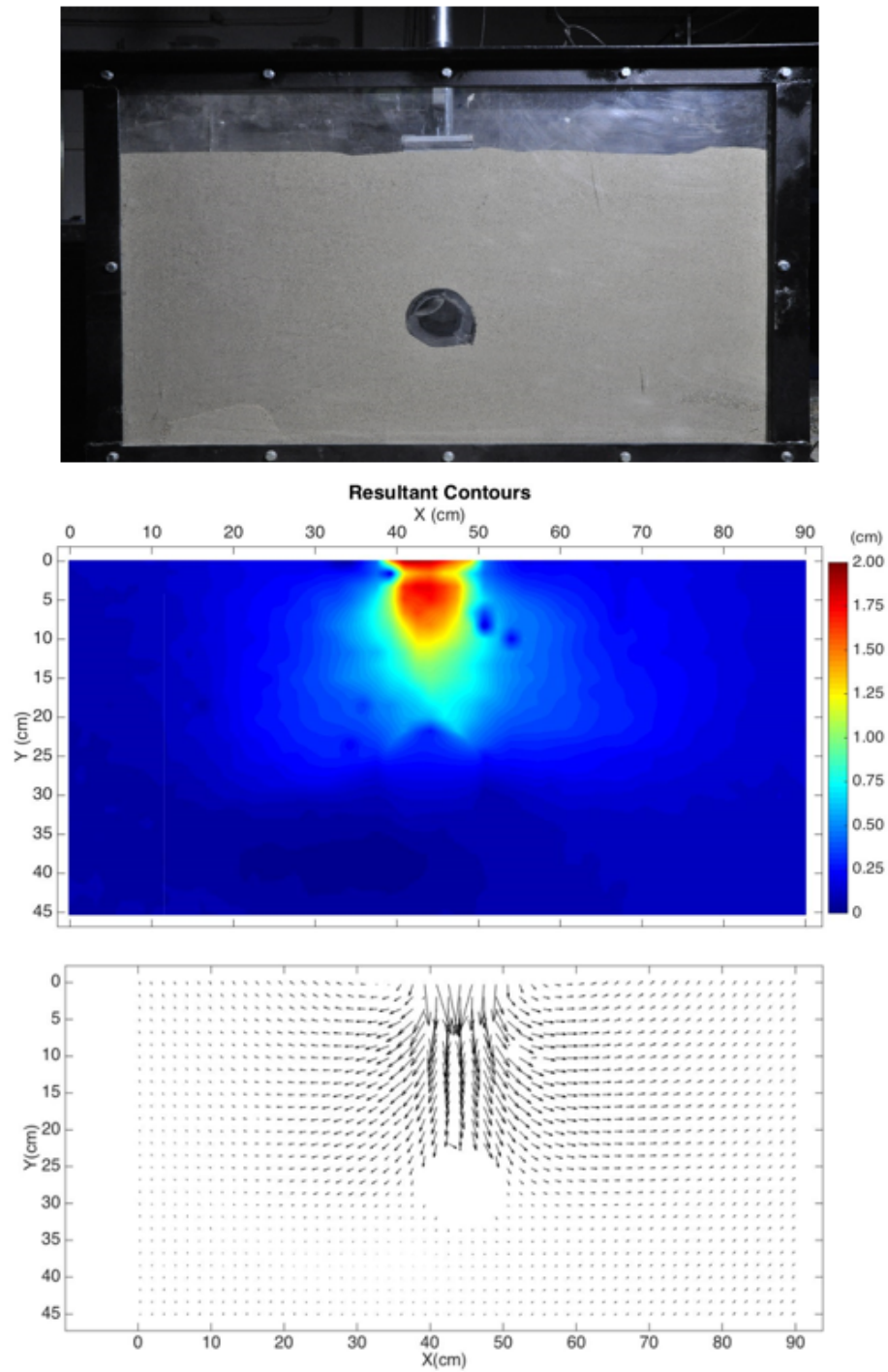


Figure 4.11. Photograph, displacement field, and vector field of the UR7 test.

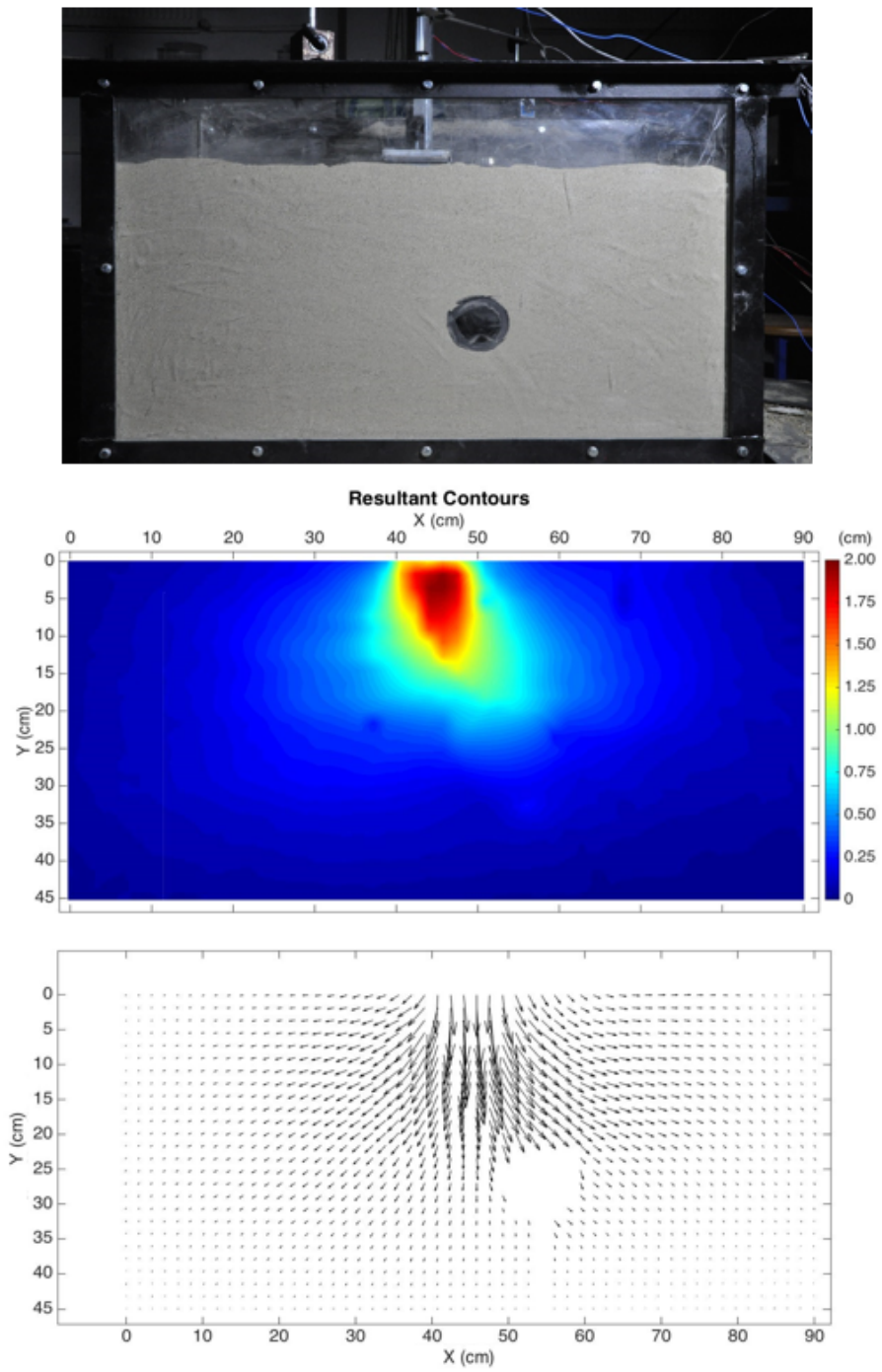


Figure 4.12. Photograph, displacement field, and vector field of the UR8 test.

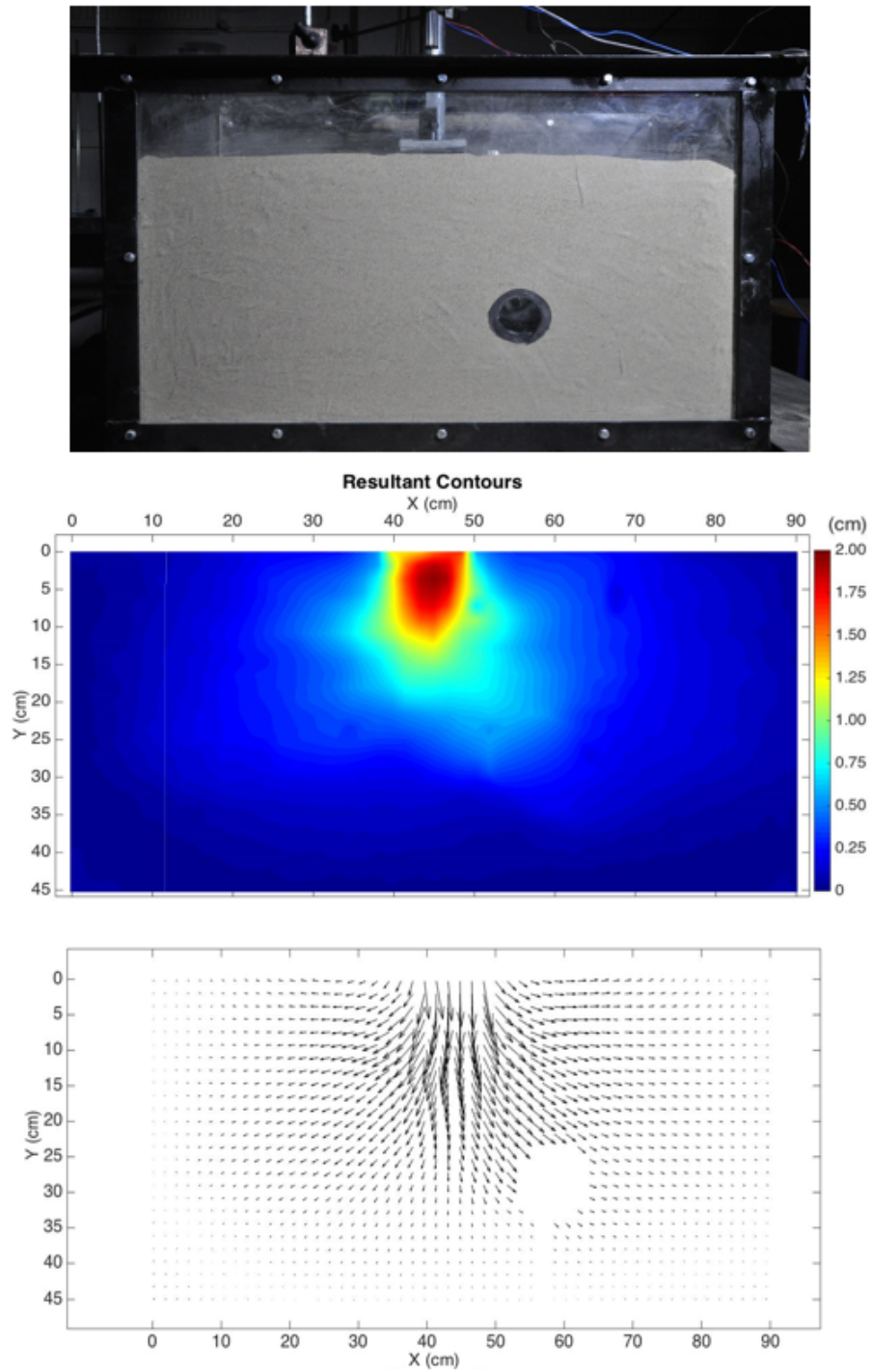


Figure 4.13. Photograph, displacement field, and vector field of the UR9 test.

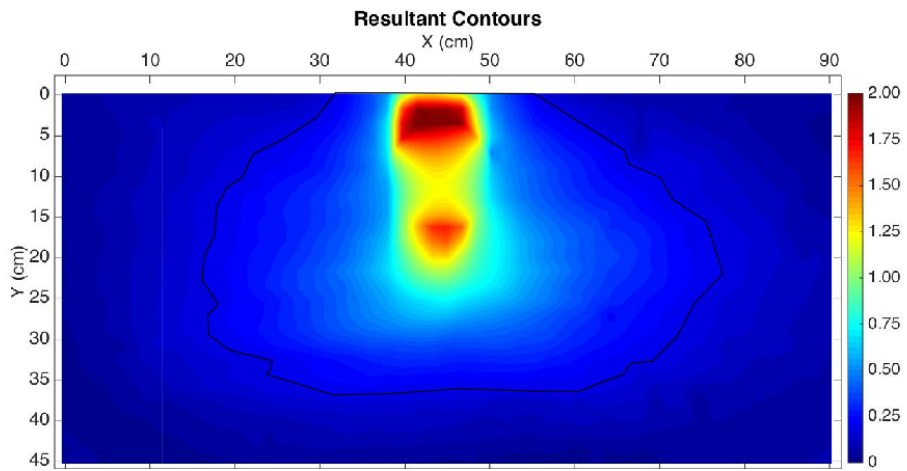


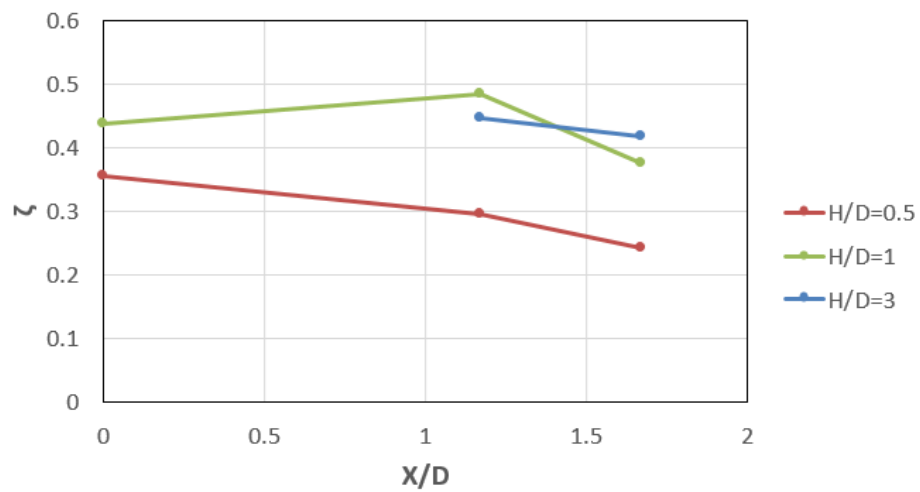
Figure 4.14. Determination of the affected zone.

Table 4.3. Comparison of the areal extent of the affected zones.

Experiment No	$\zeta$
Reference Test	0.21
UR1	0.35
UR2	0.29
UR3	0.24
UR4	0.44
UR5	0.48
UR6	0.37
UR8	0.45
UR9	0.42

Table 4.4. Comparison of the vertical extent of affected zones.

Experiment No	Vertical Extent(cm)
Reference Test	21.18
UR1	29.23
UR2	22.87
UR3	21.62
UR4	36.82
UR5	36.44
UR6	30.78
UR8	34.56
UR9	34.41

Figure 4.15. Change in  $\zeta$  for different pipe locations.

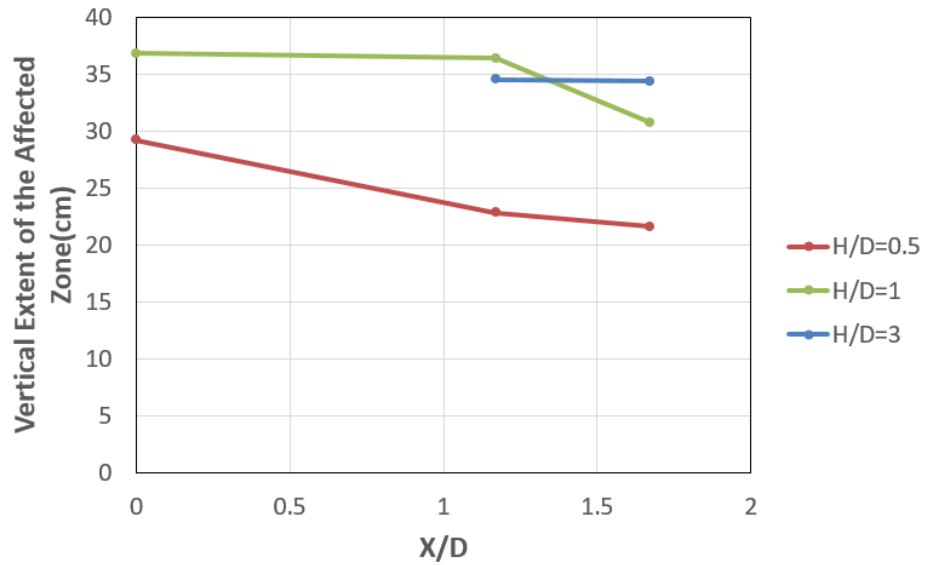


Figure 4.16. Change in the vertical extent of the affected zone different pipe locations.

H/D=1 tests, change in  $\zeta$  between X/D=0 and X/D=1.17 was less significant than the change between X/D=1.17 and X/D=1.67. Theoretically, when X/D ratio becomes infinity,  $\zeta$  should be equal to the reference test. The exact X/D location where the  $\zeta$  becomes equal to the reference test is lacking, and can be examined in the future research. Unfortunately, due to sand intrusion between pipe and plexiglas surface, data could not be acquired for UR7 test properly.

Besides, vector fields shown in Figure 4.4- Figure 4.13 were examined to find the most affected part of the pipe from the sand displacements. This analysis, shown in Table 4.5, was used in the comparison of the pipe pressures.

In Table 4.5, the most affected region in UR9 is seen as equal, meaning that 1<sup>st</sup> strain gage and 2<sup>nd</sup> strain gage were affected from soil displacement approximately equally.

Table 4.5. Most affected region of the pipe from displacement.

<b>Experiment No</b>	<b>Most Affected Part of the Pipe</b>
<b>UR1</b>	Crown/1 <sup>st</sup> Strain Gage
<b>UR2</b>	Left/2 <sup>nd</sup> Strain Gage
<b>UR3</b>	Left/2 <sup>nd</sup> Strain Gage
<b>UR4</b>	Crown/1 <sup>st</sup> Strain Gage
<b>UR5</b>	Left/2 <sup>nd</sup> Strain Gage
<b>UR6</b>	Left/2 <sup>nd</sup> Strain Gage
<b>UR7</b>	Crown/1 <sup>st</sup> Strain Gage
<b>UR8</b>	Crown/1 <sup>st</sup> Strain Gage
<b>UR9</b>	Equal

#### 4.1.2. Comparison of the Pipe Displacements

In the tests, pipes were translated both horizontally and vertically for  $X/D > 0$ , but only vertically for  $X/D = 0$ . The amount of displacement varied with pipe location. To find the amount of displacement, initial and final photos were compared. Four points were selected in the pipe (one at the crown, two at the springline, and one at the bottom of the pipe), and their coordinates were found by using the AutoCAD software, as shown in Figure 4.17. To quantify the amount of displacements, a scale should be used. In this work, as a control point, screws located at the upper part of the test box were used. As they are stable, distance among them did not change during the test; therefore, this distance was used as a scale.

Subsequently, the amount of displacement was divided to the final footing displacement (2cm). In this way, normalized displacements were obtained. This analysis is tabulated in Table 4.6 and Table 4.7, and illustrated graphically in Figure 4.18 and Figure 4.19.

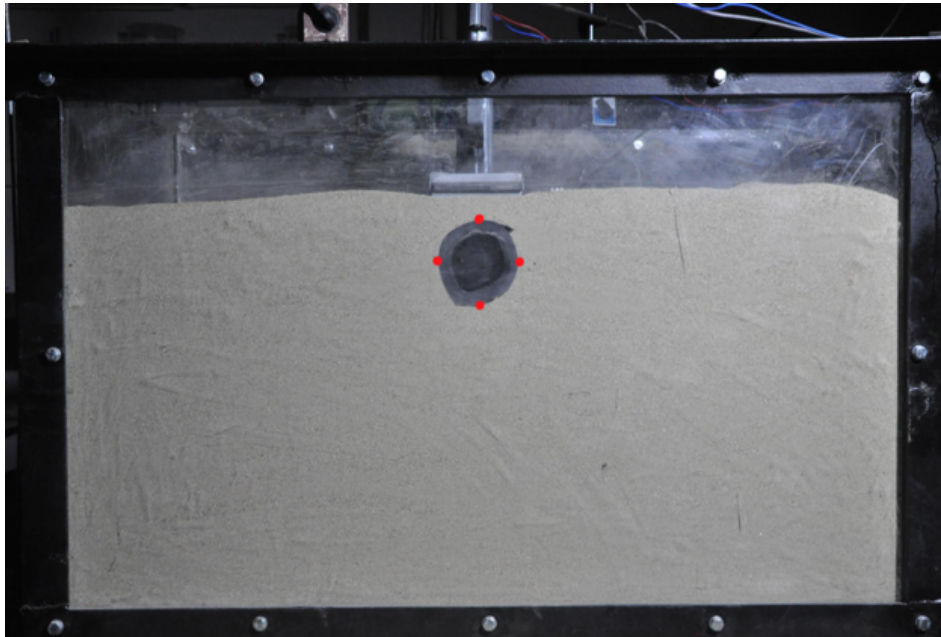


Figure 4.17. Determining pipe displacement for UR1 test.

Table 4.6. Normalized pipe displacement comparison for  $X/D > 0$ .

Experiment No	Normalized Horizontal Displacement	Normalized Vertical Displacement	$\lambda$
UR2	0.30	0.16	1.93
UR3	0.19	0.01	27.05
UR5	0.29	0.27	1.06
UR6	0.27	0.10	2.79
UR8	0.09	0.11	0.82
UR9	0.11	0.10	1.10

Table 4.7. Normalized pipe displacement comparison for  $X/D=0$ .

Experiment No	Normalized Vertical Displacement
UR1	0.78
UR4	0.82

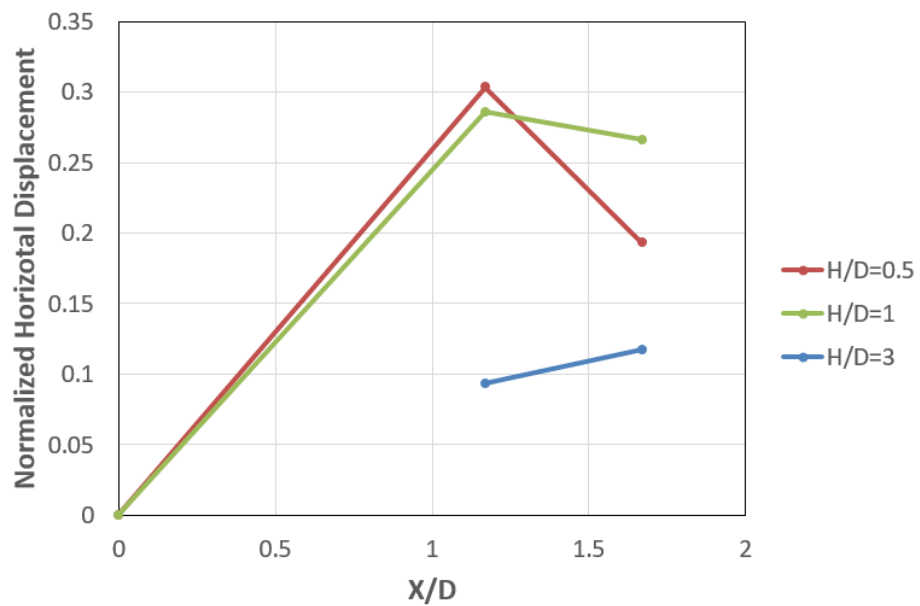


Figure 4.18. Normalized horizontal displacement for the tests.

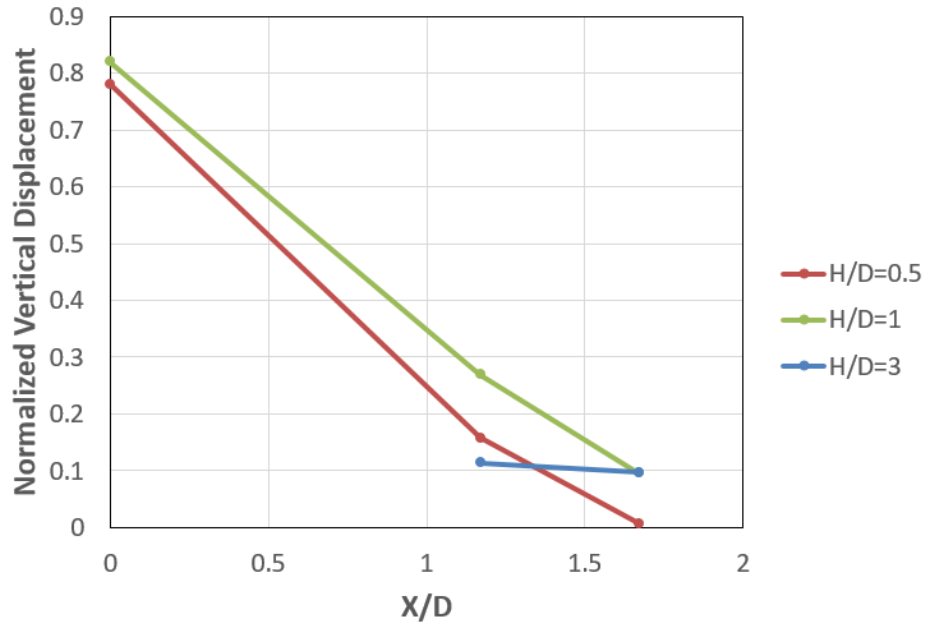


Figure 4.19. Normalized vertical displacement for the tests.

In Table 4.6,  $\lambda$  is the ratio of the normalized horizontal displacement to normalized vertical displacement, also can be seen in Equation 4.2:

$$\lambda = \frac{\text{Normalized horizontal displacement of the pipe}}{\text{Normalized vertical displacement of the pipe}} \quad (4.2)$$

$\lambda$  increased with the increase in the horizontal distance. This increase was very significant when pipe was placed at  $H/D=0.5$ , then it decreased with the increase in burial depth. In Table 4.7, normalized vertical displacement part is lacking due to no horizontal displacement in UR1 and UR4 tests. The reason behind the differences in  $\lambda$  can be explained with the angles between connection lines and the horizontal. In Table 4.8, except for UR9 test, it can easily seen that with the increase in the angle, lower  $\lambda$  ratios were obtained. This is meaningful, as this angle determines the direction that the soil displacement affects the pipe.

Also, whether the  $\lambda$  is higher than 1 or not can be found by using Table 4.5. For instance, in Table 4.5, most affected region from sand displacement was crown of the

Table 4.8. Change in  $\lambda$  with the angle of connection line with horizontal.

Experiment No	Angle	$\lambda$
UR2	41°	1.93
UR3	31°	27.05
UR5	52°	1.06
UR6	42°	2.79
UR8	72°	0.82
UR9	65°	1.10

pipe for UR8 test. This yielded more normalized vertical displacement compared to normalized horizontal displacement, and a  $\lambda$  value smaller than 1.

Besides, normalized displacement vectors were created for each test, shown in Figure 4.20. The angle between normalized displacement vectors with the horizontal are listed in Table 4.9.

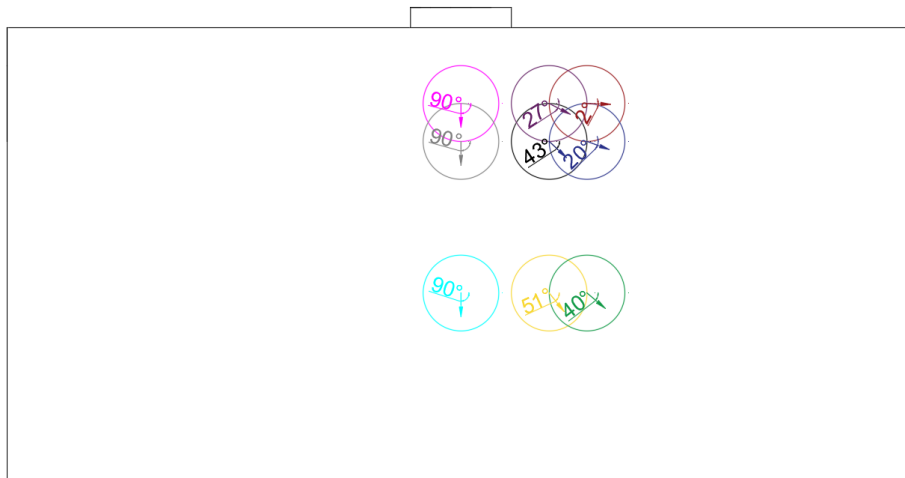


Figure 4.20. Normalized displacement vectors for the tests.

Table 4.9. Angle between normalized displacement vectors with the horizontal.

<b>Experiment No</b>	<b>Angle</b>
<b>UR2</b>	27°
<b>UR3</b>	2°
<b>UR5</b>	43°
<b>UR6</b>	20°
<b>UR8</b>	51°
<b>UR9</b>	40°

## 4.2. Analysis of the Pressure Acting on the Pipe

### 4.2.1. Effect of Burial Depth(H/D) on Pipe Pressure

To investigate the effect of burial depth on pipe pressure, results of the tests having the same X/D ratios were compared. In the analysis, pipe pressure at any settlement magnitude was divided to the foundation pressure at the same settlement magnitude. In this way, normalized pipe pressures were obtained for different settlement magnitudes and different pipe locations. Comparing these dimensionless normalized pipe pressures was considered to give more precise results. In Appendix, all of the test results will be given, but in this section, only the pressures at the maximum settlement were compared.. Pressures in this part were given as absolute values to ease the comparisons. In Appendix, they will be given with their signs.

The comparison of the normalized pressures in UR1-UR4-UR7 tests, UR2-UR5-UR8 tests, and UR3-UR6-UR9 tests can be seen in Table 4.10, Table 4.11, and Table 4.13, respectively. These tables are also illustrated as graphs, shown in Figure 4.21, Figure 4.22, and Figure 4.23.

In Table 4.10,  $\beta_1$  is the ratio of the pressure on the 1<sup>st</sup> strain gage to the foundation pressure,  $\beta_2$  is the ratio of the pressure on the 2<sup>nd</sup> strain gage to the foundation pressure,

Table 4.10. Comparison of the normalized pipe pressures of UR1-UR4-UR7 tests.

Experiment No	$\beta_1$	$\beta_2$	$\beta_3$	$\beta_4$
UR1	1.37	1.11	1.06	1.23
UR4	1.21	1.16	1.08	-
UR7	0.31	0.29	0.27	0.29

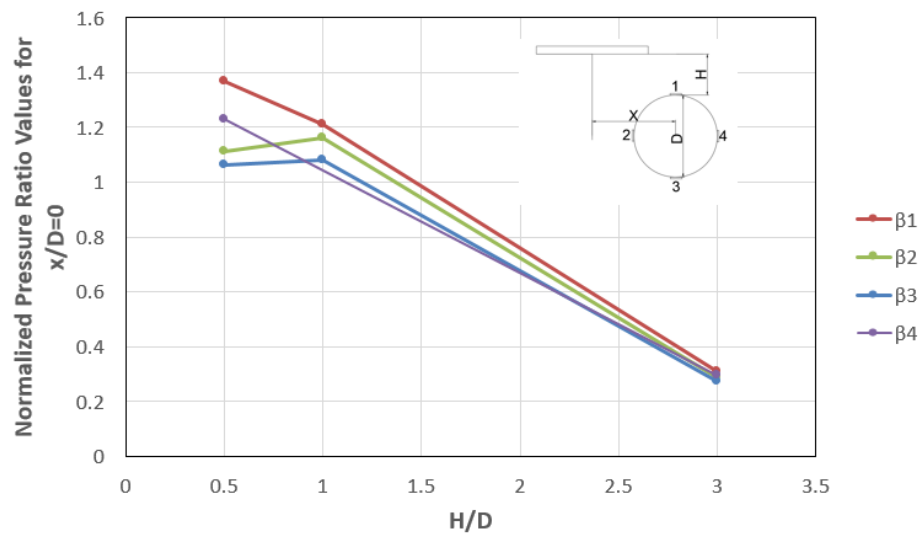


Figure 4.21. Illustration of the normalized pipe pressures of UR1-UR4-UR7 tests.

$\beta_3$  is the ratio of the pressure on the 3<sup>rd</sup> strain gage to the foundation pressure, and  $\beta_4$  is the ratio of the pressure of the 4<sup>th</sup> strain gage to the foundation pressure.  $\beta_1$  is also defined in Equation 4.3:

$$\beta_1 = \frac{\text{Pressure acting on the 1}^{st} \text{ strain gage}}{\text{Pressure acting on the foundation at the same amount of settlement}} \quad (4.3)$$

The same ratios were used also in Table 4.10-Table 4.20. Unfortunately, due to a technical problem,  $\beta_4$  could not be recorded in tests UR4, UR5, and UR6.

In Table 4.10, there was not a significant difference between UR1 and UR4 tests; however, all of the ratios decreased dramatically when H/D=3 condition was reached. In all of the tests in Table 4.10,  $\beta_1$  was the highest. This may be due to the position of the 1<sup>st</sup> strain gage, which was nearest to the pipe in UR1-UR4-UR7 tests.

Table 4.11. Comparison of the normalized pipe pressures of UR2-UR5-UR8 tests.

<b>Experiment No</b>	$\beta_1$	$\beta_2$	$\beta_3$	$\beta_4$
<b>UR2</b>	0.03	0.01	0.01	0.02
<b>UR5</b>	0.15	0.24	0.18	-
<b>UR8</b>	0.18	0.12	0.09	0.09

While the photos were being investigated in UR2 test, a rotation of the pipe in counterclockwise direction during the test was observed. This rotation was not encountered in the other tests, only translation was observed. This rotation led to a change in the pressure values. To illustrate this change clearly, Table 4.12 was created, in which pressure values were not given as absolute values. As seen in Table 4.12, pressure values recorded by 3<sup>rd</sup> strain gage were compressive (positive sign designates compression) between 4mm-16mm, but they became tensile between 16mm-20mm. UR2 test results were still used in this section, to show the pressure range. In Table 4.11, it is seen that the lowest pressure ratios were reached when the pipe was placed at H/D=0.5.

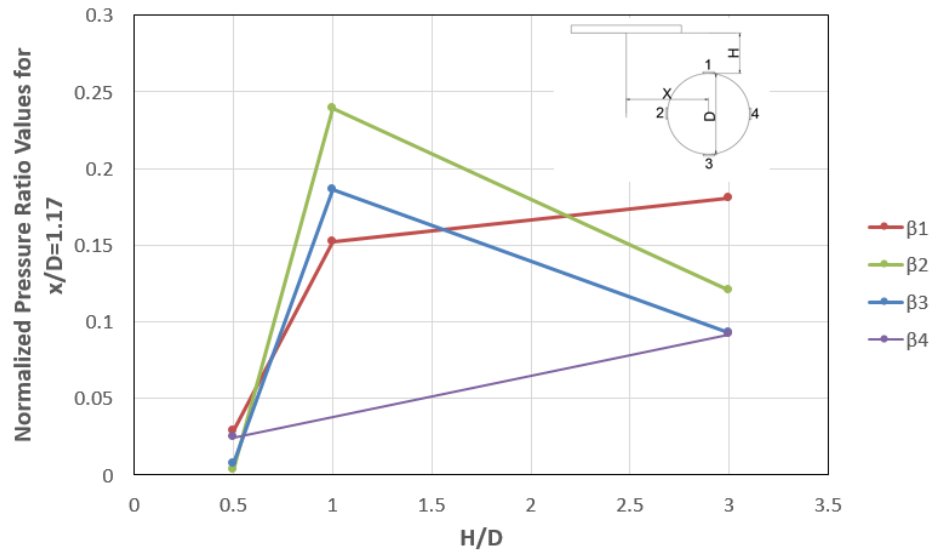


Figure 4.22. Illustration of the normalized pipe pressures of UR2-UR5-UR8 tests.

Pressure ratios in UR5 and UR8 tests were somewhat close; however, there were some minor differences. In UR5 test,  $\beta_1$  was lower than  $\beta_2$ , while in UR8 test,  $\beta_2$  was lower than  $\beta_1$ . This was due to the direction of movement of the sand particles, shown in Table 4.5. In UR5 test, the most affected region of the pipe from the sand movement was left side of the pipe; therefore, it is meaningful to obtain higher values for  $\beta_2$  compared to  $\beta_1$ . Conversely, in UR8 test, the most affected region of the pipe from the sand movement was the crown of the pipe, which explains the reason for obtaining higher values for  $\beta_1$  compared to  $\beta_2$ .

Table 4.12. Change in the pressure at the 3<sup>rd</sup> strain gage with displacement.

Experiment No	Pressure at the 3 <sup>rd</sup> Strain Gage(kPa)
UR2-0.4cm	0.33
UR2-0.8cm	0.80
UR2-1.2cm	0.58
UR2-1.6cm	0.06
UR2-2.0cm	-0.37

Table 4.13. Comparison of the normalized pipe pressures of UR3-UR6-UR9 tests.

Experiment No	$\beta_1$	$\beta_2$	$\beta_3$	$\beta_4$
<b>UR3</b>	0.03	0.07	0.05	0.08
<b>UR6</b>	0.08	0.14	0.12	-
<b>UR9</b>	0.09	0.10	0.15	0.07

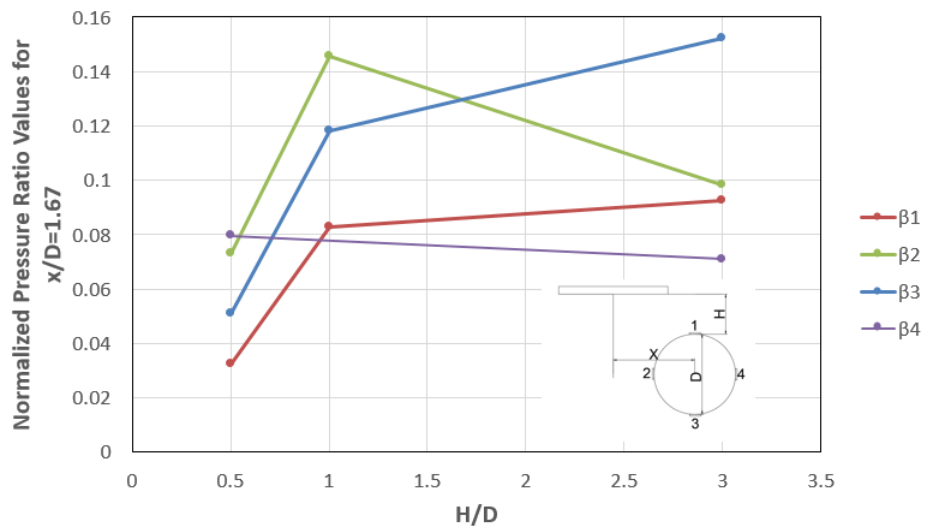


Figure 4.23. Illustration of the normalized pipe pressures of UR3-UR6-UR9 tests.

As seen in Table 4.13, approximately same pressure ratios were reached in UR6 and UR9 tests. In Table 4.5, for UR6 test, most affected region of the pipe from the sand movement is the left part, while crown and left side of the pipe were affected approximately same from the sand movement in UR9 test. This leads to have approximately same  $\beta_1$  and  $\beta_2$  values for UR9 test, and obtaining higher values for  $\beta_2$  compared to  $\beta_1$  for UR6 test.

In Table 4.11 and Table 4.13, the lowest pressures were recorded when the pipe was placed at  $H/D=0.5$ . This may be seen conflicting with the results of Table 4.10; however, it is not, which will be explained in detail in the next sub-section.

#### 4.2.2. Effect of Horizontal Distance( $X/D$ ) on Pipe Pressure

To investigate the effect of horizontal distance on pipe pressure, results of the tests having same  $H/D$  ratios are compared. Comparison of the normalized pipe pressures of UR1-UR2-UR3, UR4-UR5-UR6, and UR7-UR8-UR9 is tabulated in Table 4.14, Table 4.15, and Table 4.16 respectively. These tables are illustrated as graphs in Figure 4.24, Figure 4.25 and Figure 4.26.

Table 4.14. Comparison of the normalized pipe pressures of UR1-UR2-UR3 tests.

<b>Experiment No</b>	$\beta_1$	$\beta_2$	$\beta_3$	$\beta_4$
<b>UR1</b>	1.36	1.11	1.06	1.22
<b>UR2</b>	0.03	0.01	0.01	0.02
<b>UR3</b>	0.03	0.07	0.05	0.08

Table 4.15. Comparison of the normalized pipe pressures of UR4-UR5-UR6 tests.

<b>Experiment No</b>	$\beta_1$	$\beta_2$	$\beta_3$	$\beta_4$
<b>UR4</b>	1.21	1.16	1.08	-
<b>UR5</b>	0.15	0.24	0.18	-
<b>UR6</b>	0.08	0.14	0.12	-

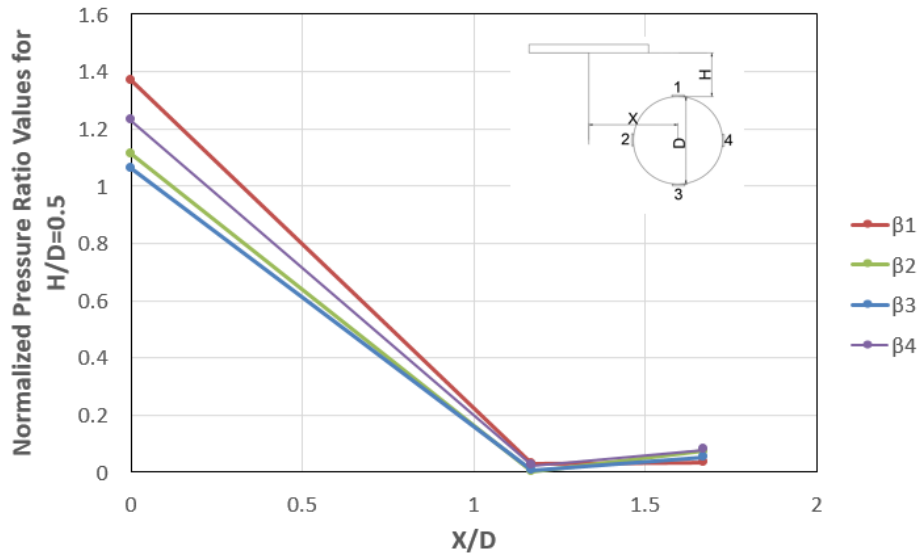


Figure 4.24. Illustration of the normalized pipe pressures of UR1-UR2-UR3 tests.

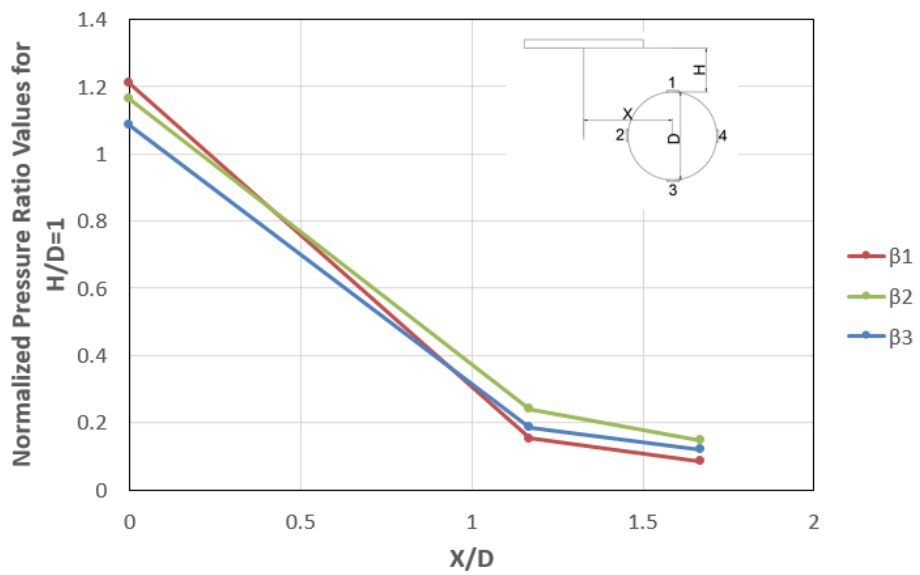


Figure 4.25. Illustration of the normalized pipe pressures of UR4-UR5-UR6 tests.

Table 4.16. Comparison of the normalized pipe pressures of UR7-UR8-UR9 tests.

Experiment No	$\beta_1$	$\beta_2$	$\beta_3$	$\beta_4$
<b>UR7</b>	0.31	0.29	0.27	0.29
<b>UR8</b>	0.18	0.12	0.09	0.09
<b>UR9</b>	0.09	0.10	0.15	0.07

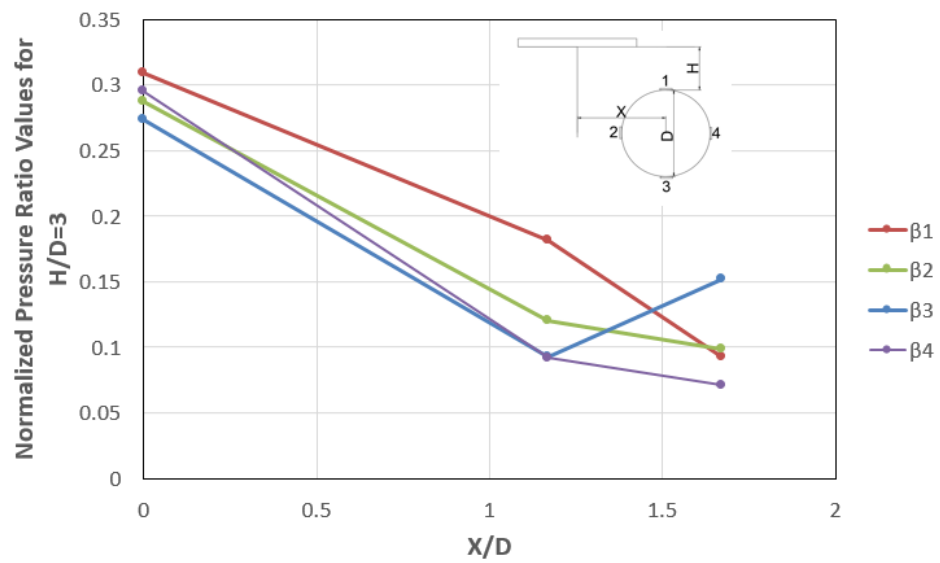


Figure 4.26. Illustration of the normalized pipe pressures of UR7-UR8-UR9 tests.

In both Table 4.14, 4.15, and 4.16, pressure ratios decreased with the increase in horizontal distance. When the pipe was placed at  $H/D=0.5$ , with the increase in horizontal distance, a severe drop in pressure was observed. This severeness tended to decrease with the increase in burial depth. For instance, in Table 4.16, the difference between UR7 and UR9 tests were smaller than UR1 and UR3 tests in Table 4.14.

To explain the reason of this severeness, again the angle between the connection line and the horizontal was used, shown in Figure 4.3. Also, for the same  $H/D$  condition,  $\beta_1$  of the tests having  $X/D>0$  were divided to  $\beta_1$  of the test where  $X/D=0$ , and called as  $\Gamma_1$ . This was done to quantify the severeness. Definiton of  $\Gamma_1$  can be seen also in Equation 4.4:

$$\Gamma_1 = \frac{\beta_1 \text{ of the tests having } X/D > 0}{\beta_1 \text{ of the test where } X/D = 0 \text{ at the same burial depth}} \quad (4.4)$$

This angle and  $\Gamma_1$  is tabulated in Table 4.17.

Table 4.17.  $\Gamma_1$  and the angle of the connection line with the horizontal.

<b>Experiment No</b>	$\Gamma_1$	<b>Angle</b>
<b>UR3</b>	0.02	31°
<b>UR5</b>	0.13	52°
<b>UR6</b>	0.07	42°
<b>UR8</b>	0.59	72°
<b>UR9</b>	0.30	65°

In Table 4.17, it is clear that with the decrease in the angle, a lower  $\Gamma_1$  values were observed, meaning a more severe drop in the pressure values.

#### **4.2.3. Effect of the Amount of the Settlement on Pipe Pressure**

The effect of the amount of the settlement on pipe pressure differs significantly with the location of the pipe. To show this, Tables 4.18-4.20 were created in which

the change in pressure acting different strain gages with the amount of settlement was presented.

For instance, in general, in UR1 and UR4 tests increase in the amount of pressure leads to an increase in the pressure ratios, that can be seen in Table 4.18, Figure 4.27, and Figure 4.28.

Table 4.18. Effect of the foundation settlement on UR1-UR4 tests.

Experiment No	$\beta_1$	$\beta_2$	$\beta_3$	$\beta_4$
UR1-1.2cm	1.22	0.99	1.00	1.06
UR1-1.6cm	1.30	1.08	1.06	1.17
UR1-2.0cm	1.36	1.11	1.06	1.23
UR4-1.2cm	1.08	1.03	1.03	-
UR4-1.6cm	1.16	1.11	1.08	-
UR4-2.0cm	1.21	1.16	1.08	-

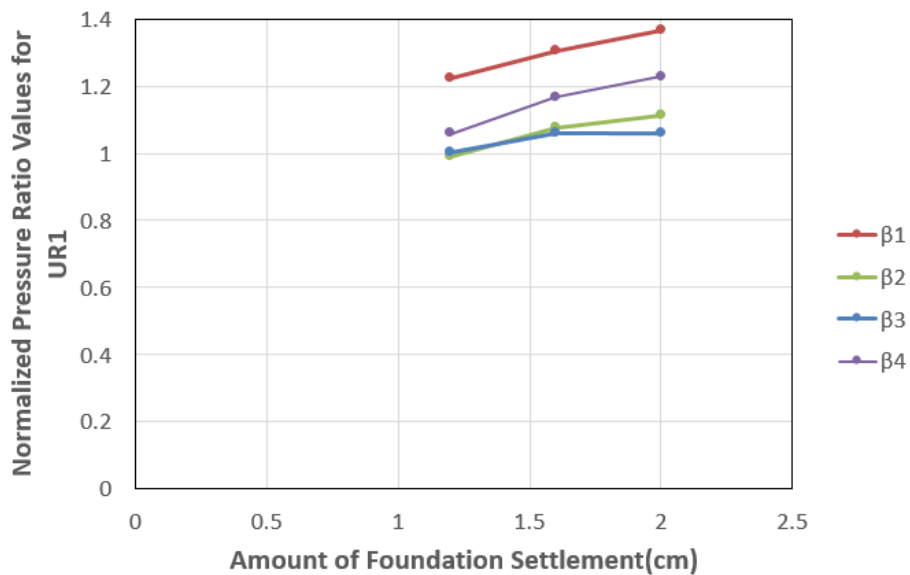


Figure 4.27. Illustration of the effect of the foundation settlement on UR1 test.

When  $H/D=3$  condition was reached, it was observed that increase in the amount on settlement did not significantly affect the pressure ratios, as shown in Table 4.19, Figure 4.29, Figure 4.30, and Figure 4.31.

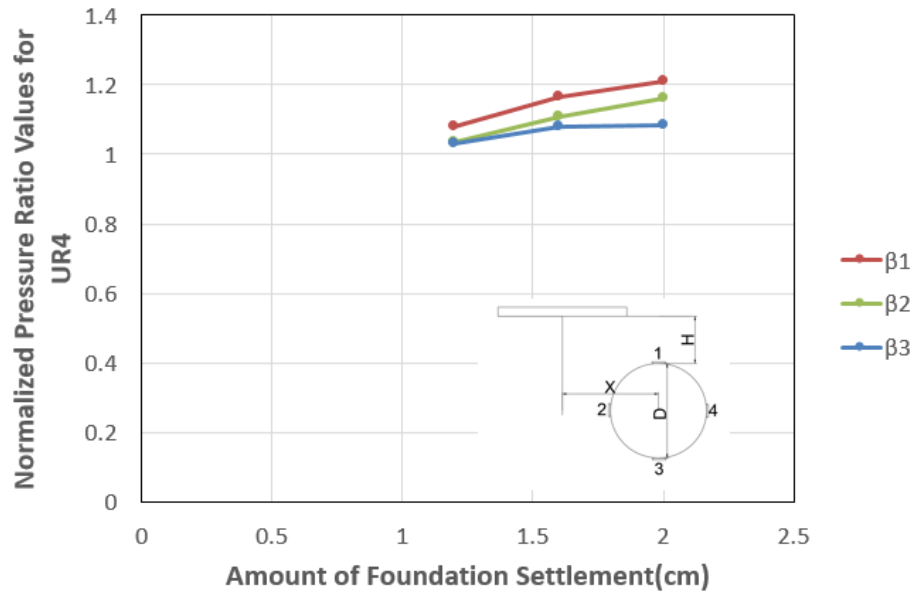


Figure 4.28. Illustration of the effect of the foundation settlement on UR4 test.

Table 4.19. Effect of the foundation settlement on UR7-UR8-UR9 tests.

Experiment No	$\beta_1$	$\beta_2$	$\beta_3$	$\beta_4$
UR7-1.2cm	0.31	0.23	0.24	0.28
UR7-1.6cm	0.32	0.27	0.27	0.30
UR7-2.0cm	0.31	0.29	0.27	0.29
UR8-1.2cm	0.14	0.13	0.08	0.04
UR8-1.6cm	0.13	0.12	0.08	0.05
UR8-2.0cm	0.18	0.12	0.09	0.09
UR9-1.2cm	0.09	0.11	0.15	0.05
UR9-1.6cm	0.08	0.10	0.15	0.06
UR9-2.0cm	0.09	0.09	0.15	0.07

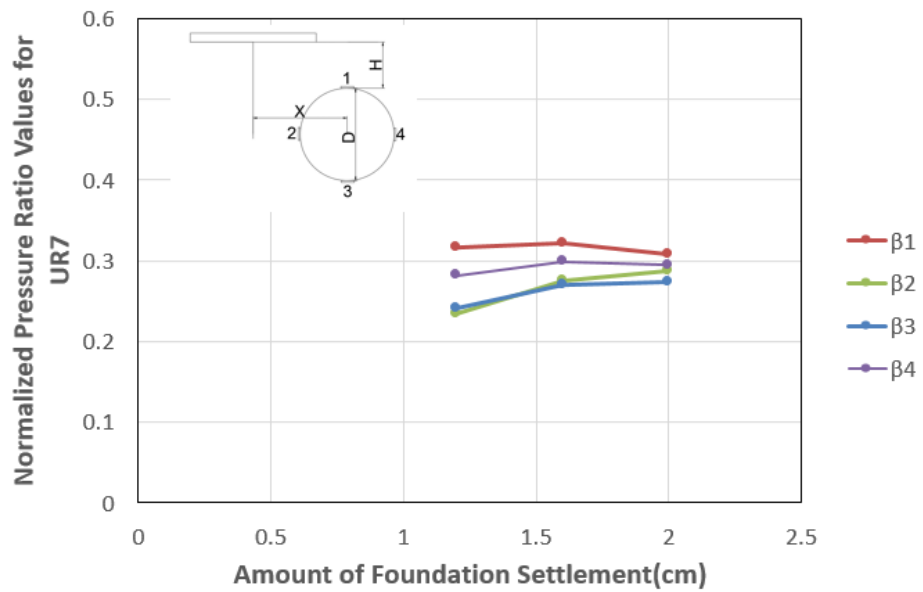


Figure 4.29. Illustration of the effect of the foundation settlement on UR7 test.

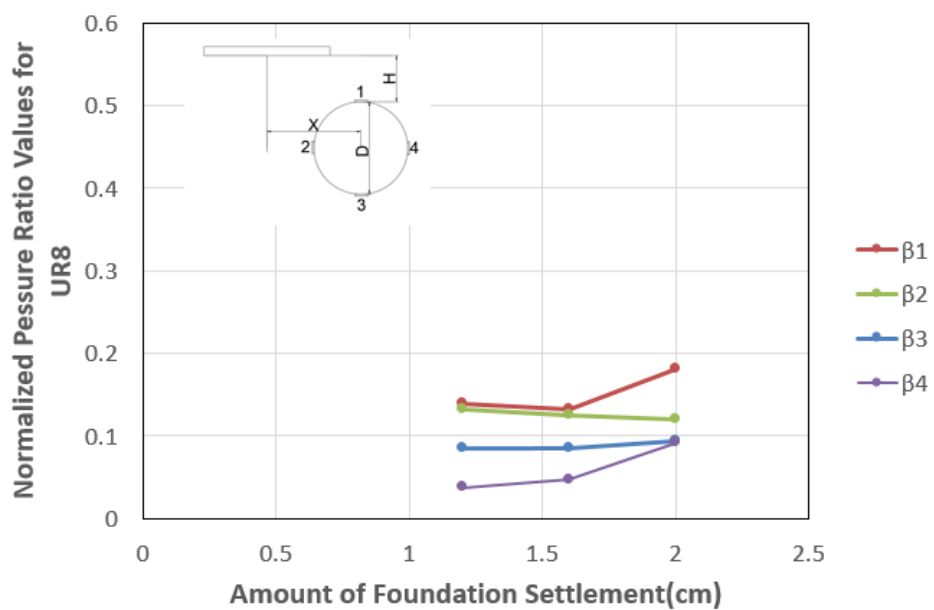


Figure 4.30. Illustration of the effect of the foundation settlement on UR8 test.

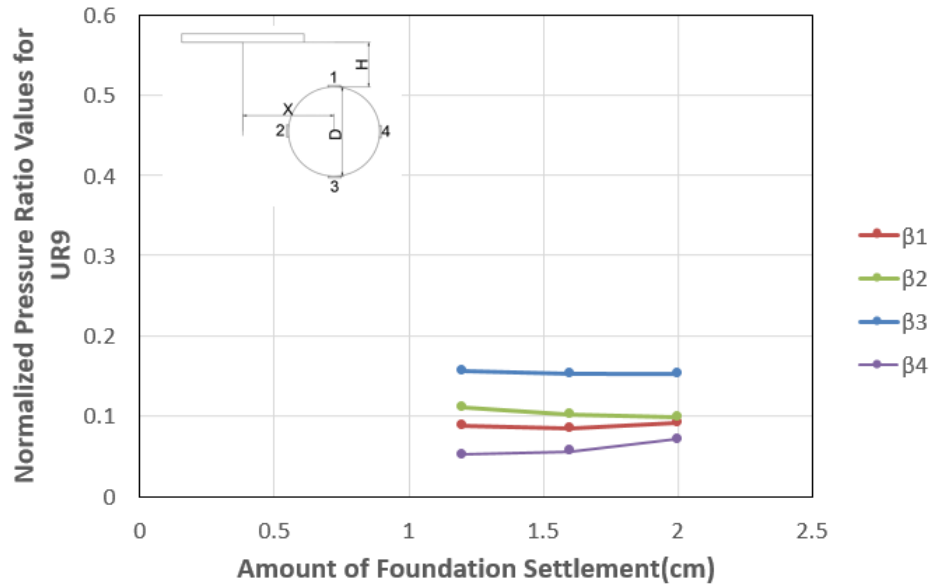


Figure 4.31. Illustration of the effect of the foundation settlement on UR9 test.

In tests UR3, UR5, and UR6, with the increase in the amount of foundation settlement, pipe translated towards right. This led different effects on different strain gages. In Table 4.5, it can be seen that in these tests, left part of the pipe was affected most from the pipe displacement. As the top of the pipe in those test was not affected from the pressure significantly,  $\beta_1$  decreased a little bit with the increase in the amount of pressure. Decrease in  $\beta_1$  did not mean a decrease in 1<sup>st</sup> strain gage, in some cases, although there was an increase in 1<sup>st</sup> strain gage,  $\beta_1$  decreased. This was due to a higher increase in the foundation pressure.

Pressure acting at the 2<sup>nd</sup> strain gage increased with the amount of the foundation displacement, which is meaningful as the left side was the most affected part of the pipe. However, this increase was not very significant, which led  $\beta_2$  to not change significantly with the increase in displacement. Changes in the 1<sup>st</sup> strain gage, 2<sup>nd</sup> strain gage,  $\beta_1$ , and  $\beta_2$  can be found in Table 4.20.

Table 4.20. Effect of the foundation settlement on UR3-UR5-UR6 tests.

<b>Experiment No</b>	$\beta_1$	<b>Pressure at the 1<sup>st</sup> Strain Gage (kPa)</b>	$\beta_2$	<b>Pressure at the 2<sup>nd</sup> Strain Gage (kPa)</b>
<b>UR3-1.2cm</b>	0.05	-1.52	0.07	2.48
<b>UR3-1.6cm</b>	0.04	-1.53	0.08	2.97
<b>UR3-2.0cm</b>	0.03	-1.41	0.07	3.19
<b>UR5-1.2cm</b>	0.17	-5.81	0.23	8.00
<b>UR5-1.6cm</b>	0.16	-6.44	0.24	9.94
<b>UR5-2.0cm</b>	0.15	-6.77	0.24	10.67
<b>UR6-1.2cm</b>	0.09	-3.38	0.14	5.24
<b>UR6-1.6cm</b>	0.08	-3.44	0.14	5.80
<b>UR6-2.0cm</b>	0.08	-3.77	0.14	6.66

## 5. DISCUSSION

First of all, this analysis was a clear demonstration of how the image analysis enhance the understanding of the behavior in physical modelling tests. Nearly all of the data obtained by strain gages and load cell became more meaningful when it was reinforced with the image analysis results.

To protect buried pipe structures from the excessive load application from the surface, one thing that comes to the mind is to bury the pipe deeper to the soil layer. As the effect of applied stress diminishes with the increasing depth, this is a meaningful approach. This is shown also in Table 4.10, in which when the burial depth reached  $H/D=3$ , normalized pressure ratios reached 0.3, which can be considered as safe for the installment.

However, installing the pipe not directly under the foundation yielded even better results. Interestingly, this yielded even lower pressure ratios when the pipe was very near to the surface. This is tried to be explained by the angles between a line that links the centers of the pipe and foundation and the horizontal. When this angle gets smaller, more severe normalized pressure drops were observed. Therefore, it can be proposed that if the applied load was not vertically aligned with the pipe, it is safe to place the pipe to shallower depths. This approach will also be more economic and less time-consuming. But if there is not enough distance, pipe can be exposed to torsion, as seen in UR2 test, which can pose unexpected problems.

Besides, with the implementation of the buried pipe systems, alterations were observed in the affected zones. Increase in burial depth led to increase in areal and vertical extent of the affected region. Therefore, burying the pipe to deeper layers can not always be considered as safe, because there might be an increased disturbance to the surroundings with the load application. Again, this increase diminishes when the pipe placed at shallower depths, with an enough horizontal distance from the centerline

of the foundation.

Taking everything into consideration, placing a pipe to a place where the angle between the connection line and the horizontal is small, yields best results in terms of pressures acting on the pipe and extent of the affected region.

As a future research, experiments can be conducted with a denser soil packing. With the increase in relative density, both pressures acting on the pipe and affected zone will be altered. Also, tests can be done with geosynthetic reinforcement. Although there are numerous studies in the literature in which effect of geosynthetics on the pressures acting on the pipe, image analysis was not used in most of them. Therefore, change in the affected zone may be investigated with the implementation of geosynthetic reinforcements to the system.

## 6. CONCLUSIONS

In this study, the goal is to investigate the effects of the location of buried pipes on the pressures acting on buried pipe and extent of the affected region. To manage this, a small scale 1g physical model box was manufactured, and several physical model tests were done inside the box within the scope of TUBITAK Project No. 116R020. Index properties of the tested sand were found by laboratory experiments, while necessary strength parameters were determined by triaxial testing. Results were obtained by means of strain gages stuck on the pipe and by analyzing photos, which were used to evaluate the displacements in the system.

From the PIV analysis, it was observed that the installment of the pipe has an effect on the area of the affected zone. This effect deteriorated when the pipe was translated horizontally. Also, through vector analysis, the most affected part of the pipes from the sand displacement was visualized, and this visualization was then used to assess the pressure differences in the pipe circumference.

From the data obtained from strain gages, it was observed that the location of the pipe has a significant effect on the pressures acting on the pipe. At the same burial depth, an increase in the horizontal distance led to a decrease in the normalized pressures. However, at the same  $X/D$  ratios, an increase in the burial depth led to more complex results. It was found that when the pipe was located at  $X/D=0$ , with the increase in burial depth, normalized pressures decreased. On the other hand, when the pipe was located at  $X/D>0$ , normalized pipe pressures reached the lowest values when the pipe was placed at  $H/D=0.5$ . This contradiction was explained with the angle between horizontal and the connection line of the pipe center and footing center. With the decrease in this angle, a more severe drop in the pressure values was observed.

## REFERENCES

- Altunbas, A., 2015, *Influence of Dilatancy on Slip Planes and on Localization of Strains*, Ph.D. Dissertation, Bogazici University.
- American Society of Testing and Materials, 2007, “*Standard Test Method for Particle Size Analysis of Soils*”, ASTM Standards: D422-63(2007)e2.
- American Society of Testing and Materials, 2014, “*Standard Test Methods for Specific Gravity of Soil Solids by Water Pycnometer*”, ASTM Standards: ASTM D854-14.
- American Society of Testing and Materials, 2016, “*Standard Test Methods for Maximum Index Density and Unit Weight of Soils Using a Vibratory Table*”, ASTM Standards: D4253-16e1.
- American Society of Testing and Materials, 2016, “*Standard Test Methods for Minimum Index Density and Unit Weight of Soils and Calculation of Relative Density*”, ASTM Standards: D4254-16.
- Balla, A., 1962, “Bearing Capacity of Foundations”, *ASCE J Soil Mech Found Div*, Vol. 88, No. 5, pp. 13-34.
- Bildik, S. and M. Laman, 2015, “Experimental Investigation of the Effects of Pipe Location on the Bearing Capacity”, *Geomechanics and Engineering*, Vol. 8, No. 2, pp. 221-235.
- Bildik, S. and M. Laman, 2019, “Experimental Investigation of Soil-Structure-Pipe Interaction”, *KSCE Journal of Civil Engineering*, Vol. 23, No. 9, pp. 3753-3763.
- Chen, Y., F. Lu, A. Namdar, and J. Cai, 2019, “Working mechanism of Pile Group

with Different Pile Spacing”, *Advances in Civil Engineering*, Vol. 2019, Article ID 5376594.

Cinicioglu, O. and A. Abadkon, 2015, “Dilatancy and Friction Angles Based on In-Situ Soil Conditions”, *Journal of Geotechnical and Geoenvironmental Engineering*, Vol. 141, No. 4, pp. 1-7.

Corey, R., J. Han, D.K. Khatri and R.L. Parsons, 2014, “Laboratory Study on Geosynthetic Protection of Buried Steel-Reinforced HDPE Pipes from Static Loading”, *Journal of Geotechnical and Geoenvironmental Engineering*, Vol. 140, No. 6, pp. 1-10.

Das, B.M., 2009, *Shallow foundations: Bearing Capacity and Settlement*, 2<sup>nd</sup> edition, CRC Press, London.

Fattah, M.Y., W.H. Hassan and S.E. Rasheed, 2018, “Behavior of Flexible Buried Pipes under Geocell Reinforced Subbase Subjected to Repeated Loading”, *International Journal of Geotechnical Earthquake Engineering*, Vol. 9, No. 1, pp. 22-41.

Ghalehjough, B.K., S. Akbulut and S. Celik, 2018, “Effect of Particle Roundness and Morphology on the Shear Failure Mechanism of Granular Soil under Strip Footing”, *Acta Geotechnica Slovenica*, Vol. 15, No. 1, pp. 43-53.

Hegde, A.M. and T.G. Sitharam, 2015, “Experimental and Numerical Studies on Protection of Buried Pipelines and Underground Utilites Using Geocells”, *Geotextiles and Geomembranes*, Vol. 43, No. 5, pp. 372-381.

Hu, G.G.Y., 1964, “Variable-Factors Theory of Bearing Capacity”, *ASCE J Soil Mech Found Div*, Vol. 90, No. 4, pp. 85-95.

Khalaj, O., M. Azizian, S.N. Moghaddas Tafreshi and B. Masek, 2017, “Laboratory

- Investigation of Buried Pipes Using Geogrid and EPS Geofam Block”, *IOP Conference Series: Earth and Environmental Science*, Vol. 95, No. 2, pp. 0-10.
- Kou, Y., S.K. Shukla and A. Mohyeddin, 2018, “Experimental Investigation for Pressure Distribution on Flexible Conduit Covered with Sandy Soil Reinforced with Geotextile Reinforcement of Varying Widths”, *Tunneling and Underground Space Technology*, Vol. 80, No. June, pp. 151-163.
- Martinez, A., S. Palumbo and B.D. Todd, 2019, “Bioinspiration for Anisotropic Load Transfer at Soil-Structure Interfaces”, *Journal of Geotechnical and Geoenvironmental Engineering*, Vol. 145, No. 10.
- Masada, T., 2000, “Modified Iowa Formula for Vertical Deflection of Buried Flexible Pipe”, *Journal of Transportation Engineering*, Vol. 126, No. 5, pp. 440-447.
- Meguid, M.A. and M.G. Hussein, 2017, “A Numerical Procedure for the Assessment of Contact Pressures on Buried Structures Overlain by EPS Geofam Inclusion”, *International Journal of Geosynthetics and Ground Engineering*, Vol. 3, No. 2, pp. 1-14.
- Meyerhof, G.G., 1951, “The Ultimate Bearing Capacity of Foundations”, *Geotechnique*, Vol. 2, No. 4, pp. 301-332.
- Meyerhof, G.G., 1963, “Some Recent Research on the Bearing Capacity of Foundations”, *Canadian Geotechnical Journal*, Vol. 1, No. 1, pp. 16-26.
- Mirzababaei, M., M. Mohamed and M. Mirafteb, 2017, “Analysis of Strip Footings on Fiber-Reinforced Slopes with the Aid of Particle Image Velocimetry”, *Journal of Materials in Civil Engineering*, Vol. 29, No. 4, pp. 1-14.
- Moghaddas Tafreshi, S.N. and O. Khalaj, 2008, “Laboratory Tests of Small-Diameter

- HDPE Pipes Buried in Reinforced Sand under Repeated-Load”, *Geotextiles and Geomembranes*, Vol. 26, No. 2, pp. 145-163.
- Nanda, S. and N.R. Patra, 2015, “Determination of Soil Properties for Plane Strain Condition from the Triaxial Tests Results”, *International Journal for Numerical and Analytical Methods in Geomechanics*, Vol. 39, No. 9, pp. 1014-1026.
- Öner, C., Ç. Arda and Ö. Çinicioglu, 2019, “Influence of Grain Size and Shape on Evaluation of Shear Zone Geometry.”, *27th European Young Geotechnical Engineers Conference*.
- Pires, A.C.G. and E.M. Palmeria, 2017, “Geosynthetic Protection for Buried Pipes Subjected to Surface Surcharge Loads”, *International Journal of Geosynthetics and Ground Engineering*, Vol. 3, No. 4, pp. 1-11.
- Saglamer, A. and M. Balkaya, 2015, “Gömülü Boru Hatlarının Statik ve Dinamik Yükler Altındaki Davranışı”, *Antalya Yöresinin İnşaat Sorunları Kongresi*, pp. 121-133.
- Sargand, S., T. Masada, B. Tarawneh and D. Gruver, 2005, “Field Performance and Analysis of Large-Diameter High-Density Polyethylene Pipe under Deep Soil Fill”, *Journal of Geotechnical and Geoenvironmental Engineering*.
- Schanz, T. and P.A. Vermeer, 1996, “Angles of Friction and Dilatancy of Sand”, *Geotechnique*, Vol. 46, No. 1, pp. 145-151.
- Stanier, S.A., J. Blaber, W.A. Take and D.J. White, 2016, “Improved Image-Based Deformation Measurement for Geotechnical Applications”, *Canadian Geotechnical Journal*, Vol. 53, No. 5, pp. 727-739.
- Terzaghi, K., 1943, *Theoretical Soil Mechanics*, Wiley, New York.

- Terzi, N.U., F. Yilmazturk, S. Yildirim and H. Kilic, 2012, “Experimental Investigations of Backfill Conditions on the Performance of High-Density Polyethelene Pipes”, *Experimental Techniques*, Vol. 36, No.2, pp.40-49.
- Vesic, A.S., 1973, “Analysis of Ultimate Loads of Shallow Foundations”, *ASCE J Soil Mech Found Div*, Vol. 99, No. 1, pp. 45-73.
- Wang, F., J. Han, D.K. Khatri, R.L. Parsons, and R. Corey, 2020, “Time-Dependent Field Performance of Steel-Reinforced High-Density Polyethylene Pipes in Soil”, *Journal of Geotechnical and Geoenvironmental Engineering*, Vol. 146, No. 1, pp. 1-11.
- White, D.J., W.A. Take, and M.D. Bolton, 2003, “Soil Deformation Measurement Using Particle Image Velocimetry (PIV) and Photogrammetry”, *Geotechnique*, Vol. 53, No. 7, pp. 619-631.
- Won, M.S., H.I. Ling and Y.S. Kim, 2004, “A Study of the Deformation of Flexible Pipes Buried under Model Reinforced Sand”, *KSCE Journal of Civil Engineering*, Vol. 8, No. 4, pp. 377-385.
- Witthoeft, A.F. and H. Kim, 2016, “Numerical Invesitgation of Earth Pressure Reduction on Buried Pipes Using EPS Geofoam Compressible Inclusions”, *Geosynthetics International*, Vol. 23, No. 4, pp. 287-300.
- Zhang, W. and A. Askarinejad, 2019, “Behaviour of Buried Pipes in Unstable Sandy Slopes”, *Landslides*, Vol. 16, No. 2, pp. 283-293.

**APPENDIX A: PRESSURE VALUES ON THE  
DIFFERENT STRAIN GAGES IN EACH TEST**

Table A.1. Pressures in the UR1 test.

<b>Experiment No</b>	<b>Pressure at the Foundation (kPa)</b>	<b>Pressure at the 1<sup>st</sup> Strain Gage (kPa)</b>	<b>Pressure at the 2<sup>nd</sup> Strain Gage (kPa)</b>	<b>Pressure at the 3<sup>rd</sup> Strain Gage (kPa)</b>	<b>Pressure at the 4<sup>th</sup> Strain Gage (kPa)</b>
<b>UR1-0.2cm</b>	4.15	3.09	-2.17	1.77	-2.26
<b>UR1-0.4cm</b>	9.99	8.22	-6.41	6.19	-6.59
<b>UR1-0.6cm</b>	15.20	14.95	11.63	11.68	-12.26
<b>UR1-0.8cm</b>	20.05	21.79	-17.17	17.42	-18.22
<b>UR1-1.0cm</b>	24.77	28.72	-22.98	23.43	-24.56
<b>UR1-1.2cm</b>	29.10	35.63	-28.89	29.19	-30.81
<b>UR1-1.4cm</b>	33.83	42.90	-35.19	35.19	-37.54
<b>UR1-1.6cm</b>	37.42	48.82	-40.31	39.74	-43.65
<b>UR1-1.8cm</b>	40.58	54.27	-44.57	43.19	-48.72
<b>UR1-2.0cm</b>	43.11	58.89	-47.93	45.76	-53.01

Table A.2. Pressures in the UR2 test.

<b>Experiment No</b>	<b>Pressure at the Foundation (kPa)</b>	<b>Pressure at the 1<sup>st</sup> Strain Gage (kPa)</b>	<b>Pressure at the 2<sup>nd</sup> Strain Gage (kPa)</b>	<b>Pressure at the 3<sup>rd</sup> Strain Gage (kPa)</b>	<b>Pressure at the 4<sup>th</sup> Strain Gage (kPa)</b>
<b>UR2-0.2cm</b>	9.50	-0.21	-0.26	-0.21	0.45
<b>UR2-0.4cm</b>	16.89	-0.69	-1.36	0.33	0.54
<b>UR2-0.6cm</b>	22.94	-0.95	-2.34	0.74	0.39
<b>UR2-0.8cm</b>	28.30	-1.25	-2.65	0.80	0.47
<b>UR2-1.0cm</b>	32.86	-1.44	-2.57	0.66	0.48
<b>UR2-1.2cm</b>	36.90	-1.37	-2.06	0.58	0.60
<b>UR2-1.4cm</b>	40.10	-1.32	-1.54	0.35	0.62
<b>UR2-1.6cm</b>	42.52	-1.14	-0.63	0.06	0.79
<b>UR2-1.8cm</b>	44.71	-1.40	-0.20	-0.27	1.07
<b>UR2-2.0cm</b>	46.60	-1.34	0.15	-0.37	1.15

Table A.3. Pressures in the UR3 test.

<b>Experiment No</b>	<b>Pressure at the Foundation (kPa)</b>	<b>Pressure at the 1<sup>st</sup> Strain Gage (kPa)</b>	<b>Pressure at the 2<sup>nd</sup> Strain Gage (kPa)</b>	<b>Pressure at the 3<sup>rd</sup> Strain Gage (kPa)</b>	<b>Pressure at the 4<sup>th</sup> Strain Gage (kPa)</b>
<b>UR3-0.2cm</b>	7.42	-0.39	0.49	-0.35	0.63
<b>UR3-0.4cm</b>	13.48	-0.72	0.96	-0.60	1.30
<b>UR3-0.6cm</b>	19.30	-1.04	1.34	-0.84	1.86
<b>UR3-0.8cm</b>	24.74	-1.26	1.70	-1.10	2.34
<b>UR3-1.0cm</b>	29.64	-1.43	2.06	-1.39	2.77
<b>UR3-1.2cm</b>	33.62	-1.53	2.48	-1.64	3.07
<b>UR3-1.4cm</b>	36.54	-1.57	2.81	-1.94	3.31
<b>UR3-1.6cm</b>	38.90	-1.52	2.97	-2.04	3.37
<b>UR3-1.8cm</b>	41.29	-1.43	3.06	-2.09	3.41
<b>UR3-2.0cm</b>	43.70	-1.41	3.19	-2.23	3.48

Table A.4. Pressures in the UR4 test.

<b>Experiment No</b>	<b>Pressure at the Foundation (kPa)</b>	<b>Pressure at the 1<sup>st</sup> Strain Gage (kPa)</b>	<b>Pressure at the 2<sup>nd</sup> Strain Gage (kPa)</b>	<b>Pressure at the 3<sup>rd</sup> Strain Gage (kPa)</b>	<b>Pressure at the 4<sup>th</sup> Strain Gage (kPa)</b>
<b>UR4-0.2cm</b>	7.01	5.24	-5.28	5.47	-
<b>UR4-0.4cm</b>	12.61	10.75	-10.54	10.79	-
<b>UR4-0.6cm</b>	17.73	16.02	-15.77	15.92	-
<b>UR4-0.8cm</b>	22.29	21.44	-20.94	21.03	-
<b>UR4-1.0cm</b>	26.14	26.90	-26.02	26.00	-
<b>UR4-1.2cm</b>	29.79	32.23	-30.83	30.74	-
<b>UR4-1.4cm</b>	32.98	37.19	-35.29	35.21	-
<b>UR4-1.6cm</b>	35.74	41.59	-39.65	38.60	-
<b>UR4-1.8cm</b>	38.49	45.75	-43.80	41.60	-
<b>UR4-2.0cm</b>	40.72	49.25	-47.35	44.10	-

Table A.5. Pressures in the UR5 test.

<b>Experiment No</b>	<b>Pressure at the Foundation (kPa)</b>	<b>Pressure at the 1<sup>st</sup> Strain Gage (kPa)</b>	<b>Pressure at the 2<sup>nd</sup> Strain Gage (kPa)</b>	<b>Pressure at the 3<sup>rd</sup> Strain Gage (kPa)</b>	<b>Pressure at the 4<sup>th</sup> Strain Gage (kPa)</b>
<b>UR5-0.2cm</b>	7.97	-1.32	0.65	-0.39	-
<b>UR5-0.4cm</b>	14.27	-2.68	1.72	-1.21	-
<b>UR5-0.6cm</b>	20.18	-3.71	3.22	-2.14	-
<b>UR5-0.8cm</b>	25.29	-4.57	4.82	-3.17	-
<b>UR5-1.0cm</b>	30.10	-5.26	6.47	-4.25	-
<b>UR5-1.2cm</b>	34.42	-5.81	8.00	-5.31	-
<b>UR5-1.4cm</b>	37.80	-6.16	9.09	-6.25	-
<b>UR5-1.6cm</b>	40.64	-6.44	9.94	-7.05	-
<b>UR5-1.8cm</b>	42.52	-6.71	10.63	-7.75	-
<b>UR5-2.0cm</b>	44.61	-6.77	10.67	-8.29	-

Table A.6. Pressures in the UR6 test.

<b>Experiment No</b>	<b>Pressure at the Foundation (kPa)</b>	<b>Pressure at the 1<sup>st</sup> Strain Gage (kPa)</b>	<b>Pressure at the 2<sup>nd</sup> Strain Gage (kPa)</b>	<b>Pressure at the 3<sup>rd</sup> Strain Gage (kPa)</b>	<b>Pressure at the 4<sup>th</sup> Strain Gage (kPa)</b>
<b>UR6-0.2cm</b>	9.64	-1.10	0.98	-0.59	-
<b>UR6-0.4cm</b>	17.80	-2.06	2.04	-1.31	-
<b>UR6-0.6cm</b>	23.80	-2.68	3.05	-2.11	-
<b>UR6-0.8cm</b>	29.11	-3.12	4.00	-2.85	-
<b>UR6-1.0cm</b>	33.39	-3.38	4.79	-3.55	-
<b>UR6-1.2cm</b>	36.58	-3.38	5.24	-3.97	-
<b>UR6-1.4cm</b>	39.58	-3.41	5.49	-4.32	-
<b>UR6-1.6cm</b>	42.12	-3.44	5.80	-4.60	-
<b>UR6-1.8cm</b>	44.02	-3.59	6.25	-4.99	-
<b>UR6-2.0cm</b>	45.61	-3.77	6.66	-5.41	-

Table A.7. Pressures in the UR7 test.

<b>Experiment No</b>	<b>Pressure at the Foundation (kPa)</b>	<b>Pressure at the 1<sup>st</sup> Strain Gage (kPa)</b>	<b>Pressure at the 2<sup>nd</sup> Strain Gage (kPa)</b>	<b>Pressure at the 3<sup>rd</sup> Strain Gage (kPa)</b>	<b>Pressure at the 4<sup>th</sup> Strain Gage (kPa)</b>
<b>UR7-0.2cm</b>	2.19	0.12	-0.06	0.08	-0.04
<b>UR7-0.4cm</b>	6.39	1.15	-0.63	0.63	-0.83
<b>UR7-0.6cm</b>	11.46	2.94	-1.79	1.83	-2.37
<b>UR7-0.8cm</b>	16.98	4.86	-3.20	3.34	-4.16
<b>UR7-1.0cm</b>	22.13	6.90	-4.68	4.95	-6.02
<b>UR7-1.2cm</b>	27.09	8.56	-6.34	6.54	-7.65
<b>UR7-1.4cm</b>	31.63	10.24	-8.17	8.21	-9.43
<b>UR7-1.6cm</b>	35.32	11.36	-9.71	9.53	-10.56
<b>UR7-1.8cm</b>	38.40	11.88	-10.94	10.41	-11.27
<b>UR7-2.0cm</b>	41.08	12.69	-11.78	11.24	-12.11

Table A.8. Pressures in the UR8 test.

<b>Experiment No</b>	<b>Pressure at the Foundation (kPa)</b>	<b>Pressure at the 1<sup>st</sup> Strain Gage (kPa)</b>	<b>Pressure at the 2<sup>nd</sup> Strain Gage (kPa)</b>	<b>Pressure at the 3<sup>rd</sup> Strain Gage (kPa)</b>	<b>Pressure at the 4<sup>th</sup> Strain Gage (kPa)</b>
<b>UR8-0.2cm</b>	8.26	0.53	-0.60	0.44	-0.04
<b>UR8-0.4cm</b>	14.43	1.42	-1.49	1.02	-0.17
<b>UR8-0.6cm</b>	19.88	2.39	-2.35	1.55	-0.41
<b>UR8-0.8cm</b>	25.08	3.37	-3.25	2.01	-0.79
<b>UR8-1.0cm</b>	29.62	4.11	-3.94	2.49	-1.11
<b>UR8-1.2cm</b>	33.45	4.66	-4.44	2.85	-1.26
<b>UR8-1.4cm</b>	36.36	4.94	-4.84	3.13	-1.33
<b>UR8-1.6cm</b>	37.98	5.03	-4.73	3.23	-1.79
<b>UR8-1.8cm</b>	38.65	6.54	-4.82	3.59	-3.08
<b>UR8-2.0cm</b>	40.39	7.31	-4.87	3.75	-3.71

Table A.9. Pressures in the UR9 test.

<b>Experiment No</b>	<b>Pressure at the Foundation (kPa)</b>	<b>Pressure at the 1<sup>st</sup> Strain Gage (kPa)</b>	<b>Pressure at the 2<sup>nd</sup> Strain Gage (kPa)</b>	<b>Pressure at the 3<sup>rd</sup> Strain Gage (kPa)</b>	<b>Pressure at the 4<sup>th</sup> Strain Gage (kPa)</b>
<b>UR9-0.2cm</b>	10.05	0.69	-1.00	0.44	-0.33
<b>UR9-0.4cm</b>	16.90	1.49	-2.01	1.27	-0.75
<b>UR9-0.6cm</b>	23.49	2.28	-2.95	2.55	-1.20
<b>UR9-0.8cm</b>	29.38	2.86	-3.62	3.75	-1.54
<b>UR9-1.0cm</b>	34.92	3.29	-4.14	4.79	-1.87
<b>UR9-1.2cm</b>	39.86	3.50	-4.42	5.61	-2.09
<b>UR9-1.4cm</b>	43.39	3.72	-4.64	6.20	-2.39
<b>UR9-1.6cm</b>	46.25	3.90	-4.73	7.03	-2.60
<b>UR9-1.8cm</b>	47.95	4.03	-4.62	7.16	-2.82
<b>UR9-2.0cm</b>	48.91	4.52	-4.80	7.44	-3.47